Annual Letter Report

Growth, Nitrogen Vacancy Reduction and Solid Solution Formation in Cubic GaN Thin Films and the Subsequent Fabrication of Superlattice Structures Using AlN and InN

Supported under Grant #N00014-86-K-0686 P5
Innovative Science and Technology Office
of the Strategic Defense Initiative
Office of the Chief of Naval Research
Report for the period January 1, 1991–December 31, 1991

Robert F. Davis, Zlatko Sitar, Michael J. Paisley, Joe J. Sumakeris,
Laura Smith, K. Shaun Ailey-Trent, and Dong W. Kum
Materials Science and Engineering Department
North Carolina State University
Campus Box 7907
Raleigh, NC 27695-7907

December, 1991

REPORT DOCUMENTATION PAGE

Form Approved
OMB No 0704 0188

1. AGENCY USE ONLY (Leave blank)	2. REPORT DATE	3. REPORT TYPE AND DATES COVERED
	December, 1991	Annual Letter 1/1/91–12/31/91

4. TITLE AND SUBTITLE Growth, Nitrogen Vacancy Reduction and Solid Solution Formation in Cubic GaN Thin Films and the Subsequent Fabrication of Superlattice Structures Using AlN and InN

5. FUNDING NUMBERS
R&T:s400001srq05
S.O.:1114SS

6. AUTHOR(S)
Robert F. Davis

7. PERFORMING ORGANIZATION NAME(S) AND ADDRESS(ES)
North Carolina State University
Hillsborough Street
Raleigh,NC 27695

8. PERFORMING ORGANIZATION REPORT NUMBER
N00014-86-K-0686 P5

9. SPONSORING/MONITORING AGENCY NAME(S) AND ADDRESS(ES)
Sponsoring: ONR, 800 N. Quincy, Arlington, VA 22217
Monitoring: Office of Naval Research Resider, N66005
The Ohio State University Research Center
1314 Kinnear Road
Columbus, OH 43212-1194

10. SPONSORING/MONITORING AGENCY REPORT NUMBER

11. SUPPLEMENTARY NOTES

12a. DISTRIBUTION/AVAILABILITY STATEMENT
Approved for Public Release; Distribution Unlimited

12b. DISTRIBUTION CODE

13. ABSTRACT (Maximum 200 words)

An atomic layer epitaxy deposition system configured for the growth of thin films of the III-V nitrides of Al, Ga and In has been designed, constructed and commissioned. The system allows the introduction of up to 16 gases without mixing. Self-terminating growth of crystalline GaN films has been achieved on single crystal wafers of (0001) α(6H)-SiC. Results of analyses via Auger spectroscopy, electron microscopy and electron diffraction are described. Deposition of AlN and GaN via gas-source MBE was also continued during this period. The principal emphasis concerned the initial stages of growth of both compounds on the substrates of (00001) α(6H)-SiC and (0001) sapphire, as determined using X-ray photoelectron spectroscopy. An initial layer of silicon nitride formed on the surface of SiC prior to the deposition of either nitride. The deposition of GaN on sapphire followed the Stranski-Krastanov mode of nucleation and growth, while on SiC, characteristics of three-dimensional growth were evident. By contrast, AlN grew initially in a layer-by-layer mode. Deposition of GaN on vicinal (100) β-SiC during UV irradiation resulted in the formation of a new 4H polytype of this material. Deposition of BN via gas-source MBE on Cu(110) resulted in nanocrystalline cBN; films grown on (111) Cu resulted in h-BN (graphitic phase). Similar studies using Si(100) substrates also resulted in the occurrence of cBN. The occurrence of the cubic polytype was enhanced while that of h-BN was discouraged with the use of the UV light at 400–500°C.

14. SUBJECT TERMS	15. NUMBER OF PAGES
gallium nitride, aluminum nitride, boron nitride, atomic layer epitaxy, layered structures, transmission electron microscopy, photoluminescence, gas-source MBE, laser ablation, borazine	76
	16. PRICE CODE

17. SECURITY CLASSIFICATION OF REPORT	18. SECURITY CLASSIFICATION OF THIS PAGE	19. SECURITY CLASSIFICATION OF ABSTRACT	20. LIMITATION OF ABSTRACT
UNCLAS	UNCLAS	UNCLAS	SAR

Table of Contents

I. INTRODUCTION

Continued development and commercialization of optoelectronic devices, including light-emitting diodes and semiconductor lasers produced from III-V gallium arsenide-based materials, has also generated interest in the much wider bandgap semiconductor mononitride materials containing boron, aluminum, gallium, and indium. The majority of the studies have been conducted on pure gallium nitride thin films having the wurtzite structure, and this emphasis continues to the present day. Recent research has resulted in the fabrication of p-n junctions in both wurtzite gallium nitride and cubic boron nitride, the deposition of cubic gallium nitride, as well as the fabrication of multilayer heterostructures and the formation of thin film solid solutions. Chemical vapor deposition (CVD) has usually been the technique of choice for thin film fabrication. However, more recently these materials have also been deposited by plasma-assisted CVD, reactive ionized-cluster beam deposition and reactive and ionized molecular beam epitaxy.

The program objectives in this reporting period have been (1) the continued development and employment of atomic layer epitaxy as a low temperature deposition method for GaN (2) the determination of the chemistry and morphology inherent in the nucleation and growth of GaN and AlN on the substrates of α(6H)-SiC (0001) and sapphire (Al_2O_3) (0001) via gas-source molecular beam epitaxy (GSMBE) and (3) the deposition of films of GaN and BN using GSMBE and microwave plasma chemical vapor deposition. The procedures, results, discussions of these results and conclusions of these studies are given in the following sections. Note that each major section is self-contained with its own figures, tables and references.

II. ATOMIC LAYER EPITAXY OF GALLIUM NITRIDE

A. Introduction

At the present time, MBE and MOCVD are the two contenders for the growth of the most sophisticated semiconducting structures. Both can produce extremely thin layers and a wide range of compound semiconductors and heterostructures. However, in both techniques all the reactant species arrive simultaneously to the substrate. As such, the growth of the subsequent monolayer of the material may be initiated before the growth of the previous one is completed. As a result, the growth process occurs on several levels of monolayers. This occurs in practically all materials deposition systems and is easily observed via RHEED oscillations. One observes the damping of the oscillation amplitude with the film thickness. As a result, the RHEED oscillations usually disappear after 10-20 monolayers of growth.

The ultimate technique, with the best control over the composition and the surface morphology, may be the deposition of a single layer of the atoms of one of the components at a time. The single most successful method for achieving this is by Atomic Layer Epitaxy

(ALE), a technique patented by Suntola and Atson in 1977 [1]. They used this method for the deposition of the polycrystalline ZnSe on glass substrates because of their concern regarding thickness uniformity over large areas.

Initially it was thought that ALE was applicable only for II-VI compounds. However, it has been shown that it also works also for other compounds and elements. A comprehensive review of the ALE research on II-VI compounds has been published by Goodman and Pessa [2]. Considerable attention has been lately devoted to the ALE of GaAs, and several research groups have demonstrated the feasibility of the technique for Ga-based III-V compounds [3,4].

Atomic Layer Epitaxy can be achieved with many existing deposition techniques, and is best thought of as a special mode of operation of the known techniques, rather than an entirely new deposition method. Since ALE consists of deposition cycles in which a single monolayer of individual species is deposited at a time, the final film thickness depends only on the number of cycles and the lattice parameter of the material. Thus ALE offers the ultimate control over the thickness and morphology of the layers, and has also the potential for the achievement of very good stoichiometry and the reduction of point defects. Since the reactants remain separated throughout the deposition, homogeneous nucleation of the desired phase within the gas stream is minimized.

B. Experimental Procedure

1. Description of the III-V Nitride ALE System

To accomplish ALE of the III-V nitrides, a vacuum system has been designed, fabricated and commissioned which allows ALE deposition within the framework of organometallic (OM) CVD parameters. The system is configured to process one-inch wafers. Ultimately, the apparatus may be adapted to handle samples up to two inches in diameter. The system consists of three chambers; a load lock, a cleaning chamber and a growth chamber. It is made of stainless steel parts with knife edge seals and is high vacuum capable. Process gasses are regulated by mass flow controllers and pumped by a rotary vane pump. The ultimate vacuum is achieved by diffusion pumps.

The load lock is a simple five way cross that can hold up to five samples. All samples are introduced to and removed from the system through this chamber; it can be evacuated to the millitorr level.

After passing through the load lock, the samples are cleaned in a subsequent chamber using a remote argon plasma with the downstream injection of hydrogen. The cleaning chamber is evacuated to high vacuum using a diffusion pump, while the process gases used for cleaning are handled by a rotary vane pump through an automatic throttle valve. To assure identical sample cleaning within a run, up to four samples can be cleaned at a time.

This chamber is capable of performing many variations on the plasma cleaning operation, since it has the capability of varying gas flow rates, substrate temperature, plasma intensity and process pressure.

After cleaning, the samples are transferred to the growth chamber. This chamber is also evacuated to high vacuum using a diffusion pump with an LN_2 trap, while the process gases are handled by a rotary vane pump. The volatile exhaust gases in the growth and cleaning chambers are diluted with nitrogen and cleaned in a water scrubber prior to the release into central exhaust system. The process pressure is monitored and controlled by a capacitance pressure gauge and an automatic throttle valve. Inside the growth chamber, the samples sit on a revolving, heated, disk-shaped holder made of SiC-coated graphite. The overall design allows sample heating to 1000°C. However, the intention is to process at substantially lower temperatures. Due to the large mass and the possible use of the high temperature capability, appropriate heat shielding and water cooling have been installed, as can be seen in the cross-sectional view of the system, shown in Figure 1.

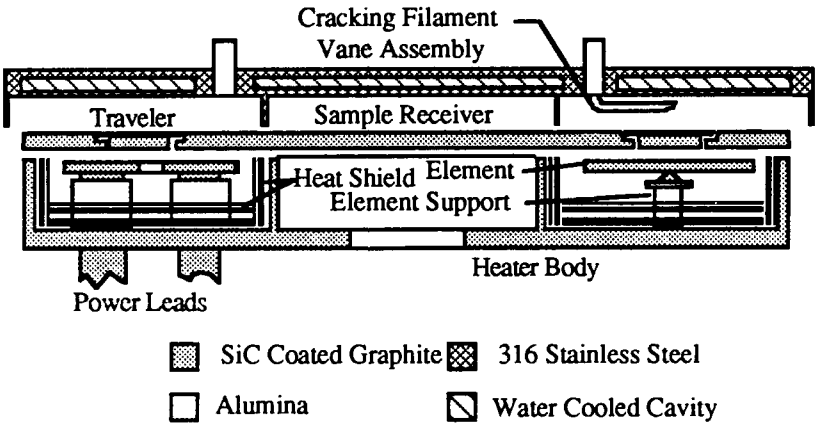

Figure 1. Cross-sectional view of the ALE growth chamber for the deposition of III-V nitrides.

A specially designed vane assembly allows the deposition in the ALE mode. The assembly is stationary above the rotating susceptor and consists of sixteen separate compartments for the introduction of up to eight different process gases without mixing. As wafers travel under each compartment, they experience a different atmosphere. However, the ALE process requires a purge cycle with an inert gas between each exposure of the wafers to the reactants. This prevents mixing of the reactant gases and allows time for the desorption of physisorbed molecules. After this cycle only the chemisorbed monolayer remains. If a purge is applied after every exposure to reactants, half of the zones (eight) remain for the deposition. That means four zones for each reactant when a binary compound is grown. This

arrangement allows the growth of four monolayers of each element (about 7-10 Å) of the binary compound per revolution of the susceptor. The anticipated growth rate in the ALE mode is about 1 μm per hour. Figure 2 shows a column V compartment containing a tungsten filament for creating active nitrogen containing species from the decomposition of ammonia. These species facilitate reaction with chemisorbed Ga atoms at low temperatures.

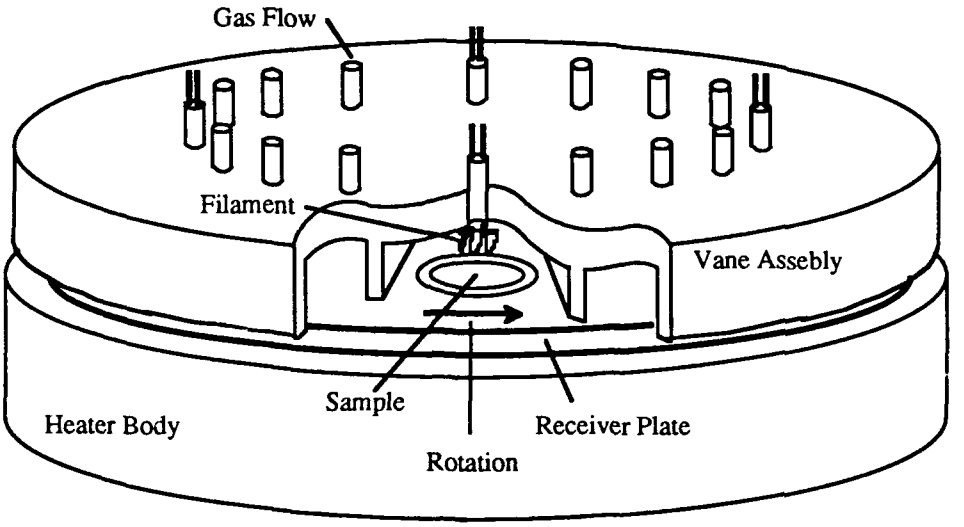

Figure 2. View into column V compartment. A tungsten filament is used to crack and activate ammonia and thus make it suitable for the reaction at a low temperature.

The gas introduction system is capable of handling organometallic and gaseous precursors. All gases used in the deposition are ultra high purity and further purified by chemical purifiers. Each OM module consists of a bubbler sitting in a constant temperature bath, a capacitance pressure transducer for measuring the pressure inside the bubbler, a manual metering valve for the pressure control, a mass flow-rate controller for the carrier gas, and several manual and pneumatic shut-off valves. This hardware allows precise dosing of the OM into the reaction chamber via the control of three key parameters: bubbler temperature, bubbler pressure and the carrier gas flow rate. Since the partial pressure of the OM in the bubbler depends on the temperature only, one can calculate the volume ratio between the OM source and the carrier gas supplied into reaction chamber simply as the ratio between the partial pressure of the OM at the bubbler temperature, $p_{OM(T)}$, and the partial pressure of the carrier gas ($p_T - p_{OM(T)}$).

$$X_{OM(T)} = \frac{p_{OM(T)}}{p_t - p_{OM(T)}}$$

The exact number of moles of OM reactant introduced into chamber is then calculated from the known flow rate of the carrier gas. The control of the introduction of the gaseous sources includes only a mass flow controller with a shut-off valve.

2. Growth Theory

Several different inorganic and organic precursors have been considered for the ALE of GaN. Organometallics were chosen over chlorides for the source of Ga because of high purity, ease of transport from the source to the chamber, and excellent control over dosing. Triethylgallium was chosen over trimethylgallium for two reasons: (1) lower decomposition temperature and thus lower growth temperature, which would reduce the concentration of nitrogen vacancies, and (2) cleaner surface reaction (the decomposition of trimethyl species often results in the decomposition of the higher deposition methyl radical resulting in residual C atoms which become incorporated in the growing film). Ammonia was chosen over hydrazine and nitrogen fluoride mainly because of safety considerations and cleanliness. Ammonia is available in research grade purity. Moreover, chemical ammonia purifiers, which effectively remove remaining water, oxygen and carbohydrides, are also available.

The reaction energy budget these precursors offer theoretically favors the self-limiting ALE deposition of III-V nitrides on (0001) surfaces of wurtzite or (111) surfaces of zincblende substrates. The growth direction is crucial, because the number of bonds a particular species makes on the surface varies greatly with the growth direction. A constituent of a tetrahedrally bonded compound can make one surface bond in the $(000\bar{1})$ direction, two surface bonds in (1011) direction and three surface bonds in (0001) direction.

An estimate of whether a reaction is favored or not, can be made by comparing the bond energies of the reactants and products. The bond energies between Group III metals and nitrogen, calculated using different methods, are summarized in Table I. For example, suppose, the (0001) surface is terminated with $Ga(C_2H_5)_2$ which makes one bond with the underlaying nitrogen. The subsequent exposure of these adsorbed species to ammonia causes a surface reaction to occur, if making three bonds with Ga is energetically favorable for the ammonia molecule. The process will end with a hydrogen terminated surface which does not react further with ammonia. The bond energy between Ga and the ethyl radical is 57 kcal/mol, and the average bond energy between nitrogen and hydrogen is about 90 kcal/mol.

Table I. Bond energies between III metals and nitrogen obtained by different methods.

B - N	Al - N	Ga - N	In - N	Remarks
115	125	108	105	Pauling's formula [6]
94	90	65	54	Geometrical mean with correction [6]
83-193	52-122	55-85	47-67	Immediate neighbors
72-91	64-80	55-69	49-61	Periodic behavior
66	67(81)	50(56)	49	Heat of vaporization [7]
87	94	69	58	Heat of formation [8]
85±5	**75±5**	**65±5**	**55±5**	Suggested values

Thus, the total enthalpy to break the necessary bonds within the precursors is (3×57) + (2×90) = 351 kcal/mol. On the other hand, the enthalpy of formation of each N-Ga bond releases 65 kcal/mol, and the reaction $C_2H_5 + H \rightarrow C_2H_6$ produces about 100 kcal/mol. Thus, the total enthalpy of reaction is: 3×65 + 2×100 = 395 kcal/mol. Since the energy of reaction is larger than the decomposition energy, the overall reaction to form a H-terminated N-Ga bilayer is favorable.

A similar calculation can be done for the next Ga layer. The Ga cycle starts with a hydrogen terminated nitrogen surface. Arriving TEG chemically adsorbs onto the surface by breaking one H-N bond (90 kcal/mol) and one Ga-ethyl bond (57 kcal/mol) and making one Ga-N bond (65 kcal/mol) and one C-H bond (100 kcal/mol) producing C_2H_6. The energy balance is 147:165 and the reaction is favorable for the deposition of a Ga layer.

The same calculation is valid also for AlN and BN. The only III metal with a marginal outcome is In, as can be seen from the data in Table I. However, such calculations offer only a rough estimate, since (1) data on bond energies are often inaccurate and (2) the enthalpy of transformation from the gas to solid state has been neglected. Energy requirements on a surface which acts as a catalyst may be even lower.

Figure 3 details the ALE process for gallium nitride from triethylgallium and ammonia as it occurs in our system. A clean, oxide-free 6H- SiC surface (A) is exposed to TEG which undergoes chemisorption involving rupture of some of the Ga-C_2H_5 bonds (B) until a continuous layer of adsorbed species is formed (C). Subsequently, the samples are exposed to an ammonia flux flowing across a hot filament (D). The ammonia attaches to the gallium precursor, replacing any previous termination until a complete layer of the NH_2 radical forms as shown in (E) At this point the sample may be again exposed to the TEG and the complete process repeated (F).

3. Growth and Analysis Procedures

In order to test and characterize the new equipment and the overall process, several deposition runs were made using different growth parameters. Table II gives the ranges over which the various parameters were varied. Throughout the test depositions four of the sixteen zones were used for TMG, four for ammonia and eight for the hydrogen purge gas.

Reflection High Energy Electron Diffraction (RHEED) was used to determine the crystallinity and structure of the grown films. Scanning Auger microscopy (JEOL JAMP-30) was performed to determine the presence of impurities and the nominal composition of the GaN layers. The surface morphology of the films was characterized using scanning electron microscopy (Hitachi S-530). Film thickness was measured by using a Rudolph automatic ellipsometer.

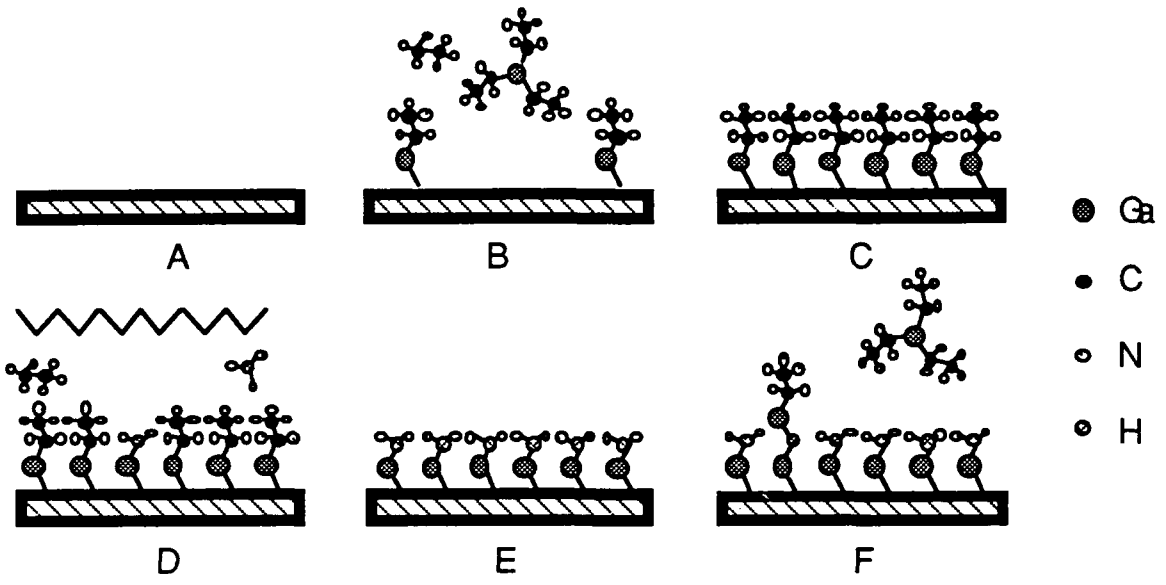

Figure 3. Schematic presentation of GaN ALE process using TEG and ammonia.

Table II. Growth parameters.

Growth temperature	350 - 650°C
Growth pressure	0.5 - 50 Torr
Ammonia flow rate	100 - 300 sccm
H_2 (purge) flow rate	200 - 300 sccm
H_2(OM carrier) flow rate	50 - 100 sccm
TEGa bubbler temperature	-10 - 20°C
TEGa bubbler pressure	400 - 800 Torr
Rotation speed	1 - 2 RPM

C. Experimental Results and Discussion

1. Surface Morphology

Initially, a few CVD runs were attempted, where all reactants were introduced into the same growth zone. The substrate temperature range was, 750-850°C. This did not result in the growth of GaN films. Only large (>10 μm) individual GaN crystals were observed on the surface. These were a possible result of homogeneous nucleation in the gas phase.

After a few unsuccessful experiments, the reactants were separated and distributed to the different growth zones. Substrates were rotated and sequentially exposed to different reactants. Films were grown at a constant chamber pressure of 50 Torr. The other parameters of growth temperature, flow rate, and substrate rotation speed (exposure time to each reactant gas) were changed.

Three dimensional growth was obtained at temperatures higher than 600°C, where individual crystallites were clearly seen. All of them had either a hexagonal or a triangular shape, both of which indicated a hexagonal structure. All of them were oriented in the same direction. The {0001} planes were perpendicular to the surface and the {1010} planes of the individual crystallites were parallel to each other. This indicated a good epitaxial relationship with the α(6H)-SiC substrate.

Films grown at temperatures lover than 400°C were continuous with no detectable surface morphology. Ga-rich films with Ga precipitates were obtained, when the same flow conditions were used as for the high temperature runs. When the supply of TEG was reduced by about three times, a clean GaN film without Ga precipitates was obtained. However, this reduced the growth rate form 2000 Å/hr to 600 Å/hr.

2. Chemical Analysis

Scanning Auger microscopy was performed on the samples to determine both the presence of impurities and the nominal composition of the GaN layers. No contaminants were observed within the resolution of the instrument (typically ≈0.1 at.%). Comparison of the Auger spectra of these films with those grown via MBE showed the ALE materials to be stoichiometric.

3. Electron Diffraction

Reflection high-energy electron diffraction (RHEED) was performed on the GaN films. All films showed a distinct diffraction pattern indicative of the wurtzite structure. The films grown at high temperatures showed spotty diffraction patterns, in agreement with the rough surface morphology observed via SEM. The films grown at low temperature showed streaked diffraction patterns indicative of a smooth surface, as well as Kikuchi lines indicative of good crystallinity.

The main aim of this research was to determine the experimental window in which GaN grows in a truly self-terminating process. Figure 4 shows the dependence of the amount of film grown per cycle with respect to the residence time per reaction zone. One can see that the growth per cycle initially increases quickly with exposure time but becomes more gradual after ≈10 sec. of exposure. Although these growth conditions could be utilized for layer-by-layer growth by correctly adjusting each exposure time, the process was not self-terminating at this temperature.

Subsequently, GaN films were grown at a sample temperature of 280°C. The crystallinity of these films has been confirmed by crystal x-ray diffraction. At an exposure time of 22 seconds, the growth rate corresponded to 2.62 Å per cycle, which corresponds to one monolayer of molecular coverage. When the growth was performed with an exposure time of

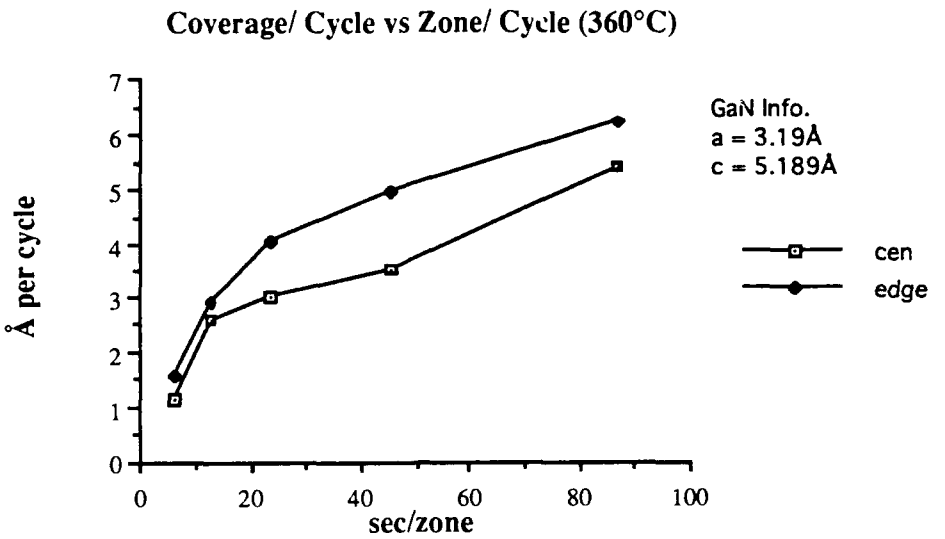

Figure 4. Dependence of the amount of film grown per cycle with respect to the residence time per reaction zone at a growth temperature of 360°C.

11 seconds the coverage per cycle falls to 1.2 Å per cycle. Recent mechanical difficulties with the system have prevented us from repeating the run for exposure times greater than 22 seconds, in order to determine if the coverage per cycle will remain unchanged at one monolayer per cycle.

D. Conclusions

The first results of the ALE growth of GaN are very encouraging. The system has performed well, and very low temperature growth of GaN has been achieved. The films were chemically stoichiometric crystalline and with a very smooth surface.

E. Future Research

Efforts to achieve a truly self-terminating layer-by-layer growth of both GaN and AlN and their solid solutions and heterostructures will be continued. Films of sufficient thickness (0.5 μm) will be grown in order to conduct electrical and luminescent measurements.

F. References

1. T. Suntola and J. Atson, U.S. Patent 4 058 430, Nov. 15 (1977).
2. C.H.L. Goodman and M.V. Pessa, J. Appl. Phys. **60**, R65 (1986).
3. S.M. Bedair, M. Tischler, T. Katsuyama, N.A. El-Masry, Appl. Phys. Lett. **47**, 51 (1985).
4. J. Nishizawa, H. Abe and T. Kurabayashi, J. Electrochem. Soc. **132**, 1197 (1985).
5. R. C. Weast ed., *Handbook of Chemistry and Physics*, 69thEdition 1988-1989, CRC Press, Inc., Boca Raton, Florida.
6. L. Pauling, *The Chemical Bond*, Cornell University Press, N.Y., 1967.
7. V. I. Vedeneev, *Bond Energies, Ionization Potentials and Electron Affinities*, St Martin's Press, N.Y., 1966.
8. T. L. Cottrel, *The Strengths of Chemical Bonds*, Butterworths Scientific Publications, London, UK, 1954.

III. INTERFACE CHEMISTRY AND SURFACE MORPHOLOGY IN THE INITIAL STAGES OF GROWTH OF GaN AND AlN ON α-SiC AND SAPPHIRE

A. Introduction

Successful commercialization of infrared and selected visible light-emitting optoelectronic devices simultaneously stimulated research in the wide-bandgap semiconductors for similar devices operational in the blue and ultra-violet regions of the spectrum. Much attention has been given to the III-V nitrides, particularly GaN and AlN, which possess direct bandgaps of 3.45 and 6.28 eV, respectively. Since they form a continuous range of solid solutions [1–3] and also superlattices [4, 5] they are suitable for bandgap engineering in the range of 3.45-6.28 eV.

Single crystal wafers of the nitrides are not available, thus they must be grown heteroepitaxially. Sapphire has been the most commonly used substrate, despite the huge lattice mismatch. The quality of heteroepitaxially grown films depends on two key issues: the lattice mismatch between the substrate and the film and the values of their respective surface energies. Both influence film growth in the very early stages and, as such have a significant influence on the overall quality of the heteroepitaxial films.

Three different growth regimes are clearly distinguished. The first one is layer-by-layer (or two dimensional) growth, in which the material is deposited in sequential monolayers of coverage. This type of growth is observed, when the substrate surface energy, σ_S, exceeds the sum of the surface energies of the overgrowth, σ_O, and the interfacial energy, σ_i (i.e. $\sigma_S \geq \sigma_O + \sigma_i$). In other words, the overgrowth "wets" the substrate. The second regime is Stranski-Krastanov growth in which the first few monolayers completely cover the surface of the substrate, while the subsequent layers form islands of deposited material. This type of growth satisfies the same equation as the layer-by-layer growth, but islanding occurs due to high strain energy which arises due to the lattice mismatch. The third regime is three dimensional growth, in which the material immediately forms islands on the surface. This type of growth occurs when $\sigma_S \leq \sigma_O + \sigma_i$. Figure 1 shows schematic representation of all three regimes.

Surface energies of the III-V nitrides have not been measured. A common theoretical method for covalently bonded materials involves the summation of the energies of the broken bonds per unit area of the surface [6]. However, surface bond energies also cannot be determined accurately. As such, one cannot determine from the theoretical modes of surface energy which substrate would be best suited for the heteroepitaxial growth of a certain material, e.g., GaN or AlN.

Experimental determination of the mode of nucleation and growth of a material on a selected substrate usually consists of several sequences of growth of 0.5 to 1 monolayer

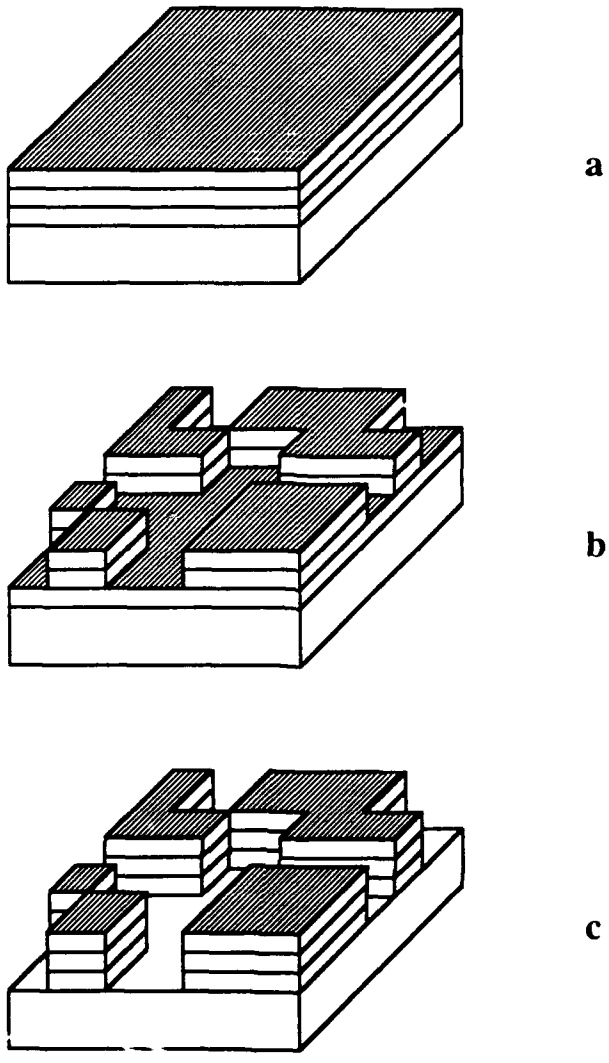

Figure 1. Schematic presentation of the three growth regimes: (a) Layer-by-Layer, (b) Stranski-Krastanov, (c) 3-Dimensional.

of material and analysis of the interface region either by Auger spectroscopy or XPS. The growth steps are repeated until a total of five to ten monolayers have been grown. Such an experiment is built on the fact, that electrons of a well defined energy travel in solids a certain distance without loosing their energy. This distance is called the escape depth. When they pass through a material, the flux of these electrons decreases exponentially. Since low energy electrons (a few 100 eV) have a very short escape depth (usually in the order of a few monolayers), they are a sensitive measuring tool for the characterization of very thin layers. If the substrate is excited with high energy electrons (as in Auger studies) or photons (XPS studies) which easily penetrate the grown film well beyond the escape region for characteristic electrons, one can consider the substrate as a source of an electron flux I_0. If a film is deposited in small steps, the electron flux of characteristic substrate lines decreases

with the film thickness. The dependence of the electron flux on film thickness can provide information regarding the initial growth morphology. A calculated plot of the decrease of the characteristic substrate XPS peak with film thickness for the three types of growth is shown in Figure 2 [7].

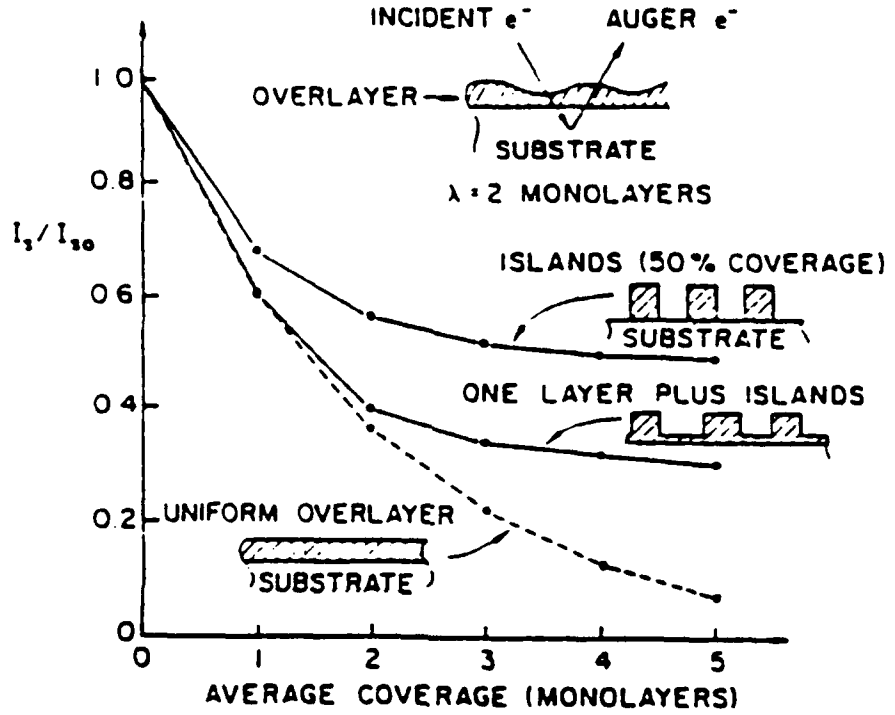

Figure 2. Extinction curves for characteristic substrate electrons as a function of coverage of an overlayer for different types of growth.

B. Experimental Procedures

1. Deposition System

The growth system was a commercial Perkin-Elmer 430 MBE system consisting of three major sections: a load lock (base pressure $\approx 5 \times 10^{-8}$ Torr), a transfer tube connecting the MBE and the analytical chambers (base pressure $\approx 1 \times 10^{-10}$ Torr) which was used to degas the substrates, and the growth chamber (base pressure $\approx 5 \times 10^{-11}$ Torr).

Knudsen effusion cells were used as gallium and aluminum sources. Films of GaN and AlN could not be produced within the experimental conditions of this study using molecular nitrogen. Therefore an ECR plasma source was designed, constructed and commissioned [8] in order to efficiently activate/dissociate molecules of this gas. This unique source has the advantage of fitting inside the 2.25 inch diameter tube of the source flange cryoshroud. Using this design, the source–to–substrate distance was minimized which increased the flux density at the substrate. A similar plasma source was not commercially available at the outset of this

effort. Some important parameters of the ECR source are given in the Table I. Ultra-high-purity nitrogen, further purified by a chemical purifier, was used as the source gas. The flow rate was regulated by a variable UHV compatible leak valve and was normally ≈5 sccm which resulted in a process chamber pressure of 1×10^{-4} Torr.

Table I. Some parameters of the NCSU-ECR nitrogen plasma source.

Overall source diameter	57 mm
Plasma diameter	23 mm
Microwave frequency	2.45GHz
Microwave power	0–100 W
Peak magnetic flux	1.05 kG
Nitrogen ion current density at 50 W	
• at the source	≈1 $mAcm^{-2}$
• at the substrate	150–200 μAcm^{-2}
Start pressure	1×10^{-4} Torr
Minimum operation pressure	1×10^{-5} Torr

2. Film Growth

Growth studies were conducted on (0001)-oriented α(6H)-SiC and the basal plane of epitaxial quality sapphire wafers, both of which have a hexagonal structure. All substrates were chemically cleaned to remove organic and metallic contaminants and mounted on a standard 3 inch molybdenum block with indium which provided both good adherence and thermal contact.

The substrates underwent an initial low temperature (≈70°C) outgasing in the load lock followed by slow heating in the transfer tube to a maximum of 700°C with a dwell time of 30 min at this temperature. After cooling, the samples were introduced into the growth chamber and examined by reflection high energy electron diffraction (RHEED) using a 10 kV beam. The resulting RHEED patterns on both the α-SiC and sapphire substrates showed Kikuchi lines, indicative of a good crystalline quality.

Prior to growth, the substrates were heated to the desired deposition temperature and subsequently exposed to a flux of plasma activated nitrogen species for about 5 min. Following the stabilization of temperatures and fluxes, a thin layer of GaN or AlN was grown. The growth conditions are summarized in Table II. After the growth was completed, the gallium or aluminum cell and the substrate were cooled, while the nitrogen source remained active until the substrate temperature was below 400°C. One set of experiments was conducted using photo enhancement, where a 500 W Hg lamp was used to irradiate the

samples during the growth. The XPS results of this study were compared with those described from the unirradiated sample.

Table II. Growth conditions.

Nitrogen pressure	$1x10^{-4}$ Torr
Microwave power	50 W
Gallium temperature	900°C
Aluminum temperature	1120°C
Substrate temperature	600°C
Thickness grown/deposition	0.2 - 0.5 nm
Number of deposition cycles	6 - 7
Total number of monolayers grown	5 - 12

3. XPS Analysis

XPS (X-ray photoelectron spectroscopy) was performed on the cleaned substrates prior to deposition and on the grown films after each deposition step. Samples were transferred from MBE growth chamber to the analytical chamber under UHV conditions. XPS spectra were obtained with a Riber Mg/Al X-ray source and a Riber MAC II cylindrical electron analyzer. Spectral data were acquired by an IBM PC-AT running software developed at NCSU.

For the study of the AlN growth, Mg Kα X-rays (1253.6 eV) were used to obtain spectra. For GaN growth, both the Mg and Al (1486.6 eV) anodes were used. The reason for alternating the X-ray sources for the examination of GaN was due to the fact that the Ga Auger electron emission occupies a large region of the spectrum between 0 and 1000 eV, and covers up certain XPS photoemission peaks of interest. The change of the X-ray energy shifts the Auger emission lines on an intensity vs. binding energy plot for the change in the energy of the X-ray photons, while the positions of the XPS photopeaks remains the same. The effect of changing the energy of X-rays is illustrated in Figure 3. Figure 3(a) is a wide-energy scan survey spectrum of GaN on sapphire obtained with the Mg X-ray anode, showing both substrate and film photopeaks and the Ga_{LMM} Auger emission cluster, which covers about a 250 eV wide band of the spectrum, from 150-400 eV. Figure 3(b) is a similar survey spectrum of GaN on SiC using the Al anode; this spectrum shows that the Ga Auger emission has been shifted by an amount equal to the energy difference between the two sources (233 eV). Owing to the positions of the Ga Auger emission, the Mg anode was used for examining the O_{1s} and N_{1s} photopeaks, while the Al anode was used for examining the C_{1s}, Si_{2s}, Al_{2p} and Ga_{3d} peaks.

For the study of GaN, the Si_{2s} photopeak at 153 eV was used, rather than the more commonly used Si_{2p} peak, again because of interference from Ga emission. The Ga_{3p} peak at

107 eV lies very close to Si_{2p} at 103 eV, and overwhelms the Si_{2p} emission, as the Ga signal increases with the thickness of GaN film. The Si_{2s} peak is also near another Ga photopeak (Ga_{3s} at 160 eV) but is located farther from the nearby Ga peak than the Si_{2p} peak is from its Ga neighbor. No switching of the anodes was necessary for the examination of AlN films. All photo-peaks of interest are well resolved on both substrates with the Mg anode, as can be seen in Figures 4 (a) & (b), which show a broad energy scan of AlN on SiC and sapphire, respectively.

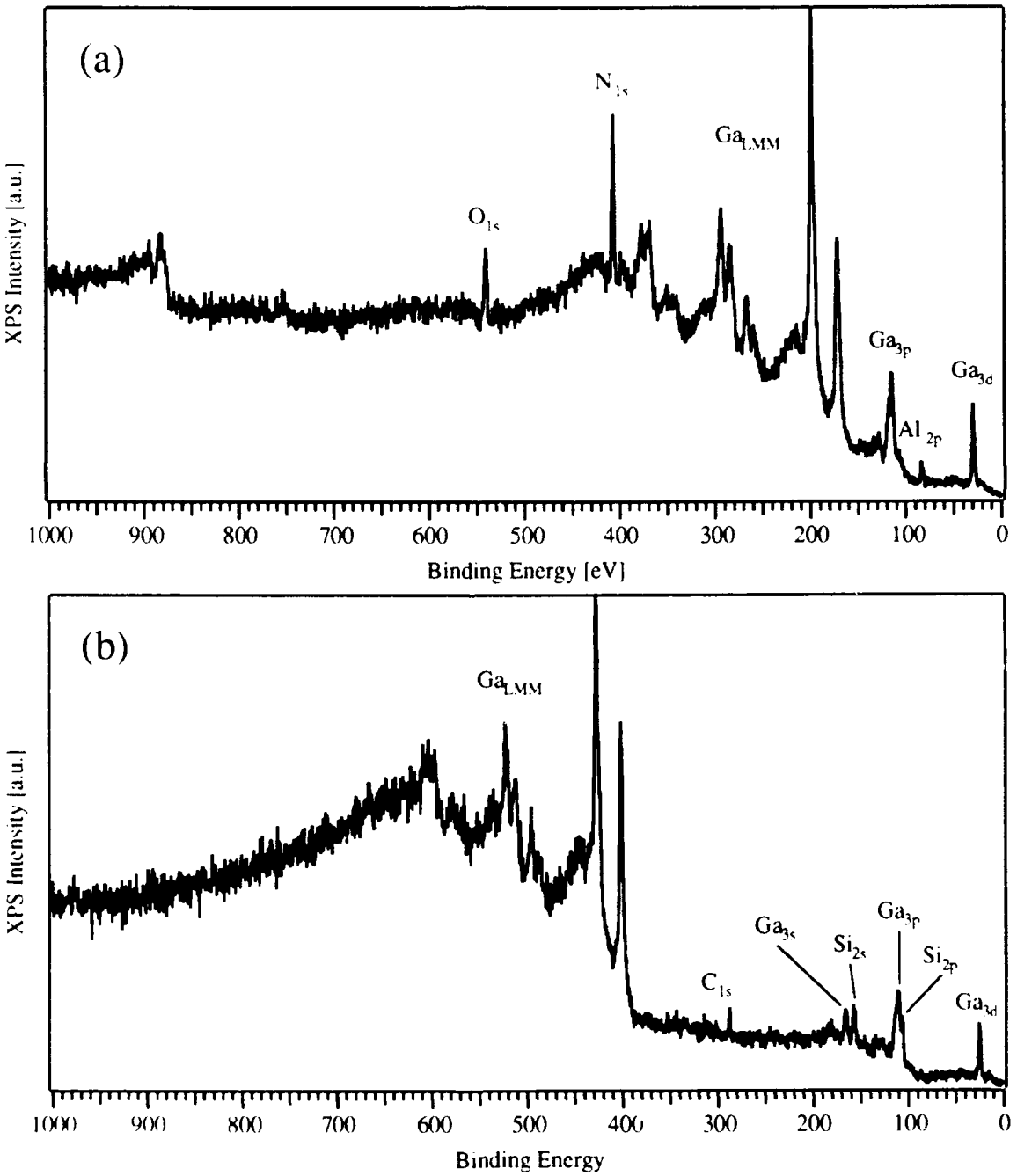

Figure 3. XPS survey spectra of GaN films: (a) Sapphire substrate, Mg X-ray source. (b) SiC substrate, Al X-ray source.

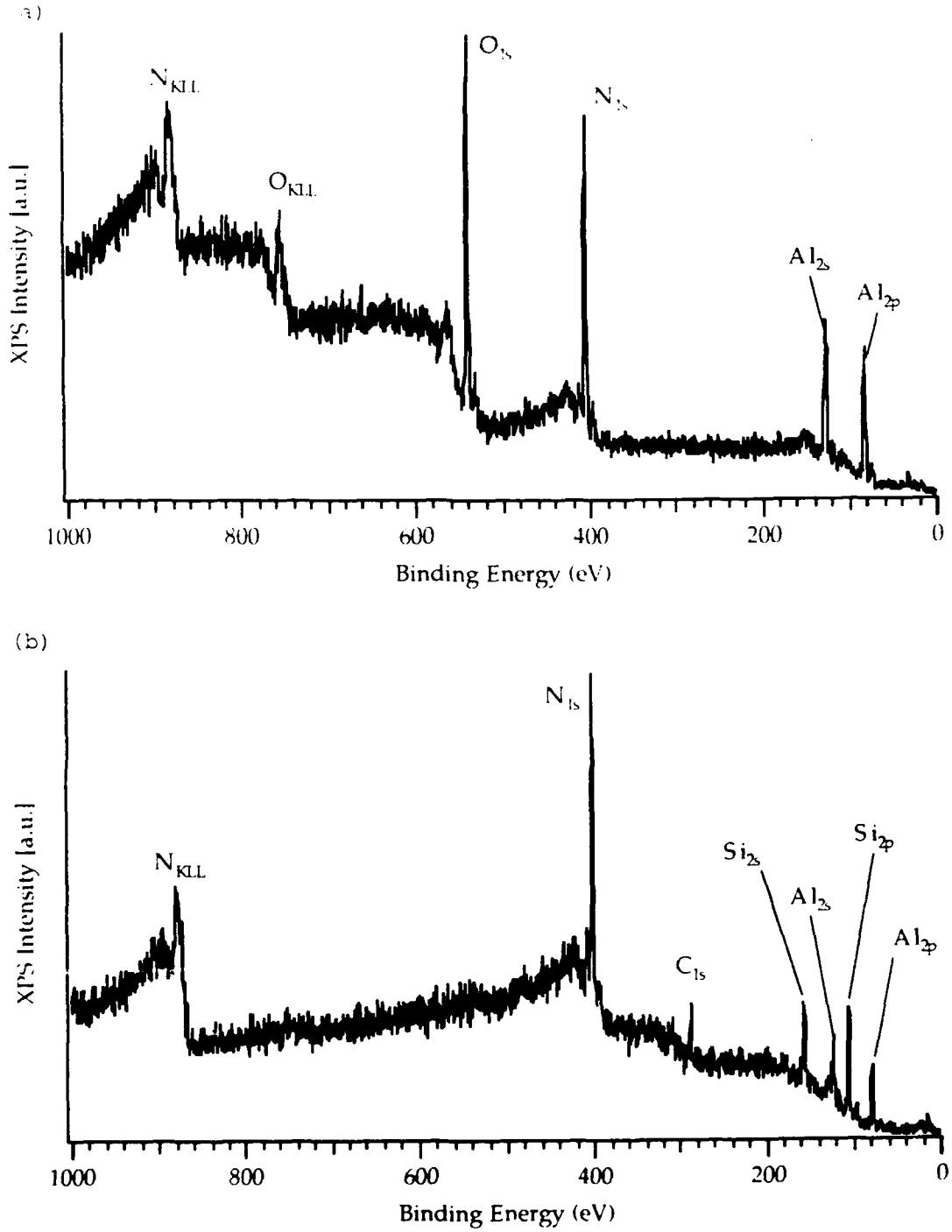

Figure 4. XPS survey spectra of AlN films: (a) Sapphire substrate, (b) SiC substrate. Mg X-ray source was used in both cases.

Electron escape depths were obtained from the universal curve of mean free path of electrons vs. their energy.[7] The escape depth is relatively insensitive to the material traversed by the electrons. Since XPS photoelectrons of C_{1S}, Si_{2S} and O_{1S} have considerably different binding energies, the energies of the escaped electrons differ as well. Since the energy of an escaped electron equals the incident X-ray photon energy minus the electron

binding energy, electrons with higher binding energy acquire less kinetic energy when being excited with the same kind of X-rays. Switching anodes from Mg to Al has an effect on the kinetic energy as well. The escape energies of selected photoelectrons and their respective escape depths are summarized in Table III.

Table III. Photoelectron energies and their escape depths.

	O_{1s}	C_{1s}	Si_{2s}
Photon Energy [eV]	1254 (Mg)	1487 (Al)	1487 (Al)
Binding Energy [eV]	531	283	152
Kinetic Energy [eV]	723	1204	1335
Escape Depth [Å]	12±1	18±1	18±1

Si_{2s} and C_{1s} peak intensities were monitored during the growth on SiC substrates and O_{1s} peak was examined during the growth on sapphire. The areas of the substrate peaks obtained after each deposition were calculated, compared to the areas of the peaks from the virgin substrate, and finally plotted vs. thickness of deposited material. Results were compared with a theoretical curve for layer-by-layer growth.

The binding energy value of each of the XPS photopeaks was referenced to the peak position, which was expected to be the most invariant. This procedure minimizes the effects of the analyzer characteristics and specimen charging. For the films grown on SiC, the C_{1s} peak was set at the typical value for SiC of 283.0 eV[9-11]. The other peaks were referenced to that value. For the films grown on sapphire substrates, the N_{1s} values of 397.0 for GaN [11, 12] and 397.3 for AlN [11, 12] were used as reference positions. For the clean sapphire substrates, prior to deposition, the photopeaks were referenced to the average value for O_{1s} observed during the remainder of the deposition.

C. Results and Discussion

1. Growth Morphology: GaN

Figures 5 and 6 show plots of relative substrate peak intensities vs. film thickness obtained during the growth of GaN both without (Fig. 5) and with (Fig. 6) UV treatment during growth. Both figures also contain theoretical curves representing layer-by-layer growth calculated at two escape depths, 12 (C_{1s},Si_{2s}) and 18 (O_{1s}) Å. The two curves correspond to the growth on SiC and sapphire, respectively.

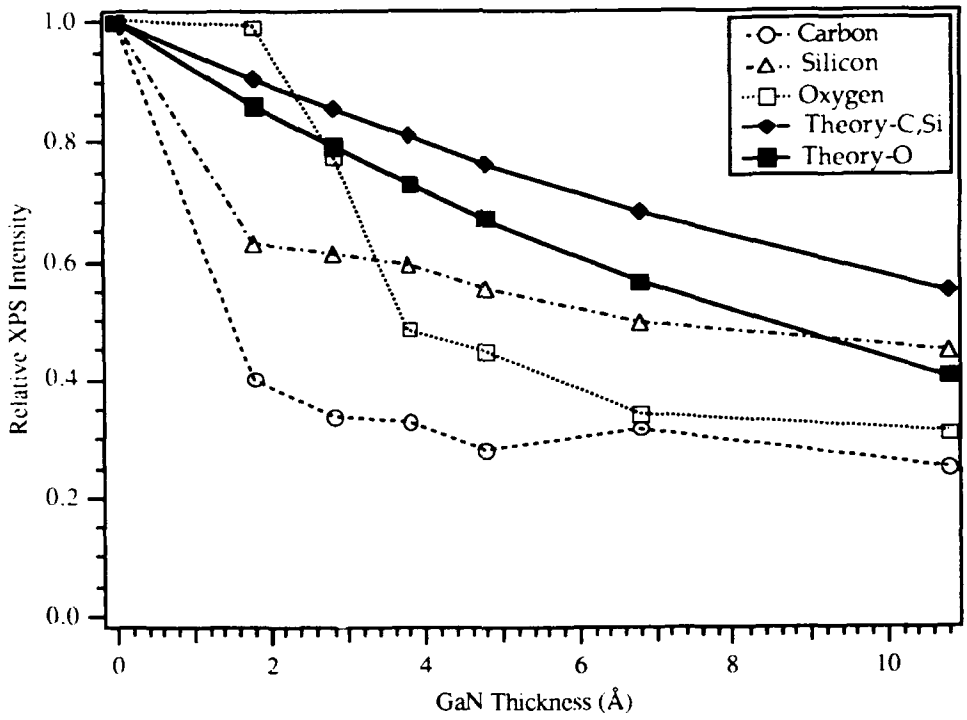

Figure 5. Change of XPS photoelectron intensity during growth of GaN on α(6H)-SiC and sapphire.

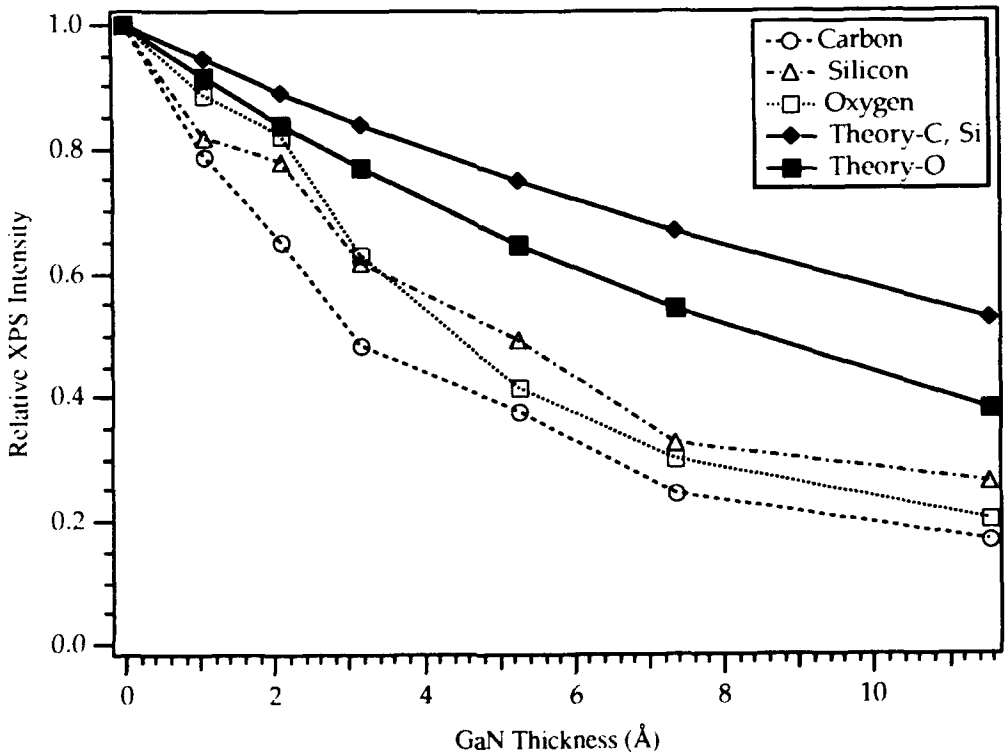

Figure 6. Change of XPS photoelectron intensity during UV-enhanced growth of GaN on α(6H)-SiC and sapphire.

The plots in Figure 5 show that the substrate peak intensity diminishes initially faster for the growth of GaN on SiC than on sapphire (compare O_{1s} to C_{1s} and Si_{2p} signals). This is most likely due both to a faster initial nucleation process on SiC, and to the formation of a thin silicon nitride layer at the interface (see below). This reasoning also agrees with the behavior of the O_{1s} signal. This signal decreases rapidly, once initial nucleation occurs, and with the same slope as the Si_{2p} and C_{1s} signals at the very beginning of the growth. Furthermore, an earlier study in the authors' laboratory of the growth rate of GaN on different substrates did not indicate a substantial difference between the growth rates on SiC and sapphire within experimental conditions. The growth rate was controlled by the Ga arrival rate rather than by any other factors.

Similar behavior for the change in the intensity of the Si_{2s} and C_{1s} photoemission was anticipated, since they originate from the same SiC substrate. However, this was not observed. As shown in Figure 2, the C_{1s} peak intensity shows a faster initial drop and also saturates at a lower value. This can also be explained by the formation of a thin layer of silicon nitride. Since the Si-face of the SiC substrates was used, a silicon nitride layer formed on the surface during exposure to the reactive N species prior to film deposition. This resulted in burying the carbon layer more deeply under the Si. The difference in the initial intensity drop approximately corresponds to the formation of one monolayer of silicon nitride.

All three curves assume a more gradual behavior after the initial rapid drop. The slopes of the C_{1s} and Si_{2s} signals in this region are considerably lower than the slope of the corresponding theoretical curve, which indicates an early saturation, while the slope of the O_{1s} signal exhibits a closer match to its theoretical curve. However, none of the experimental curves resembles the corresponding calculated curves for layer-by-layer growth.

The growth of GaN on sapphire appears to follow a Stranski-Krastanov mode while the growth on SiC shows some characteristics of three dimensional growth, although one would expect from the lattice mismatch a smoother growth on SiC than on sapphire. At present it is unclear whether or not this is due to the formation of a thin interfacial layer of silicon nitride.

Figure 6 shows the extinction curves of the substrate elements during UV-enhanced growth of GaN. In this case the substrate peak intensities show the same tendency to level off as they did in the first experiment, but slightly later in the growth process. In both cases however, the experimental curves drop more rapidly and subsequently show a tendency to level off before they reach zero, which is in contrast to the corresponding theoretical curves for layer-by-layer growth. As mentioned above, these curve shapes suggest island formation, either complete three-dimensional growth or Stranski-Krastanov growth. In the case of GaN growth without UV enhancement (Fig. 5), growth appears to be three-dimensional on SiC, and to follow a Stranski-Krastanov mode on sapphire with the formation of one monolayer.

In the case of UV-enhanced growth, the extinction curves for both SiC and sapphire are all similar, and indicate Stranski-Krastanov growth after the formation of 2 or 3 monolayers. Additionally, the results shown in Figure 10 reveal less evidence of silicon nitride formation than is indicated in Figure 5.

2. Growth Morphology: AlN

Figure 7 shows the change in XPS substrate peak intensities acquired during the growth of AlN. In this case, the experimental data resemble the corresponding theoretical curves more closely. This indicates that AlN grows layer-by-layer. This is in agreement with several reports which indicate that GaN films are affected beneficially when grown on an AlN buffer layer previously deposited on sapphire. Figure 8 shows the extinction curves obtained and calculated for UV-enhanced AlN growth. Here the experimental data indicate the development of island growth after 1 or 2 monolayers had formed. There is also more evidence of silicon nitride formation, as the C_{1s} signal drops off much more rapidly and saturates at a lower value than does the Si. As is the case with UV-enhanced growth of GaN (Fig. 6), the overall behavior of the two substrates appears to be similar.

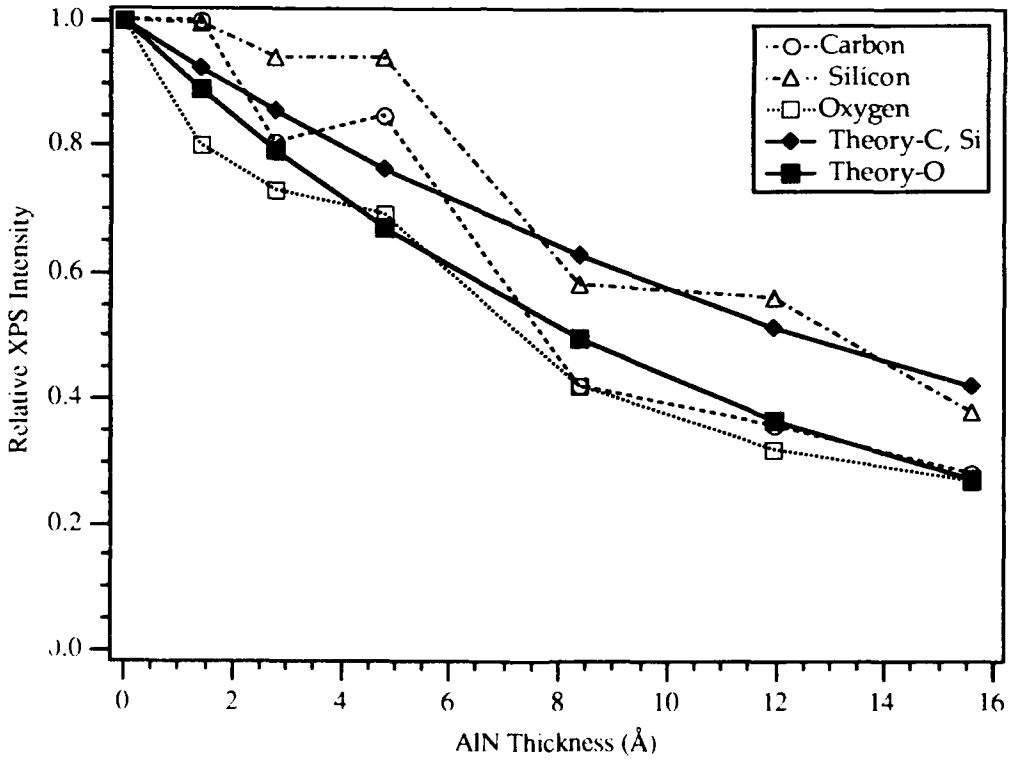

Figure 7. Change of XPS photoelectron intensity during growth of AlN on α(6H)-SiC and sapphire.

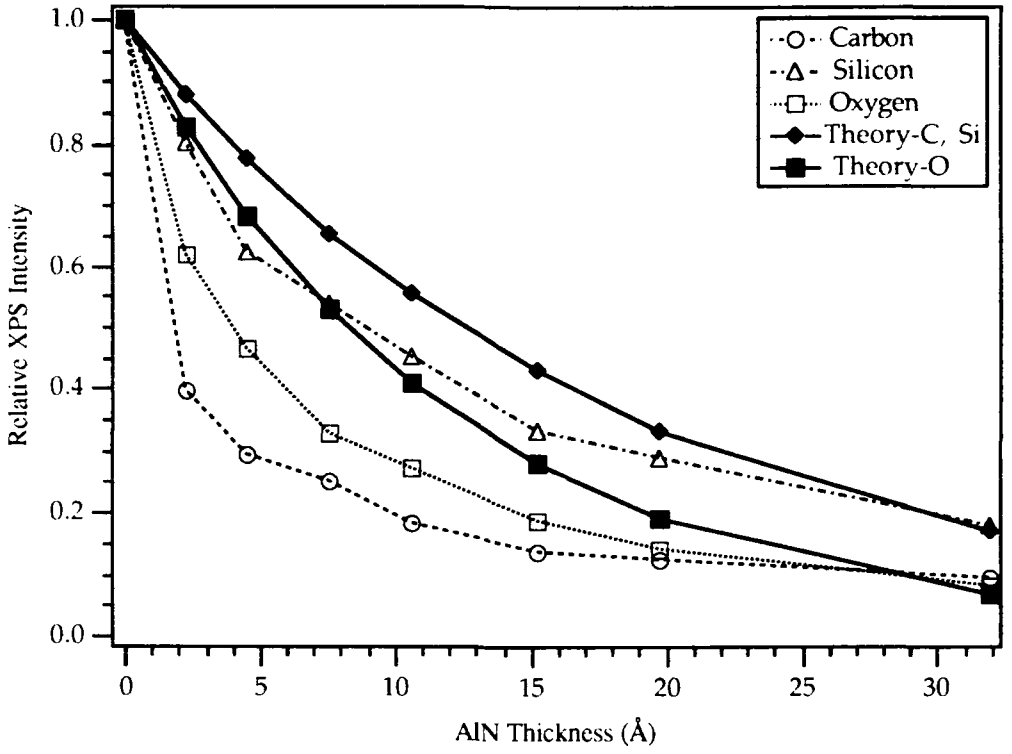

Figure 8. Change of XPS photoelectron intensity during UV-enhanced growth of AlN on α(6H)-SiC and sapphire.

3. Interface Chemistry: GaN

XPS was also used to characterize the chemical state of the substrates, interfaces and the growing films during the MBE deposition of GaN and AlN. Analysis of the cleaned substrates prior to deposition revealed the presence of very small amounts of carbon and oxygen surface contamination. The binding energy values obtained with reference to a particular peak for the growth series of GaN and AlN on sapphire and on α(6H)-SiC are listed in Tables IV, V, VI and VII.

In the case of non-UV-enhanced GaN growth (Table IV), the only XPS photopeak to show any significant binding energy shift is the Al_{2p} emission from the sapphire substrate. The slight shift (0.6 eV) may indicate that some Al-N bonding is taking place during GaN deposition, and the proportion of Al-N bonds increases with increasing coverage until the substrate is completely covered.

The Al_{2p} signal shows somewhat different behavior during the UV-enhanced growth (Table V). With the first deposition, the binding energy of the Al emission drops more than 1 eV and then gradually reaches a value similar to that in the first experiment. At the present time the reasons for this behavior are not well understood. The Ga_{3d} signal also shows a slight shift in the higher binding energy direction. The relatively low initial binding energy value for Ga is closer to the published values for elemental Ga than to GaN. This value

subsequently shifts to a higher value during deposition. It is possible that less of the Ga had reacted to form GaN in the early stages of the experiment, even though XPS peak-area calculations for Ga/N stoichiometry revealed a higher Ga/N ratio (of *total* Ga and N emission) from the first growth steps than from subsequent depositions.

Table IV. Binding energies of XPS photoelectrons measured during the GaN growth on sapphire and α(6H)-SiC.

Growth Step	0	1	2	3	4	5	6
On sapphire:							
Al_{2p}	74.0	73.8	73.6	73.4	73.7	73.4	73.4
O_{1s}	531.0*	531.3	531.1	531.0	531.2	531.0	530.9
Ga_{3d}	-	19.3	19.2	19.0	19.2	19.1	19.2
N_{1s}*	-	397.0	397.0	397.0	397.0	397.0	397.0
On α(6H)-SiC:							
Si_{2s}	152.1	152.2	152.2	152.2	152.2	152.2	152.2
C_{1s}*	283.0	283.0	283.0	283.0	283.0	283.0	283.0
Ga_{3d}	-	19.9	19.9	20.0	19.9	20.0	20.0
N_{1s}	-	397.7	397.6	397.7	397.5	397.6	397.7

* Values set as reference.

Table V. Binding energies of XPS photoelectrons measured during the UV-enhanced GaN growth on sapphire and α(6H)-SiC.

Growth Step	0	1	2	3	4	5	6
On sapphire:							
Al_{2p}	74.0	72.7	72.8	73.2	73..	73.2	73.6
O_{1s}	531.0*	530.8	531.0	531.1	531.0	531.0	531.0
Ga_{3d}	-	18.5	18.4	18.9	18.8	18.9	19.0
N_{1s}*	-	397.2	397.2	397.2	397.2	397.2	397.2
On α(6H)-SiC:							
Si_{2p}	100.9	101.0	101.0	101.1	101.1	101.0	101.1
C_{1s}	283.0	283.0	283.0	283.0	283.0	283.0	283.0
Ga_{3d}	-	20.1	20.1	20.1	20.1	19.9	19.8
N_{1s}	-	398.0	397.9	397.9	397.8	397.7	397.5

* Values set as references; NSP = no significant peak.

Table VI. Binding energies of XPS photoelectrons measured during the AlN growth on sapphire and α(6H)-SiC.

Growth Step	0	1	2	3	4	5	6
On sapphire:							
Al_{2p}	75.0	75.0	75.0	74.8	74.5	74.2	74.1
O_{1s}	532.0*	532.2	532.1	532.0	531.9	531.8	531.8
N_{1s}*	-	397.3	397.3	397.3	397.3	397.3	397.3
On α(6H)-SiC:							
Si_{2p}	100.9	101.0	101.0	101.1	101.1	101.0	101.1
C_{1s}	283.0	283.0	283.0	283.0	283.0	283.0	283.0
Al_{2p}	-	NSP	NSP	NSP	74.0	74.0	74.1
N_{1s}	-	397.6	397.6	397.5	397.3	397.3	397.4

* Values set as references, NSP = no significant peak.

Table VII. Binding energies of XPS photoelectrons measured during UV-enhanced AlN growth on sapphire and α(6H)-SiC.

Growth Step	0	1	2	3	4	5	6	7
On sapphire:								
Al_{2p}	74.9	74.9	74.6	74.6	74.4	74.3	74.1	74.0
O_{1s}	531.9*	532.2	532.0	531.9	531.8	532.0	531.7	531.7
N_{1s}*	-	397.3	397.3	397.3	397.3	397.3	397.3	397.3
On α(6H)-SiC:								
Si_{2p}	100.7	100.8	100.9	101.0	101.0	100.9	101.2	101.0
C_{1s}	283.0	283.0	283.0	283.0	283.0	283.0	283.0	283.0
Al_{2p}	-	73.4	73.8	73.8	73.8	73.8	73.8	74.0
N_{1s}	-	397.1	397.2	397.2	397.2	397.1	397.2	397.4

* Values set as references.

4. Interface Chemistry: AlN

The binding energy values of the Al_{2p} emission during AlN growth on sapphire (Tables VI and VII) show trends similar to those seen in GaN growth. In this respect there is no difference caused by the application of UV excitation during growth. Additionally, in the case of UV-enhanced growth of AlN on SiC the Al_{2p} signal behaves in a manner similar to that of Ga_{3d} during UV-enhanced growth. The slight shift of the Al_{2p} peak from a lower binding energy value to a higher one corresponding to AlN is an indication that Al-N bonding is not complete in the earliest stages of deposition.

The sequence of Si_{2p} peaks acquired between deposition steps during the growth of AlN on α(6H)-SiC is shown in Figure 9. The initial Si_{2p} signal from the bare substrate was a symmetrical peak characteristic of clean SiC. With the first AlN growth step, significant shouldering of the peak appeared on the high binding energy side, indicating the presence of a more highly oxidized state of the silicon. This shoulder persisted throughout the film deposition process and remained as the SiC component and the overall Si intensity diminished with film growth. Gaussian curve fitting analysis was applied to the most intense shouldered peak, obtained at the first growth step, to resolve the position of the high binding energy component. The results of curve fitting are shown in Figure 10.

By means of Gaussian curve fitting, the high binding energy shouldering was found to be primarily due to a single component shifted 1.4 eV from the main SiC peak. This component has been attributed to the formation of silicon nitride during the initial stages of AlN growth. This behavior shows that the Si-face of SiC initially undergoes nitridation.

The UV-enhanced growth of AlN on SiC exhibited very similar behavior. Shouldering of the Si_{2p} peak was again quite apparent, and curve fitting of the shouldered peaks revealed the same silicon nitride component shifted 1.4 eV from the SiC peak. The results of this curve fitting for UV-enhanced growth are shown in Figure 11.

A similar conclusion could not be made for the growth of GaN on SiC, although there is little reason to expect that in this case a completely different chemistry *initially occurred* at the interface. The sequence of Si_{2s} peaks acquired between deposition steps during growth of GaN on α(6H)-SiC is shown in Figure 12. However, the shouldering effect was not apparent, since Si spectra obtained during the growth of GaN show lower peak intensities and a poorer signal-to-noise ratio than the spectra obtained for AlN. The close proximity of the Ga_{3s} peak on the high energy side, as shown in Figure 3, could have obscured the evidence of the silicon nitride formation as well.

The film elements Ga, Al, and N exhibited no significant changes in chemistry, except for the slight shift of the Al_{2p} peak from AlN growth on sapphire as the Al_2O_3 gave way to AlN. Thus the XPS analysis indicates that no significant chemical reactions occurred between the growing films and the substrates other than the formation of small amounts of interfacial Si_3N_4 during the initial stages of growth on SiC.

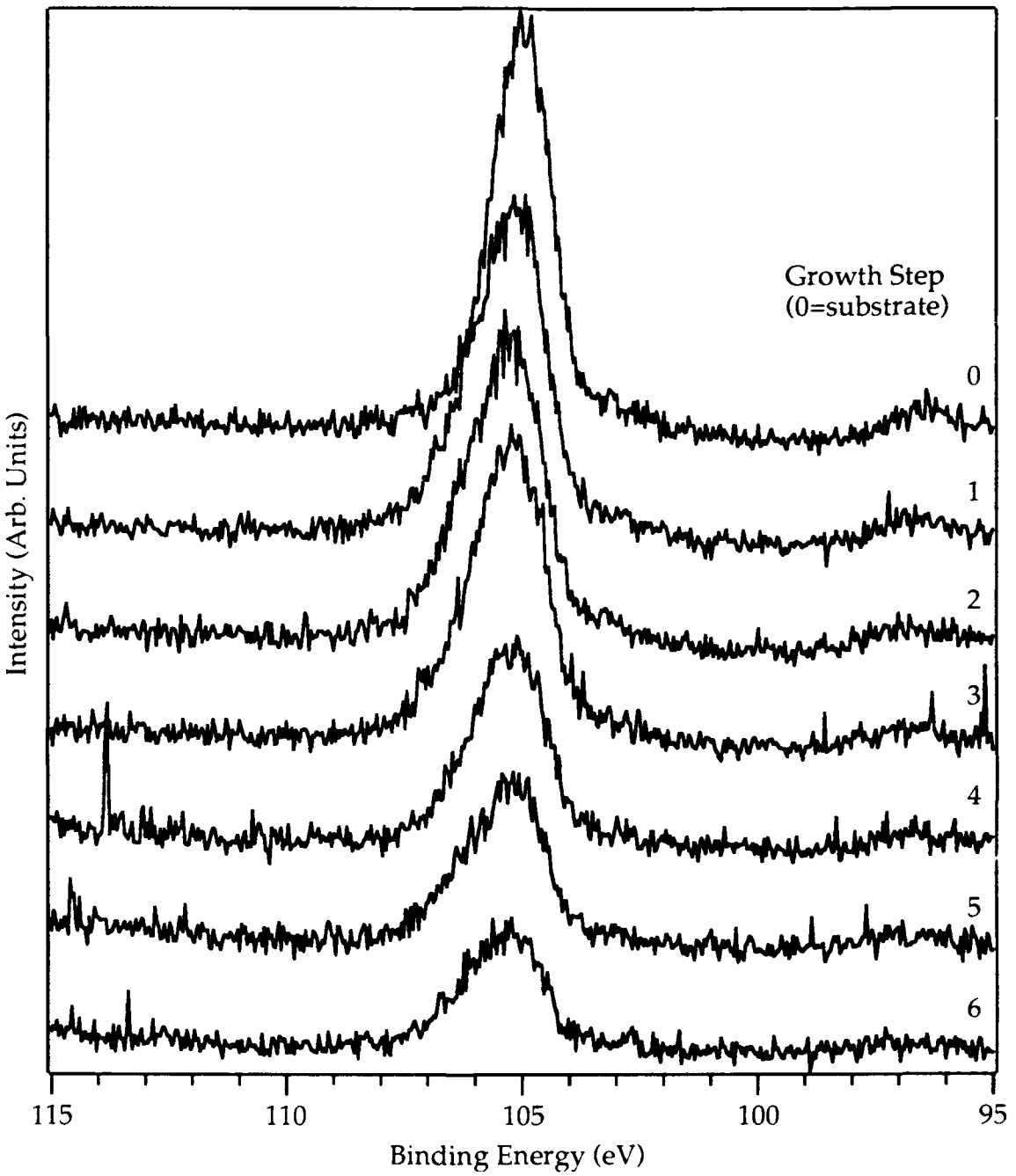

Figure 9. Si_{2p} photoemission as a function of AlN growth on SiC. Shoulder developed on the high binding energy side was due to the formation of Si_3N_4.

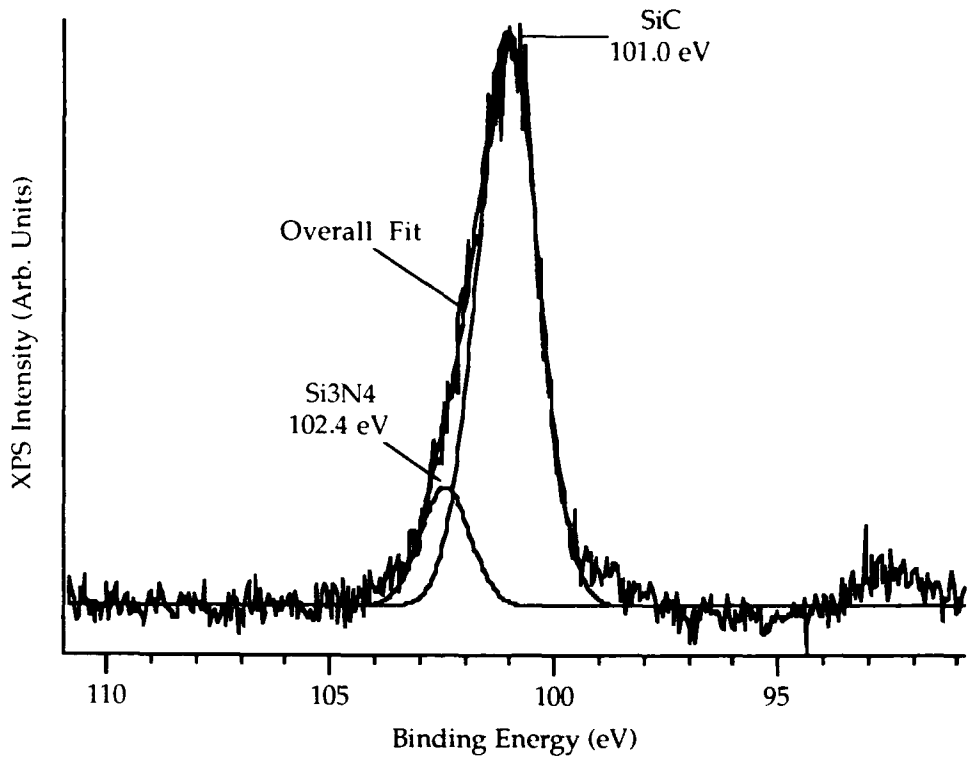

Figure 10. Gaussian curvefit of Si_{2p} photoemission from AlN deposited on α–SiC, showing component attributed to Si_3N_4 shifted 1.4 eV from SiC peak.

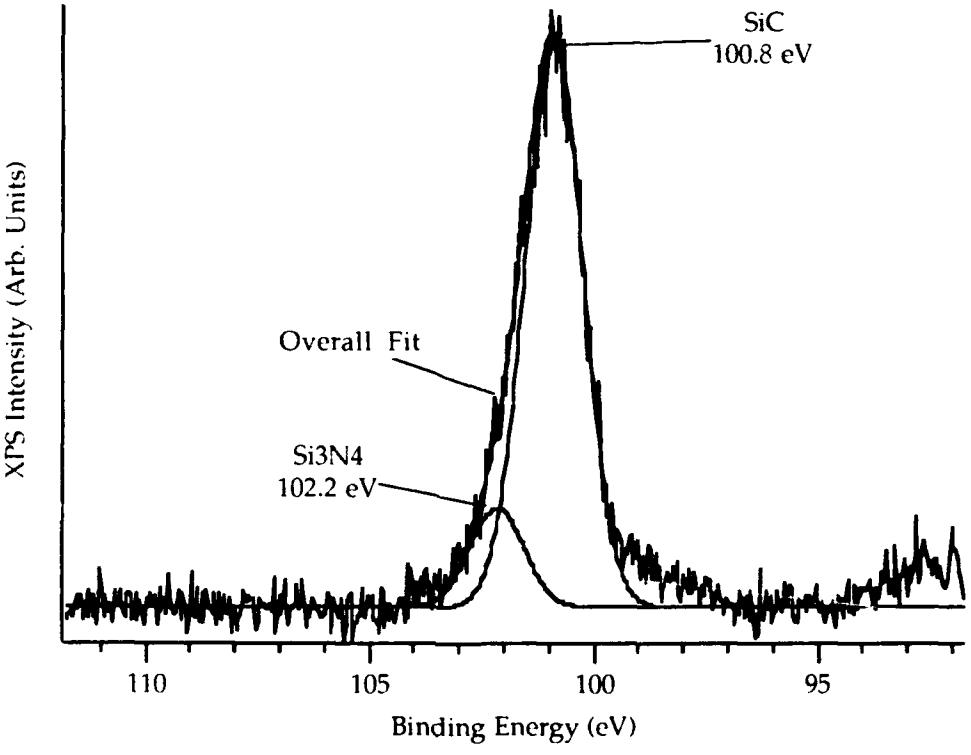

Figure 11. Gaussian curvefit of Si_{2p} photoemission from UV-enhanced deposition of AlN on α-SiC, showing Si_3N_4 component.

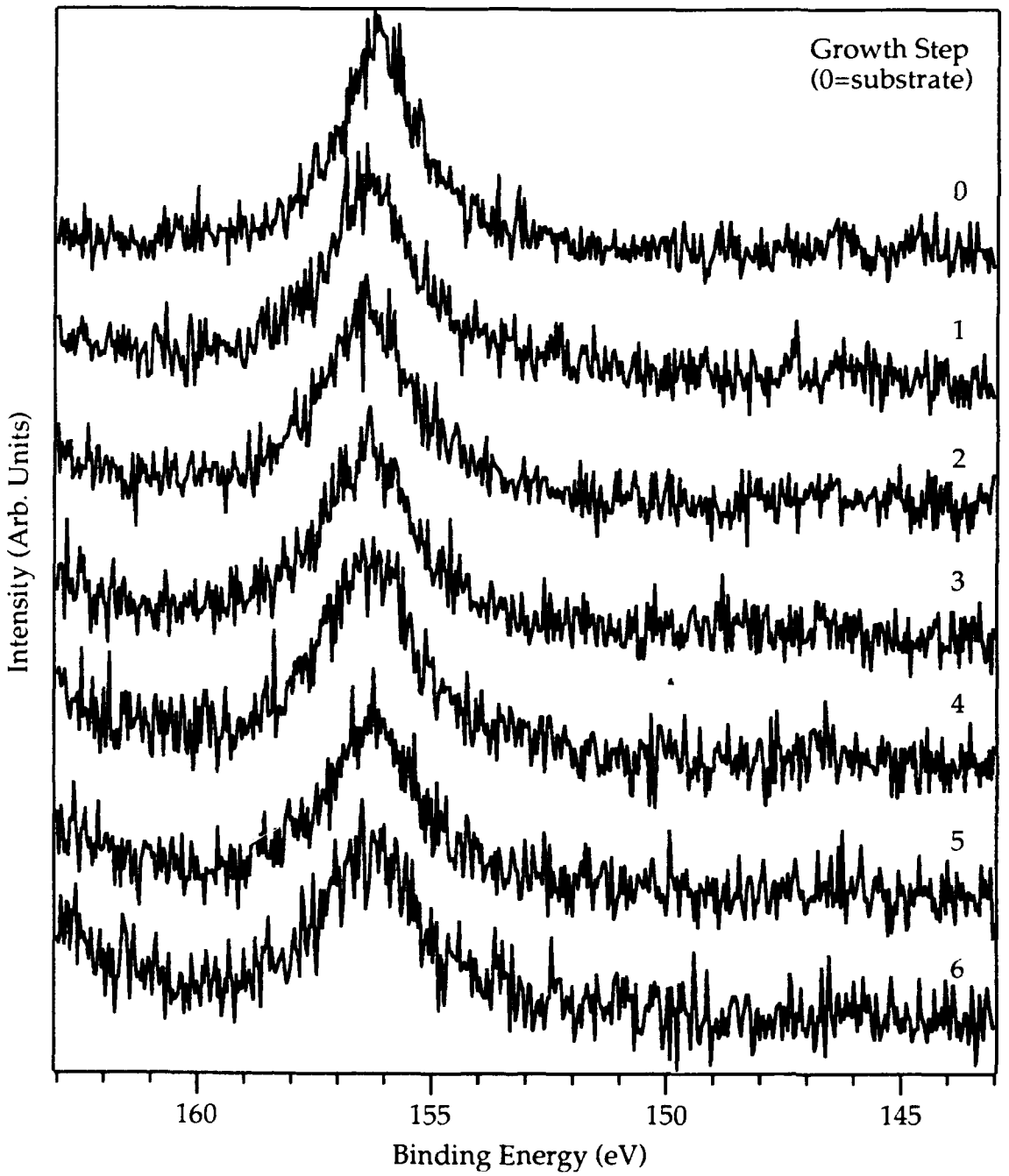

Figure 12. Si_{2s} photoemission as a function of GaN growth on SiC.

D. Conclusions

The initial stages of growth of AlN and GaN on SiC and sapphire substrates via plasma enhanced MBE and a photo-assisted MBE process were studied. Information regarding the morphology and interface chemistry was obtained. Evidence for silicon nitride formation was obtained from studies both of the Si oxidation states and the substrate peak intensity dependence on the film thickness. No significant chemical changes at the interface were observed when films were grown on sapphire.

A faster GaN nucleation was observed on SiC, while AlN apparently nucleated on both substrates equally well.

The growth of GaN on sapphire appeared to occur via the Stranski-Krastanov mode, while the growth on SiC showed some characteristics of three dimensional growth. At present, it is unclear whether or not this latter result is solely due to formation of thin interfacial layer of Si_3N_4.

The study of AlN showed that it grows layer-by-layer on both substrates. The application of UV radiation during the growth did not produce any significant changes.

E. Future Research Plans

The deposition of AlN and GaN and layered structures of these materials via GSMBE will be continued. Since the main goals are the improvement of the quality of materials, and growth of p-type GaN and AlN the short term research will be devoted to the production of smooth layers of both materials and their solid solutions. Mg will be used as the dopant for both compounds. A Hg UV light source will be to be used in the doping studies. Having achieved the quality and desired electrical properties, all efforts will be focused toward the growth of structures for simple optoelectronic devices.

F. References

1. M. R. H. Khan, Y. Koide, H. Itoh, N. Sawaki and I. Akasaki, Solid State. Comm. **60**, 509 (1986).
2. S. Yoshida, S. Misawa and S. Gonda, J. Appl. Phys. **53**, 5844 (1982).
3. Y. Koide, H. Itoh, M. R. H. Khan, K. Hiramatu, N. Sawaki and I Akasaki, J. Appl. Phys. **61**, 4540 (1987).
4. Z. Sitar, M. J. Paisley, B. Yan, J. Ruan, J. W. Choyke, and R. F. Davis, J. Vac. Sci. Technol. B **8**, 316 (1990).
5. Z. Sitar, M. J. Paisley, B. Yan, J. Ruan, J. W. Choyke, and R. F. Davis, Thin Solid Films, **200**, 311 (1991).
6 A.W. Adamson, *Physical Chemistry of Surfaces*, 5th ed. John Wiley and Sons, Inc., N.Y., 1990.
7. L.C. Feldman and J.W. Mayer, *Fundamentals of Surface and Thin Film Analysis*, North-Holland, N.Y.
8. Z. Sitar, M. J. Paisley, D. K. Smith, and R. F. Davis, Rev. Sci. Instr. **61**, 2407 (1990).
9. F. Bozso, L. Muehlhoff, M. Trenary, W.J. Choyke, and J.T. Yates, Jr., J. Vac. Sci. Technol. A **2**, 1271 (1984).
10. P.A. Taylor, M. Bozack, W.J. Choyke, and J.T. Yates, Jr., J. Appl. Phys. **65**, 1099 (1989).
11. NIST X-Ray Photoelectron Spectroscopy Database, version 1.0, NIST Standard Reference Database 20. National Institute of Standards and Technology, Gaithersburg, MD, 1989.
12. J. Hedman and N. Mårtensson, *Physica Scripta* **22**, 176 (1980).

IV. GAS-SOURCE MOLECULAR BEAM EPITAXY OF BORON NITRIDE AND GALLIUM NITRIDE

A. Introduction

1. Boron Nitride

Boron nitride has long been known for its desirable properties as a highly insulating as well as a chemically and thermally stable material. The cubic phase of boron nitride was first reported by Wentorf,[1] who produced it in a high pressure apparatus. This investigator also conducted the initial measurements regarding the semiconducting properties of this material. It has been used since then primarily for its high hardness in applications such as grinding and polishing. The cubic phase of BN is actually the zinc blende structure or, in space group notation, $F\bar{4}3m$ (Hermann-Mauguin) or T_d^2 (Schöenflies). Boron nitride is very similar to carbon in that both exist in hexagonal, wurtzitic, and cubic forms and many of the properties in each of the phases are strikingly similar. For example, both diamond and c-BN are metastable under the conditions currently used for growth of thin films. The primary difference is that hexagonal boron nitride is an insulator and hexagonal carbon is a conductor.

Interest in the cubic polymorph of BN as a semiconductor material has received much interest recently as a possible substrate for the deposition of diamond, due to the similar lattice parameters (Δa_0=1.34%) and its wider bandgap which is in the range of 5.8–6.5 eV.[2–4] Potential applications which would make use of the very wide bandgap of c-BN include optical devices for the vacuum UV (λ~200 nm) and high-power electronic devices. For a complete listing of materials-related properties of c-BN see *Landolt-Börnstein:Numerical Data and Functional Relationships in Science and Technology, Series III, Vols. 17 and 23*, or Ref. [5] (which also includes a side-by-side comparison of properties of c-BN with diamond).

Several approaches have been employed in the attempt to grow thin films of cubic boron nitride (c-BN). These include reactive diode[6] and rf sputtering,[7] ion implantation,[8, 9] plasma CVD,[10–12] microwave plasma CVD,[13, 14] and ion plating techniques.[15–18] These attempts were successful in producing polycrystalline films of c-BN, predominantly of a mixed nature with both cubic and other phases present and of extremely fine grain size. It appears that most researchers succeeded in the deposition of c-BN if the technique included the input of additional energy from energetic ions during the deposition process.

Research in the present program using microwave plasma CVD to deposit c-BN films and conducted in conjunction with ASTeX, Inc., has been described in the paper submitted to *Kobe Research and Development*. A preprint of this paper is included in this report as Appendix I. This study has attempted to use the energetic plasma conditions of a microwave ECR source to provide that important additional energy. The previous progress report of June, 1991, indicated that the resulting films were amorphous with cubic character. In

discussing future research plans in that report, mention was made of the use of a UV light source to provide additional energy to the growth processes. This process route has since begun to be investigated for the growth of c-BN. However, since photo-enhancement of growth processes is a relatively new field, this field will be briefly reviewed in the following section.

2. Gallium Nitride

Gallium nitride (GaN) is currently known to occur in two different tetrahedrally-coordinated crystal structures. The best characterized polymorph is wurtzitic GaN which, in space group notation, is $P6_3mc$ (Hermann-Mauguin) or C_{6v}^4 (Schöenflies) or B4 (Strukturbericht). It has the lattice parameters of a=0.3190 nm and c=0.5189 nm (Note that c/a=1.627 is near the ideal ratio of 1.633 for hexagonal unit cells.).[19] The more recently discovered cubic polymorph of GaN is actually the zinc blende structure or, in space group notation, $F\bar{4}3m$ (Hermann-Mauguin) or T_d^2 (Schöenflies) or B3 (Strukturbericht) with a lattice parameter of 0.451 nm.

The cubic polymorph has properties only slightly different from wurtzite, due to the fact that the bonding environments are similar. Indeed, the two structures differ only in the stacking of essentially identical tetrahedral units.[20] Thus, it is expected that the properties of c-GaN would be very similar to that of w-GaN. Since w-GaN is far better characterized, its properties will be used in the discussion of the material in general.

Wurtzitic GaN is a wide bandgap (3.45 eV at 300K, or 3.28 eV for c-GaN)[21] III-V compound semiconductor. The large direct bandgap and high electron drift velocity of GaN are important properties in the performance of short wavelength optical devices and high power microwave devices. Immediate applications that would be greatly enhanced by the availability of GaN and/or $Al_xGa_{1-x}N$ devices include threat warning systems (based on the ultraviolet {UV} emission from the exhaust plumes and supersonic bow shock of missiles) and radar systems (which require high power microwave generation). Important future applications for devices produced from these materials include blue and ultraviolet semiconductor lasers, blue light emitting diodes (LEDs) and high temperature electronic devices.

3. Photo-Enhanced Growth

Unfortunately, the study of photochemistry in the solid state has progressed slowly, especially in comparison to solutions and gases. Fleischauer points out in his review of solid state photochemistry[22] that this is due to the complexities of the analysis when compared to solutions and gases. Readers are referred to Fleischauer's review for information on photo-chemical processes, though it is strongly slanted toward examples in research on metal

complexes. In the sections that follow, only those processes which might have an impact on growth phenomena are covered.

Photo-enhanced growth techniques are generally applications of photochemistry to the growth processes, with the possible exception of purely thermal effects. Use of photochemical processes for growth of thin films is a relatively recent development,[23] and, as applied in MBE deposition, has been characterized as being in its infancy.[24] Thus it is not surprising that extensive searches of the thin film semiconductor growth literature have shown only limited application of the potential photochemical effects which can be exploited. For this reason, the next sections will describe the types of photo-enhancement effects that can occur.

Current literature on the photo-enhanced growth of thin films can be classed into five basic categories: thermal effects (both equilibrium and non-equilibrium), enhanced atom mobility, photolytic and enhanced pyrolytic decomposition effects, dopant activation, and other photochemical effects. In a number of cases these effects are thought to occur in combination.[25, 26] The first four subsections of this report will be limited to situations where these photochemical effects have been explicitly observed during thin film growth. The fifth section will discuss other photochemical processes which have not been explicitly observed in thin film growth, but which might be utilized to enhance the processes of thin film deposition.

Thermal Effects. Purely thermal effects are those attributed to heating of the substrate by absorption of the incident photons. This may take the form of near-equilibrium heating of substrates by lamps,[26–28] or involve the use of lasers and is categorized either by plasmas[29, 30] or extreme localized heating and/or melting of the surface.[28] The heating effects exploited with lamps of various types are used for technological reasons (*e.g.*, high heating rates,[28] low thermal mass, or materials service compatibility[27]) rather than specific effects on the growth processes. Laser thermal processing is used especially where the localized nature of the heating can be exploited.[28]

Enhanced Atom Mobility. Enhancement of the mobility of atom species on the growth surface is a fairly new but rapidly increasing application of photo-enhanced growth. Illumination of species on the growing surface can produce activated species which increases the rate of surface diffusion and thus improve crystal quality,[31-33] even to the point of crossing the transition from polycrystalline to single crystal growth.[26] Though less often observed, this phenomenon can also occur in the bulk (i.e., not during growth).[34] This enhanced diffusion phenomenon has also been observed to cause ordering in vacancy-donor complexes in CdTe.[35] A related phenomenon is the enhancement of desorption of certain adsorbed species.[32–33]

Photolytic Decomposition. Photolytic decomposition or photo-enhanced pyrolytic decomposition coupled with the use of metallorganic precursor compounds is the most common use of photo-enhancement during deposition. By choosing the proper illuminating wavelength(s) and precursor species the deposition will be enhanced or even selectively controlled by the illumination of the substrate.[23] Light sources that have been used have been lasers,[23] disk-shaped plasmas,[25] or arc lamps.[26]

Photolytic processes are not restricted to decomposition of metallorganic sources. For example, photolytic decomposition as been observed in Ga_2 vapor at relatively low energies of $\approx$25,000 cm^{-1} (3 eV or 400 nm).[36] These processes have also been used in the deposition of such materials as amorphous Si[37] and AlN.[31] Two photon process dissociation has also been observed for a number of cases,[38] which could be applicable in cases of laser illumination.

While strictly not a decomposition reaction, a somewhat related phenomenon is the photo-excitation of atomic or molecular species. The energies and absorption cross-sections for many common atoms and simple molecules are described in *Photochemistry of Small Molecules* by Hideo Okabe.[39] Such processes have been presumed to be a part of the growth effects observed in deposition of ZnS from elemental sources.[32]

Dopant Activation. An as-yet unexplained mechanism utilized in photo-assisted growth processes has been dopant activation during photo-assisted MBE. This process was developed for substitutional doping in II-VI compound semiconductors in the Physics department at NCSU in the research group headed by Dr. Jan Schetzina.[40, 41] They have achieved, among other things, hole concentrations (>2×10^{18} cm^{-3}) in *p*-type CdTe of ~100× larger than conventional thermal equilibrium bulk methods.[42]

Photo-assisted dopant activation has since been observed in other systems. Yamazaki *et al.*[23] achieved growth of Si with completely activated boron which produced carrier concentrations of up to 1.5×10^{20} cm^{-3} by UV irradiation. Subsequent fabrication of bipolar transistor structures resulted in ideality factors of $\approx$1.0. Enhancement of dopant incorporation was also observed by Fujita *et al.*[43] in growth of ZnSe. They reported enhanced incorporation of intentional and unintentional doping levels depending on the wavelengths of the illumination used. However, it is not clear whether the observed effect was electrical activation of dopants present and/or enhanced incorporation of intentional/unintentional dopant atoms.

A number of other photochemical effects have been observed which perhaps have not been effectively applied to problems in thin film growth. These effects will be discussed in this next section.

Other Photochemical Effects. As Giles *et al.*[40] pointed out in their paper describing the photon-induced electrical activation of dopants, there are a large number of photochemical

effects which can occur during growth. In addition to the effects already discussed above, they also listed modification of the electrical potential of the surface through the generation of electron-hole pairs and photochemical changes in atomic bonding.

Photo-generation of electron-hole pairs can be exploited to good effect by migration of these generated carriers to the interface, where they become localized and break bonds. One long established (since mid-60's or before) application combines this effect with an electrochemical cell to cause oxidation, etching or deposition in semiconductors.[44] The actual reaction that would occur being dependent upon carrier type and solution chemistry.

An application of this effect which occurs entirely in the solid state (first observed in 1966) involves so-called "photodoping" which is the term applied to the photo-activated diffusion of Ag in chalcogenide and some other glasses. Though there are differences in the proposed models regarding the diffusion of the Ag in the bulk, the consensus of opinion is that the initial entry of the Ag into the glass is caused by photo-generated carriers diffusing to the interface.[45–47]

A more thin film or vacuum deposition-related application of the same phenomenon is described in the study of the photochemistry and/or photocatalysis of molecules adsorbed onto surfaces. The reader is referred to the excellent review of photocatalytic reactions on semiconductors by Wolkenstein[48] for a more complete discussion of these effects which also includes examples. One minor flaw in Wolkenstein's treatment pointed out by Morrison[49] is the use of the Fermi level as a dominant variable, since the Fermi level is sensitive to so many variables.

An example from the photochemistry literature is the study made by Ho on the photochemistry of NO adsorbed onto Si(111)7×7.[50] He found that adsorption of NO increased the band bending occurring at the Si surface. Thus when the surface was illuminated, holes were rapidly accelerated to the surface before electron-hole recombination could occur, where the holes ruptured bonds causing the NO molecules to be desorbed and/or dissociated. This is illustrated schematically in Figure 1.

Ho also described the case of $Mo(CO)_6$ adsorbed onto Si(111)7×7, where the photochemistry of the adsorbed species could be affected directly. However, he pointed out that the photochemistry of adsorbed species need not be similar to that of the gas phase. A weakly physisorbed species would have a very similar photochemistry to that of a gas phase species. However, a more strongly physisorbed or even chemisorbed species would have a dramatically different photochemical response. Indeed, Cowen *et al.*[51] described the photochemistry of adsorbed species as "strongly perturbed." They noted that the changes could involve reaction inhibitions, enhancements, or even shifts in wavelength. For example, Cowin and co-workers[51] reported the photo-fragmentation of CH_3Cl on Ni at 248 nm, a wavelength that gas phase CH_3Cl does not absorb.

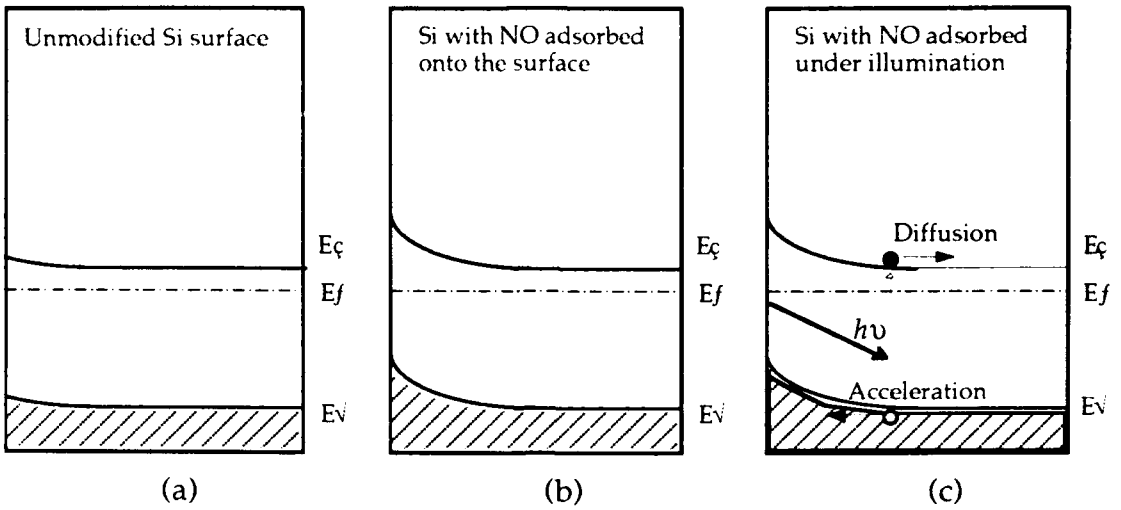

Figure 1. A schematic diagram of desorption of NO from Si surface due to the influence of photo-generated carriers (after Ho[47]). In (a) the normal Si surface, (b) NO adsorbed on the surface and increasing the band bending, and (c) photon created holes accelerate to the surface, causing bond rupture and desorption.

Examples from the thin film deposition literature include the photo-induced desorption reported by Matsumura *et al.*[33] in the growth of ZnS_xSe_{1-x} films. They did not determine if it was electron-hole mediated or direct photon desorption. Additionally, Celii *et al.*[52] reported that UV laser irradiation suppressed the formation of diamond in filament-assisted deposition. They determined that it was not a gas phase reaction, and speculated that the irradiation somehow removed potential nucleation sites, since diamond crystals from irradiated and unirradiated areas were otherwise similar in all respects.

Photo-induced changes in bonding need not only result in desorption/adsorption or dissociation. Much more subtle changes in bonding can be caused by illumination. Bicknell-Tassius *et al.*[35] reported the preferential orientation of photoluminescence defects occurred during photo-assisted MBE of CdTe. They postulated that vacancy-donor complexes were aligned along preferred crystallographic directions due to the irradiation.

Other much more subtle bonding changes have been observed as well. Feenstra and McGill[53] reported the dissociation of Zn–O defect pairs in GaP. They reported that these defect pairs which form as Zn on a Ga-site and O on an adjacent P-site can be dissociated by purely thermal means at ≈1000K. At lower temperatures (≈500K), the reaction will proceed via photoexcitation. They further reported that the defect pairs will reform, but at a larger separation distance.

The most unusual application of photon irradiation might well be the stimulation of a change in crystalline structure. This process was coined the "photophase effect" by Alfimov *et al.*[54] in 1984. They reported work by others on photophase changes including

condensation of gas phase molecules, crystallization of anthracene melts and a new crystalline phase of anthracene. Fleischauer[22] also reported work by others involving x-ray induced phase transformations in metal complexes.

Matsuda and Kikuchi[55] reported the first evidence of a photo-induced phase change in a simple binary system. They examined samples in the $As–As_2S_2$ system, and formed the new compound As_3S_2. Though the new phase is unstable at room temperature, they found that it was stable in the range of 150–190°C.

Conclusions on Photo-Enhancement. It is clear from the description and references given above that photo-enhanced growth processes can be extremely complex. The dynamic nature of these processes mean that without extensive study even simple predictions cannot be made regarding which source/material systems would be candidates for particular forms of photo-enhancement. However, it is also apparent from the examples cited that the advantages of photo-enhancement can be extremely important in producing the desired properties for a given materials system. The difficulties in applying photo-enhancement are several, but the advantages are unambiguous. These advantages may well be applied to the growth of c-BN films. Documented in the following sections are the initial observations of the photophase effect in BN growth.

B. Experimental Procedure

The primary deposition technique was GSMBE. Elemental boron and gallium were evaporated from effusion cells, and reactive nitrogen species were obtained by passing molecular nitrogen through a compact electron cyclotron resonance (ECR) plasma source. The growth system was a Perkin-Elmer 430 MBE system modified as described below. It consisted of three major sections: a load lock (base pressure $\approx 5 \times 10^{-8}$ Torr), a transfer tube (base pressure $\approx 3 \times 10^{-10}$ Torr) which was used to degas the substrates, and the growth chamber (base pressure $\approx 1 \times 10^{-10}$ Torr). The growth chamber was equipped with four standard 20 cc effusion cells and one high-temperature cell, the latter of which contained the B. All metals were contained in BN crucibles which were resistively heated either with Ta or W alloy wire heaters. The gallium cell was loaded with 50 g of 99.999 999% pure gallium.

The special high temperature cell noted above was monitored using a W3%Re-W26%Re thermocouple. Any decomposition of the crucible at the elevated operating temperatures did not affect the growth of the BN films. Prior to installation of the source, the BN crucible was loaded with 3 g of 99.9999% pure boron.

The more significant modification was the use of a compact ECR microwave glow-discharge plasma to dissociate/activate the N-containing gas. This source was designed and commissioned in an in-house effort by Dr. Zlatko Sitar.[56] This source has the advantages of fitting inside the nominal two-inch diameter tube of the source flange cryoshroud and thus

minimizes the source-to-substrate distance. As a result, the flux of activated/dissociated species arriving at the substrate surface is increased. This source was attached in place of a more traditional effusion (or cracker) cell for the group V element. The nitrogen gas was taken from a bottle of compressed UHP-grade nitrogen, purified by a metallorganic resin bed gettering material and subsequently regulated to the source by a variable leak valve.

Borazine ($B_3N_3H_6$) contained in a nitrogen carrier gas was also investigated for the deposition of BN, as this chemical is a source for both boron and nitrogen. Borazine was also chosen as a gas source in order to investigate both the activation of this material in the ECR plasma as well as attempt to determine if boron-nitrogen compounds provide a more suitable precursor, since the B–N bond already exists in the material. This was done by placing the borazine (which is liquid at STP) in a temperature controlled bubbler and passing nitrogen gas through it which then passed into the ECR source.

Substrate preparation involved a 30 min. exposure to UV which has been shown to remove hydrocarbon contamination,[57] followed by a dilute acid etch to remove oxide layers. In the case of Si, a solution of H_2O:HF (10:1) was used,[58] and for Cu, a solution of H_2O:HCl (10:1) was employed.[59] Subsequently, the substrates were mounted on a Mo holder using either molten indium or silver paste. Silver paste was very important for the copper substrates as they were extremely sensitive to oxidation and would oxidize heavily in attempting to indium bond the substrates.

Samples were then loaded into a cryopumped load lock. After the initial evacuation, the samples were loaded into the transfer tube where they were degassed to a temperature of 700°C. Immediately after degassing they were loaded into the growth chamber and the deposition cycle initiated. Typical deposition conditions used for both BN and GaN are shown below in Table I.

Table I. Deposition Conditions used in GSMBE of BN and GaN

Nitrogen pressure	$1–2\times10^{-4}$ Torr
Microwave power	20–50 W
Boron temperature	1725 – 1775°C
Gallium temperature (where used)	975 – 990°C
UV source power (where used)	500 W
Substrate temperature	400 – 700°C
Growth time (BN)	120 – 360 min.
Deposited film thickness	10–850 Å

The UV lamp, when used, was a 500 W high pressure Hg arc-lamp* with a collimating lens. The resulting spectral output is shown below in Figure 2. Note that the standard units for spectral irradiance are $\mu W\ cm^{-2}\ nm^{-1}$ and thus must be integrated to get power levels. This lamp was setup to illuminate the substrate surface from a sapphire viewport positioned normal to the growth surface. The sapphire window permitted transmission of the entire range of UV wavelengths. Accounting for the mounting geometry and the various losses (including the sapphire window) resulted in an overall illumination power (for the spectrum 200–900 nm) of ~0.5 W cm^{-2}.

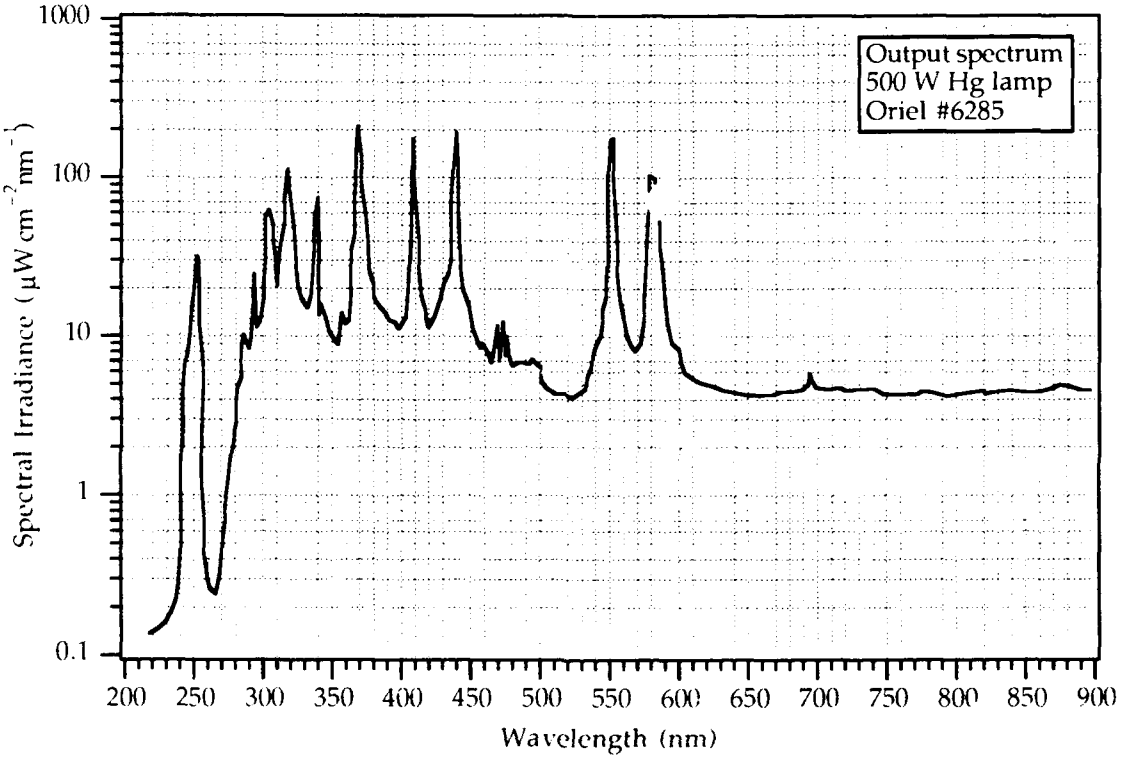

Figure 2. Spectral irradiance plot of the high pressure Hg arc lamp used for photo-enhanced deposition of BN films (After Oriel Corp. data for 500-W Hg-lamp).

Subsequent to deposition, the substrate would either be moved to the load lock for removal from the system or transferred to the analytical system for additional characterization.

* Model 6285 lamp in #66042 housing, Oriel Corporation, Stratford, CT 06497

C. Results

1. Boron Nitride

Boron Nitride on Copper. Figure 3 shows an XPS plot (Riber Mac2 analyzer) of BN deposited on a Cu(110) substrate. Note lack of contamination from carbon and oxygen as a result of the UHV deposition. Peak heights make it appear that the surface is primarily Cu. This is not strictly true, since the sensitivity factor for Cu-$2p_{3/2}$ is ~50× greater than that of B-1s and ~10× greater than N-1s. However, significant island formation of BN is strongly suggested.

X-ray spectra (Rigaku Geigerflex) of films grown at two different temperatures are shown in Figure 4. Note that the BN deposit seems oriented to the substrate given that only one reflection is present, but highly defective. This is from the fact that an ordinariiy forbidden reflection seems to be present. Deposition does not appear to be affected by the influence of the photon irradiation.

Deposition of BN on Cu (111) was also undertaken to determine effects of substrate orientation. X-ray diffraction showed that the films showed no cubic and were h-BN or t-BN (a planar disordered h-BN variant).

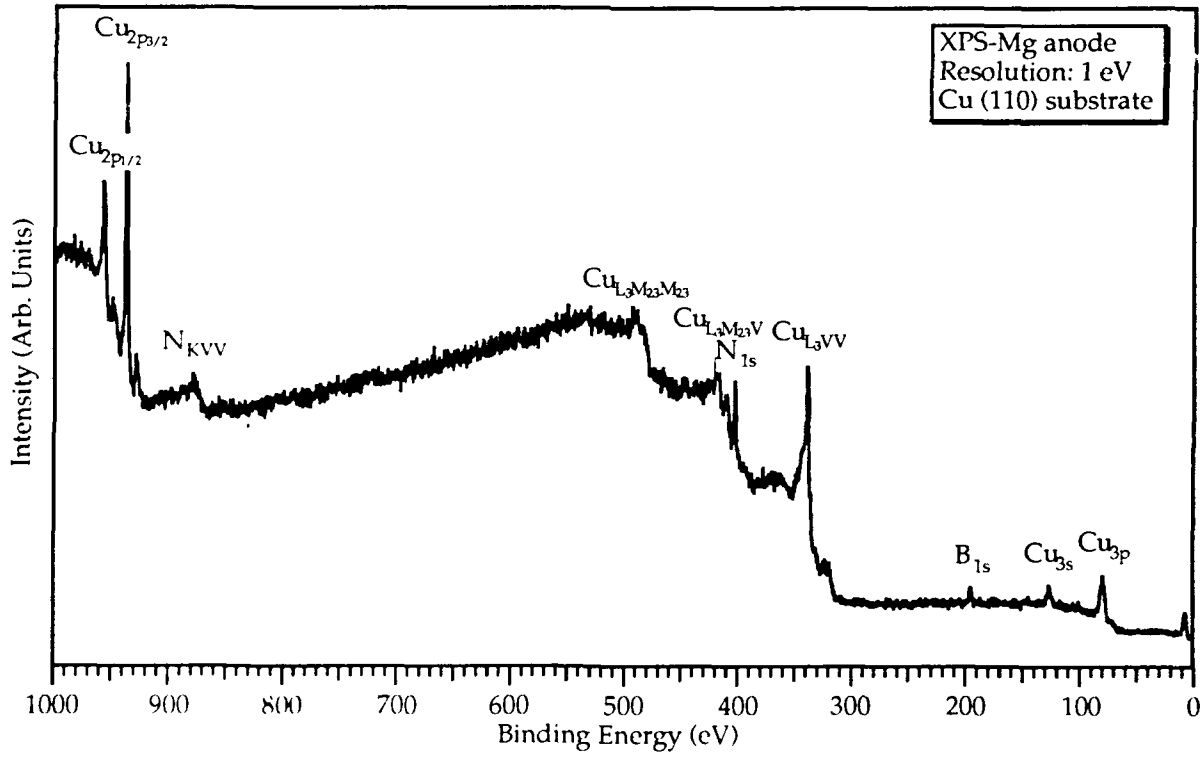

Figure 3 XPS spectrum of BN deposit on Cu(110) substrate. Cu-$2p_{3/2}$ sensitivity is ~50× greater than that of B-1s and ~10× greater than N-1s.

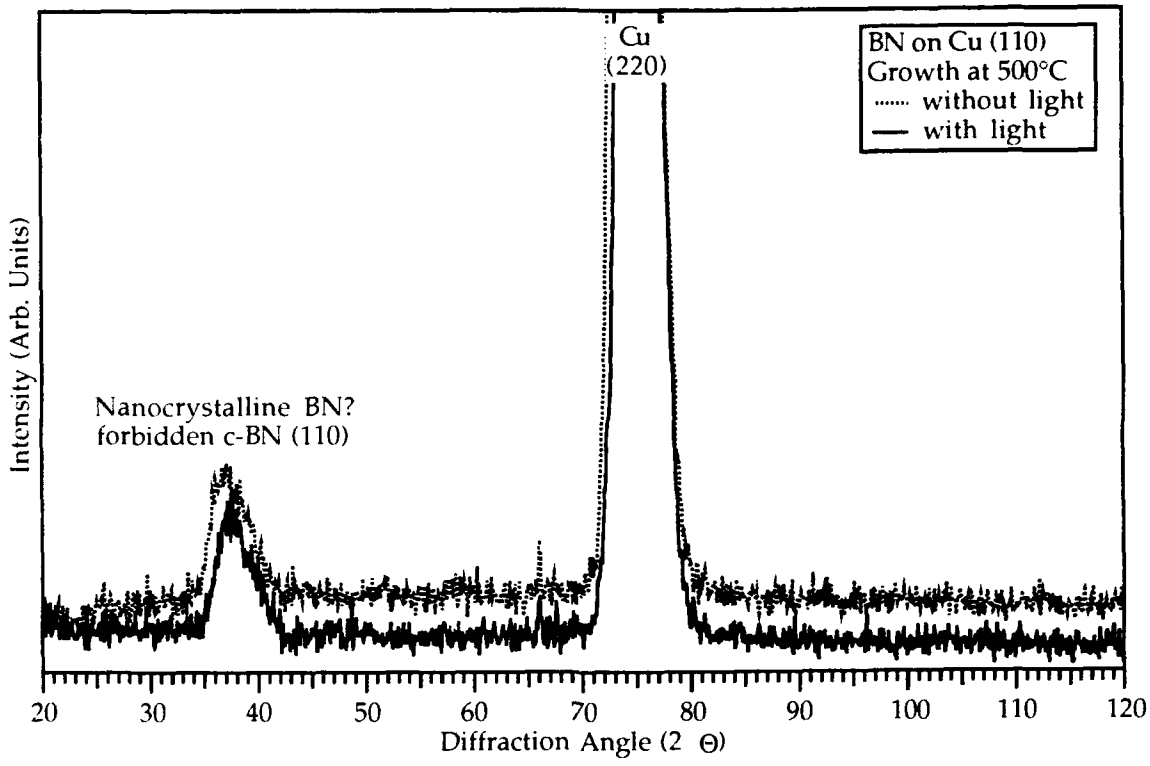

Figure 4. X-ray spectra (Cu K_α radiation) of BN on Cu (110) substrate.

Boron Nitride on Silicon (100). Previous reports from this research program described the FT-IR analysis of films deposited on Si(100). As shown in Figure 5, the films were primarily amorphous; however, they did contain some c-BN component, perhaps in nanocrystalline form.

Subsequent growths attempted to examine the differences that would evolve if the growth surface were illuminated by a high pressure Hg arc lamp. Field emission SEM (Hitachi S-4000) examination results are shown in the following figures. Films deposited without illumination at the higher growth rate are shown in Figures 6 and 7. In the former figure, the film appears free of gross features. However, in Figure 7, an extremely fine texturing on the surface is revealed.

The microstructure of the surface of a film deposited with illumination at the higher growth temperature (500°C) is shown in Figure 8. Since the morphology was essentially the same as Figure 6, a lower magnification micrograph is not shown. Again, the film shows an extremely fine texturing on the surface.

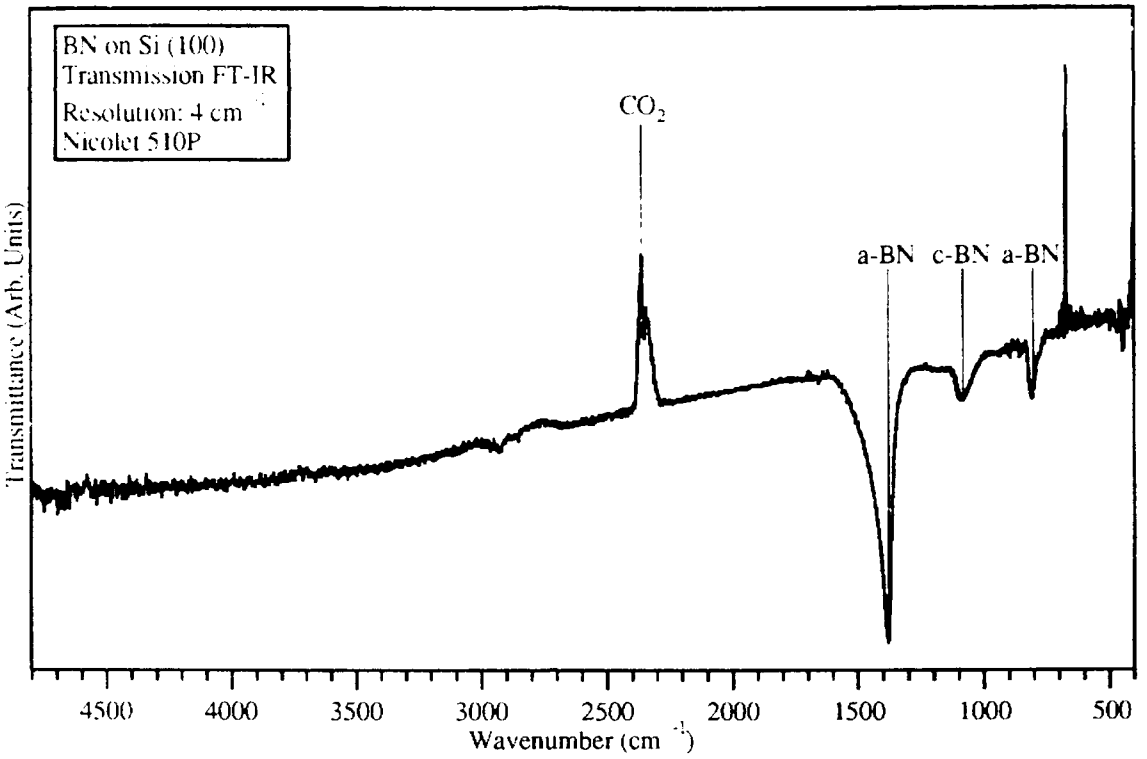

Figure 5. Transmission FT-IR spectra of BN deposited on Si (100) substrate. Inverted CO_2 absorption peak is present because concentration was lower when analyzing sample than for instrument baseline spectrum.

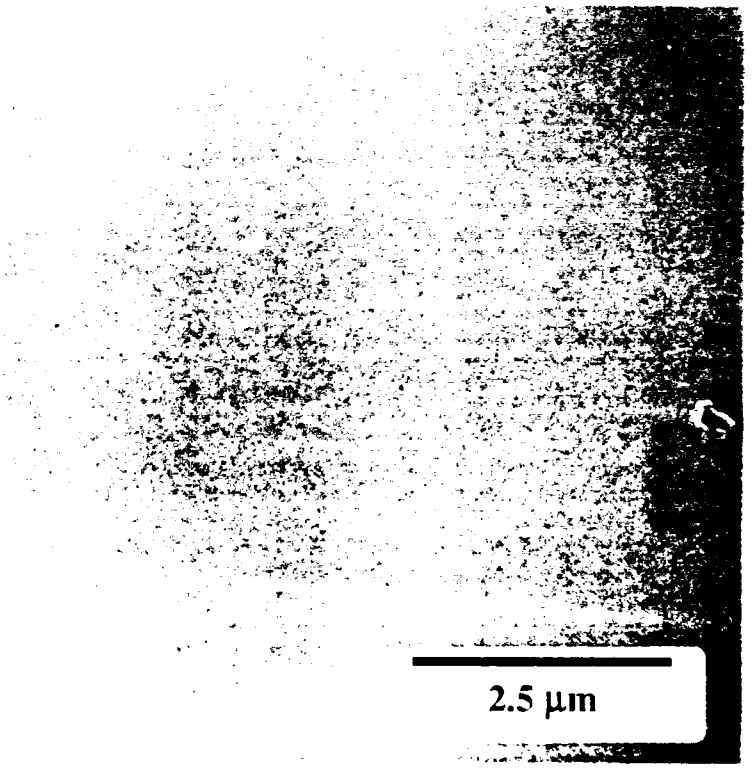

Figure 6. Secondary electron micrograph of surface of BN film deposited on Si (100) without additional illumination (growth at 500° C).

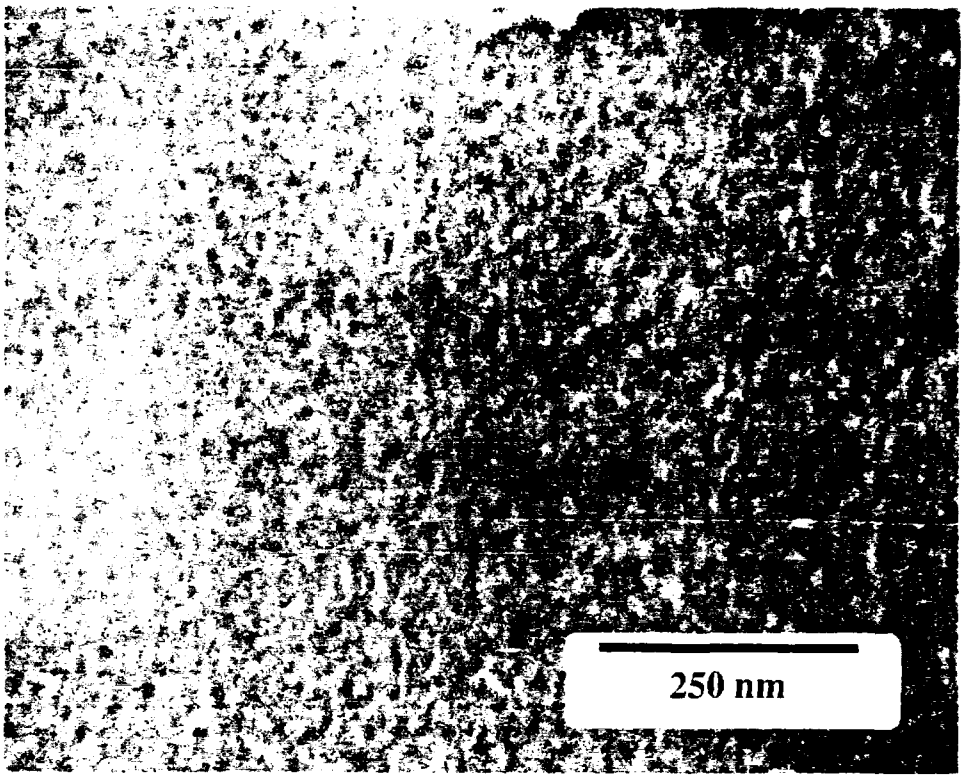

Figure 7. Secondary electron micrograph of surface of BN film deposited on Si (100) without additional illumination (growth at 500°C).

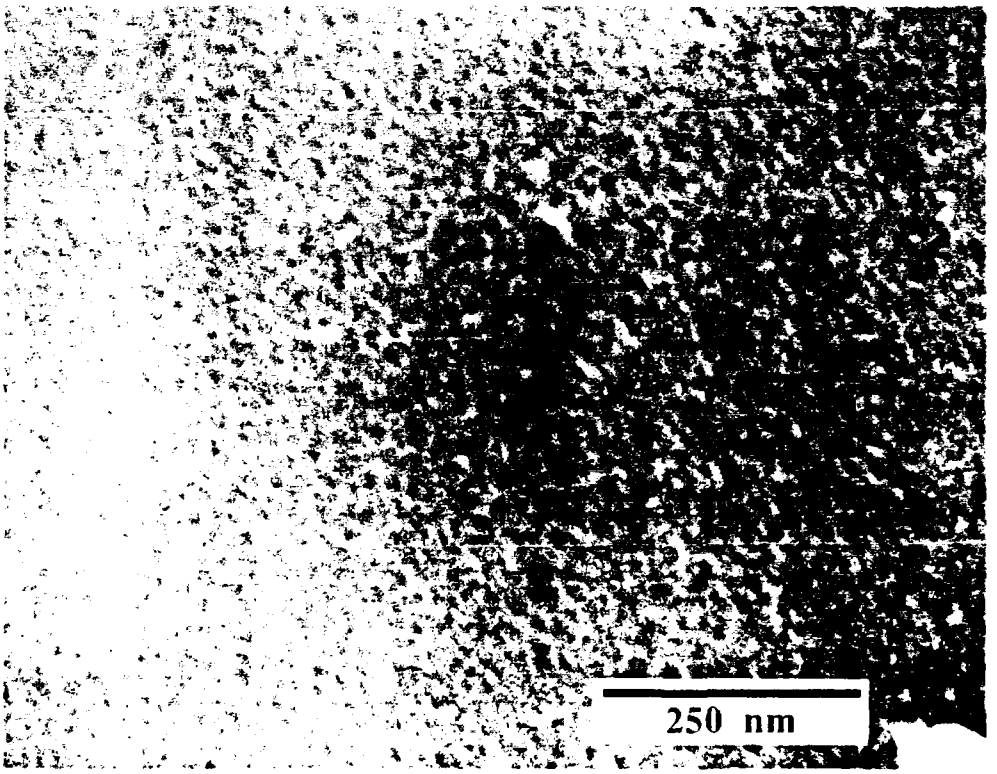

Figure 8. Secondary electron micrograph of surface of BN film deposited on Si (100) with additional illumination from the UV source (growth at 500°C).

Growth at a lower temperature (400°C) resulted in the surface morphologies shown in Figures 9 and 10. They reveal a small but discernable change from those shown in Figures 6-8. The higher magnification micrograph of Figure 10 shows small grains across the surface.

Figure 11 shows the surface microstructure for films grown at 400°C in tandem with the illumination from the arc lamp. The microstructure at low magnification was similar to that of Figure 9 and so is not shown. The microstructure is more like that of the films deposited at 500°C, than that of the 400°C film without illumination. However, the change in appearance is slight.

Shown in Figure 12 are the diffraction patterns from depositions at 500°C. Note that the sample with illumination fractured from handling which resulted in a high background at low angles due to the scattering from mounting clay. The interesting feature is that the c-BN (400) peak is not present except when the growth surface is photon irradiated.

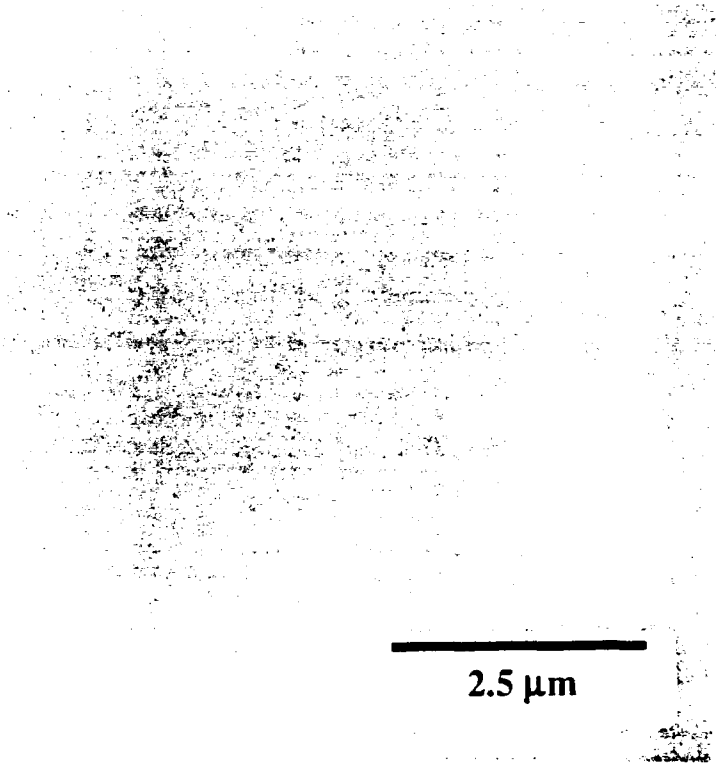

Figure 9. Secondary electron micrograph of surface of BN film deposited on Si (100) without additional illumination (growth at 400°C).

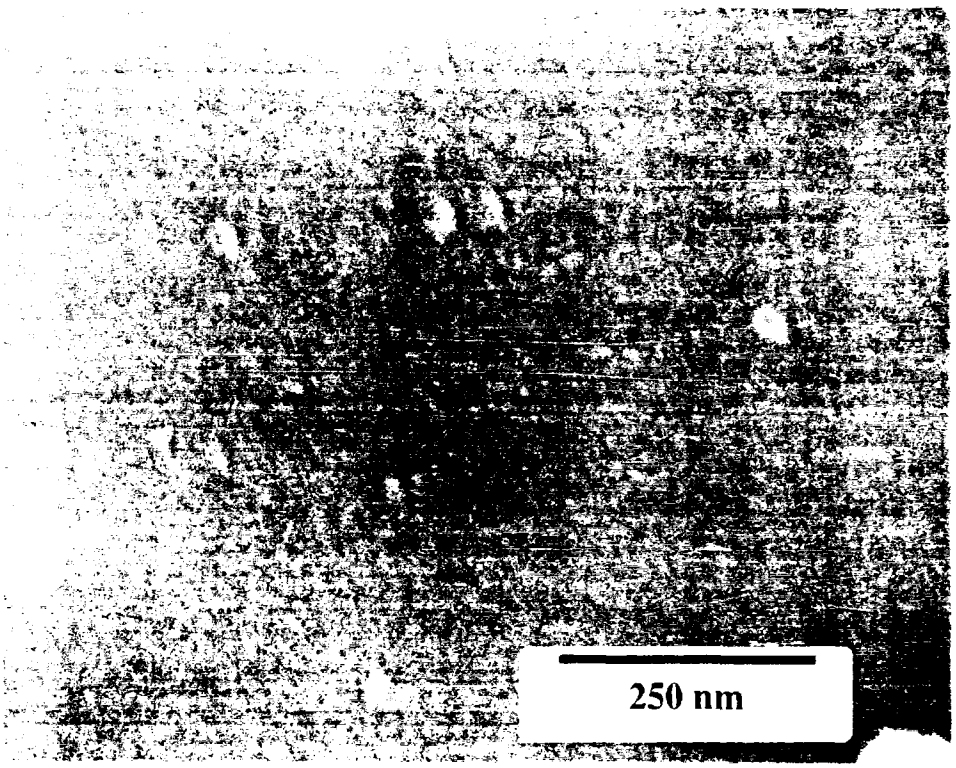

Figure 10. Secondary electron micrograph of surface of BN film deposited on Si (100) without additional illumination (growth at 400°C).

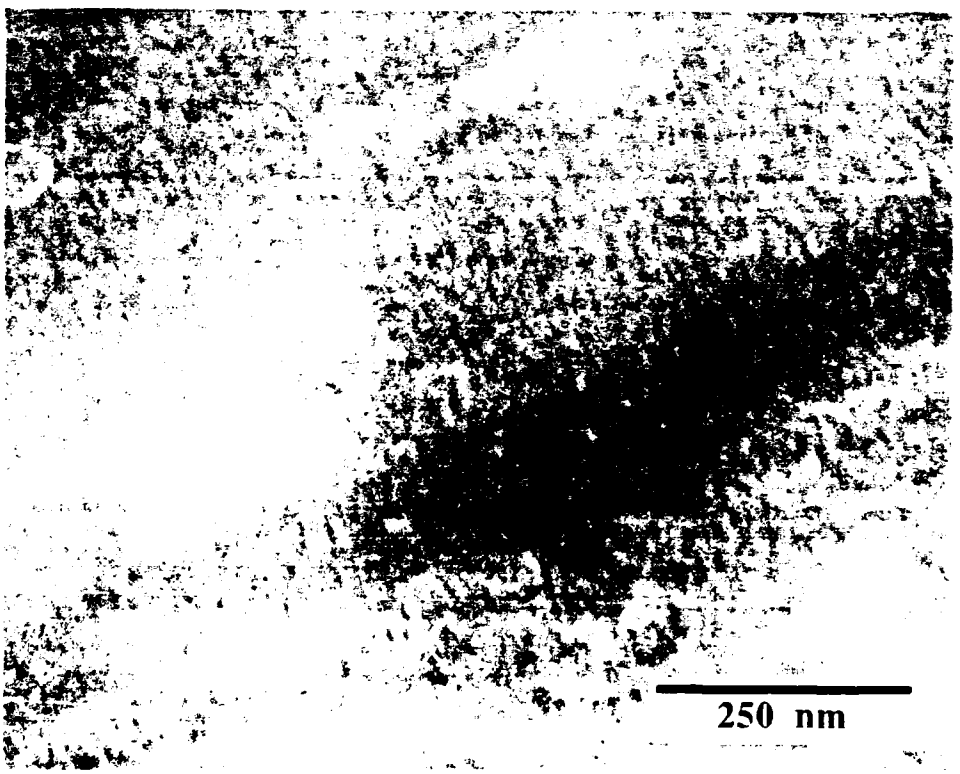

Figure 11. Secondary electron micrograph of surface of BN film deposi[illegible]n Si (100) with additional illumination (growth at 400°C).

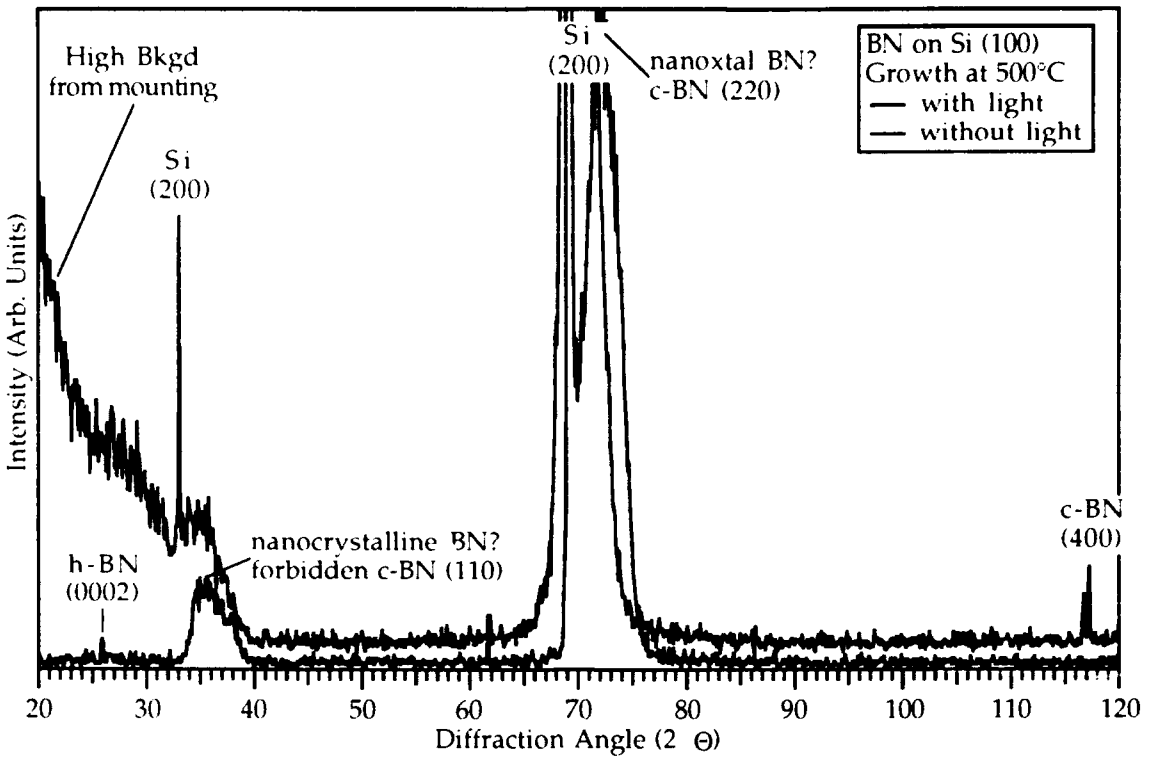

Figure 12. X-ray diffraction patterns (Cu K_α radiation) of BN deposited on Si (100) at 500°C with and without illumination from the Hg arc lamp.

Samples were next compared at a lower growth temperature to determine its impact on the phase formation. Figure 13 shows patterns from depositions at 400°C. The h-BN phase is apparently much more well crystallized at this lower temperature, based on the narrow linewidth of the h-BN (0002) peak. In both cases, the c-BN (400) peaks are present, but there is a dramatic decrease in the intensity of the h-BN (0002) peak for the illuminated case, indicating a strong inhibition of the formation of this phase.

The FT-IR spectra from the samples grown at 500°C are shown in Figure 14 and show that there is little else evident than the two phases of BN. Please note that peaks for amorphous BN coincide with those of h-BN and thus are not differentiated in these spectra (see discussion).

The FT-IR spectra for the samples grown at 400°C are shown in Figure 15 and show a much more complex structure. Note the many water and carbon dioxide peaks are from a purging problem in the optical analysis bench and can be ignored. Interestingly, the complex peak structures for the unirradiated case disappeared for the case when the photon irradiation was used. This is not contamination as has been shown in many previous reports from XPS spectra.

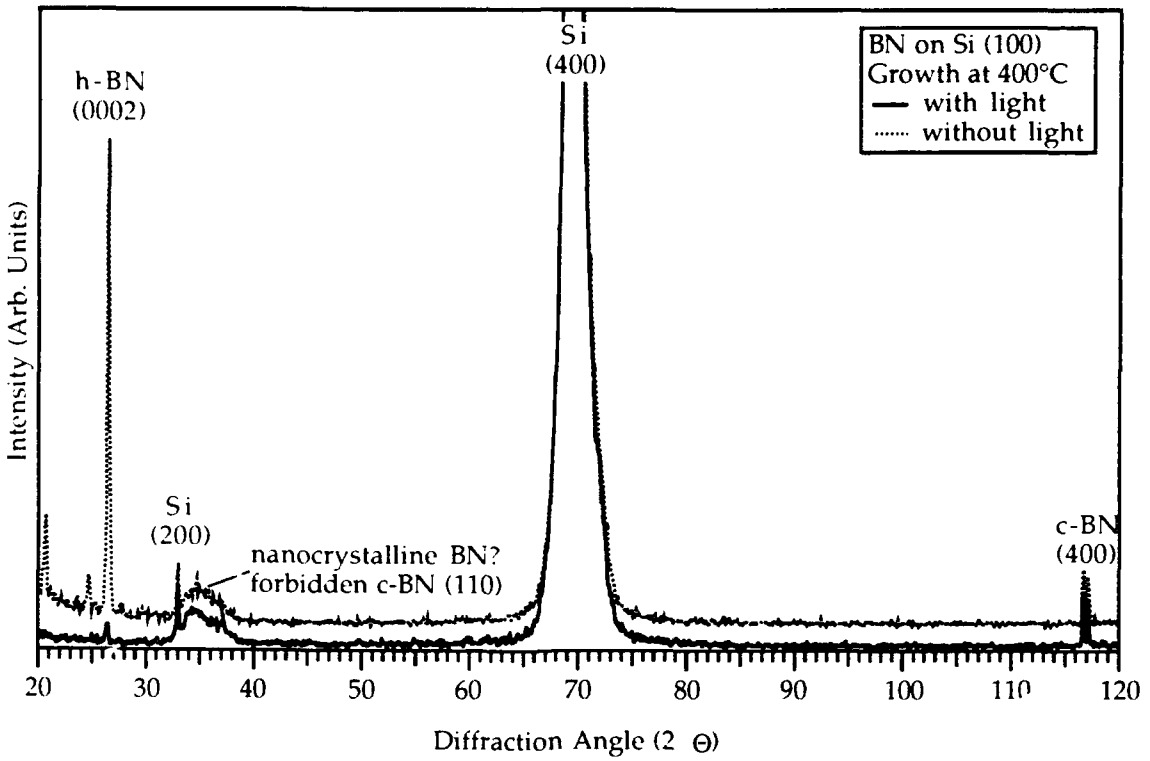

Figure 13. X-ray diffraction patterns (Cu K_α radiation) of BN deposited on Si (100) at 400°C with and without illumination from the Hg arc lamp.

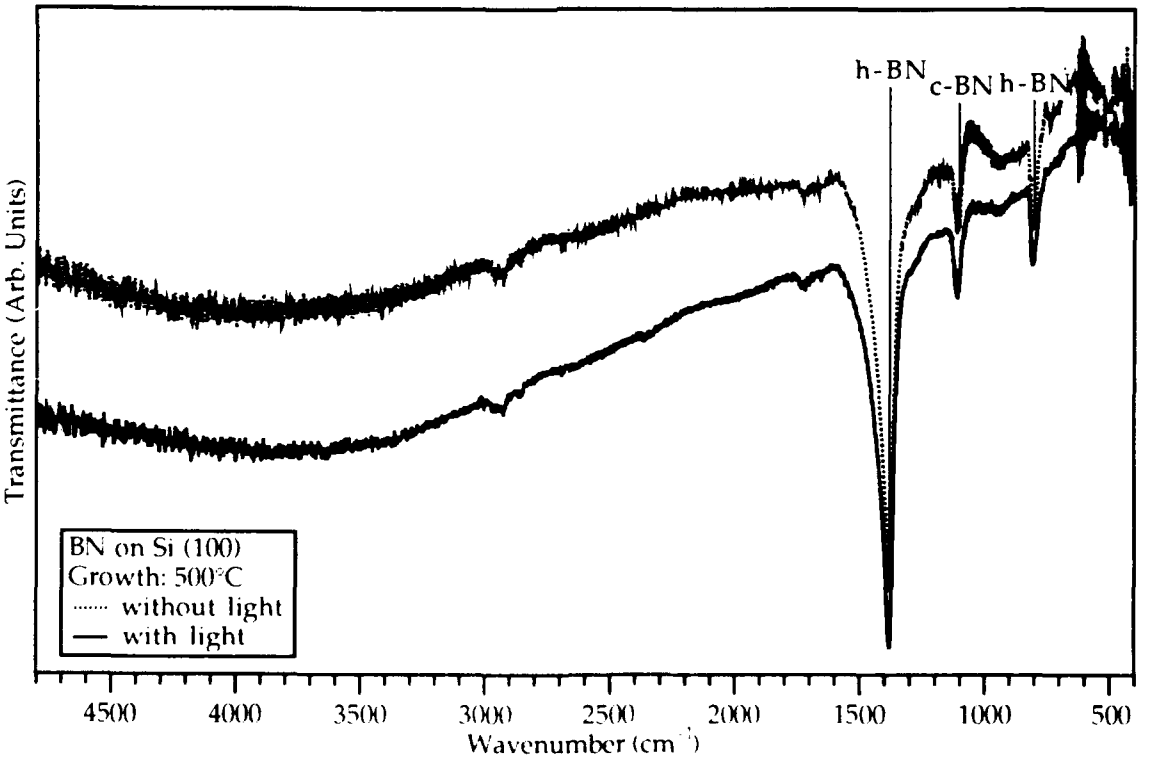

Figure 14. FT-IR spectra (Nicolet 510P) of BN on Si (100) deposited at 500°C.

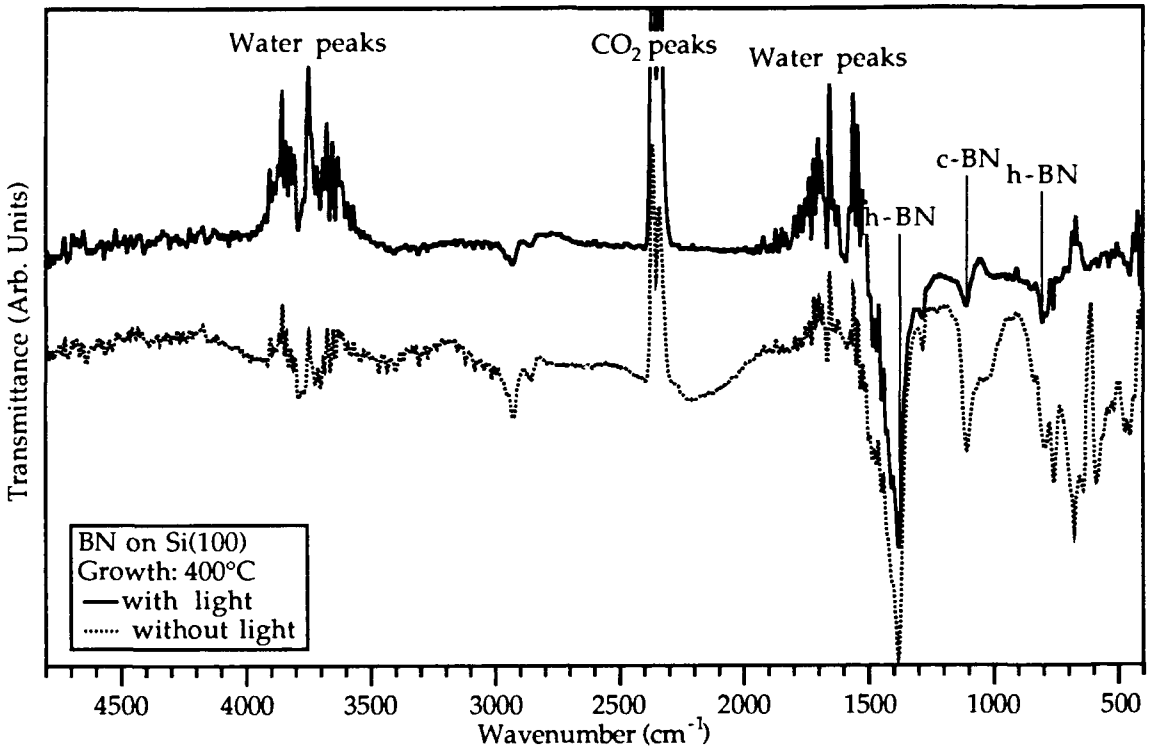

Figure 15. FT-IR spectra (Nicolet 510P) of BN on Si (100) deposited at 400°C. Spectra corrected for background shift and slightly smoothed.

2. Gallium Nitride

The XPS spectra in Figure 16 show no noticeable differences between films deposited with and without the lamp illumination.

Field emission SEM (Hitachi S-4000) examination results are shown in the following figures. Films deposited without illumination at the higher growth rate are shown in Figures 17 and 18. The film appears free of gross features in Figure 17, but Figure 18 shows an angular texture indicative of a polycrystalline film.

Films deposited with illumination at the higher growth rate are shown in Figures 19 and 20. Again, the film appears free of gross features in Figure 19, but Figure 20 shows a different angular texture indicative of a polycrystalline film, as before, yet certainly different in some respects.

Films deposited without illumination at the lower growth rate are shown in Figures 21 and 22. The film appears much flatter than at the higher growth rate and with a significantly different texture. Large crevice-like features are also clear in Figure 21. Figure 22 shows the texture tends to be in two directions, but with smaller areas with a different texture.

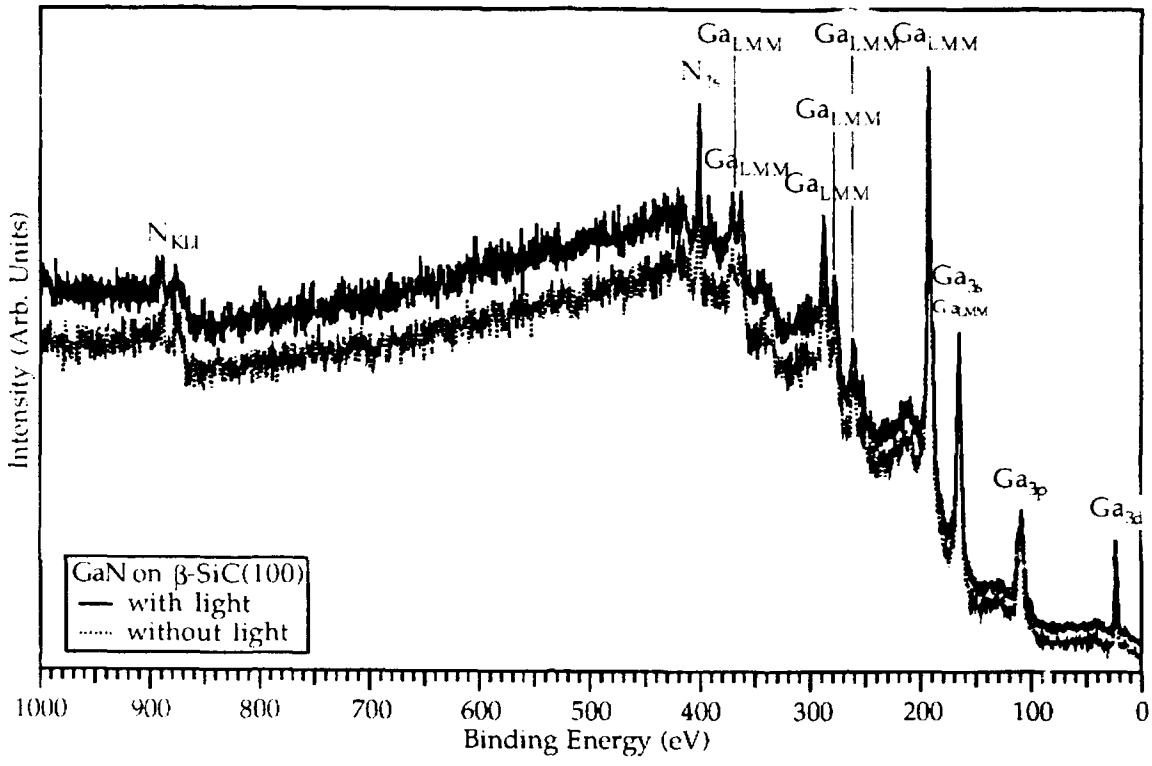

Figure 16. XPS spectra of GaN on β-SiC(100) deposited with and without illumination from 500-W Hg-arc lamp.

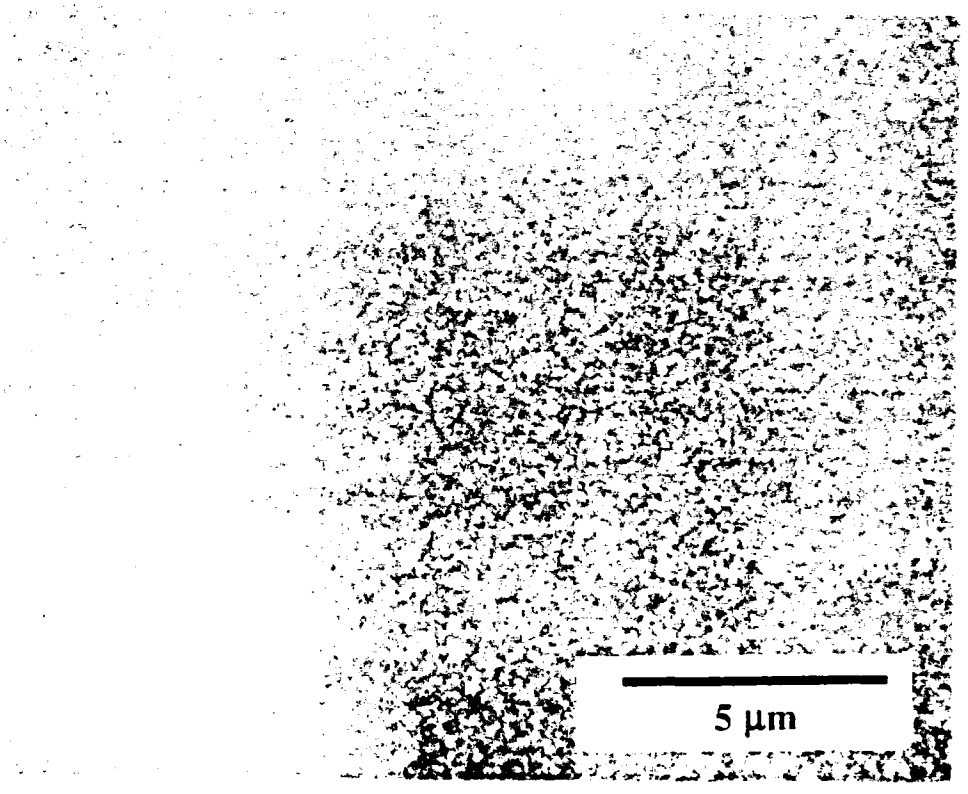

Figure 17. Secondary electron micrograph of surface of GaN film deposited on β-SiC (100) without additional illumination (Ga cell @ 990°C).

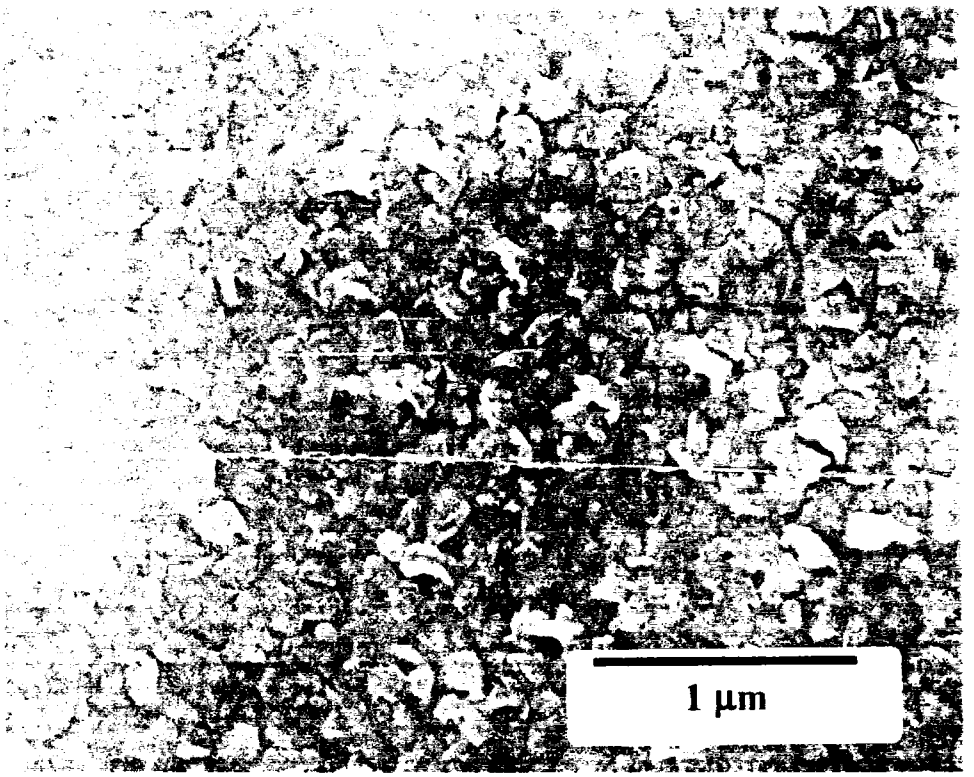

Figure 18. Secondary electron micrograph of surface of GaN film deposited on β-SiC (100) without additional illumination (Ga cell @ 990°C).

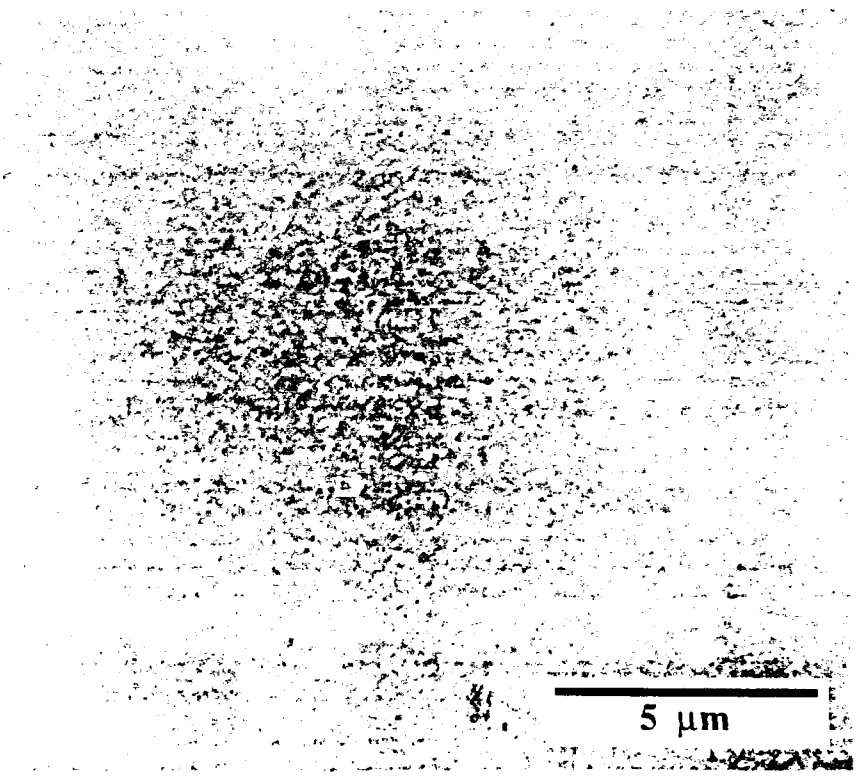

Figure 19. Secondary electron micrograph of surface of GaN film deposited on β-SiC (100) with additional illumination (Ga cell @ 990°C).

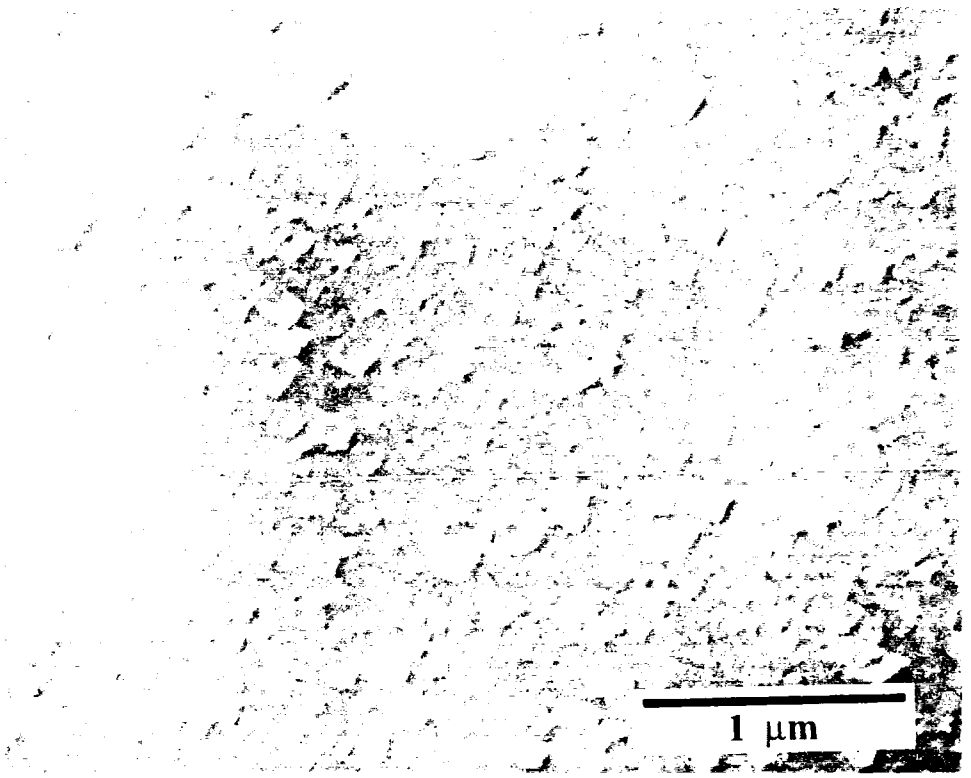

Figure 20. Secondary electron micrograph of surface of GaN film deposited on β-SiC (100) *with additional illumination* (Ga cell @ 990°C).

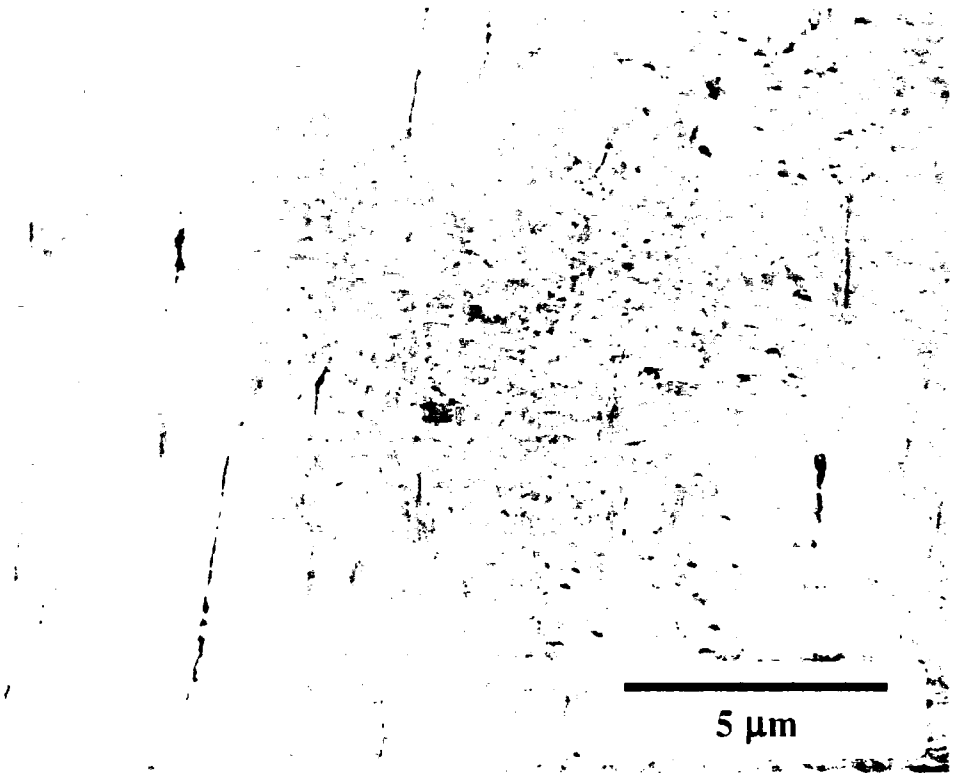

Figure 21. Secondary electron micrograph of surface of GaN film deposited on β-SiC (100) without additional illumination (Ga cell @ 975°C).

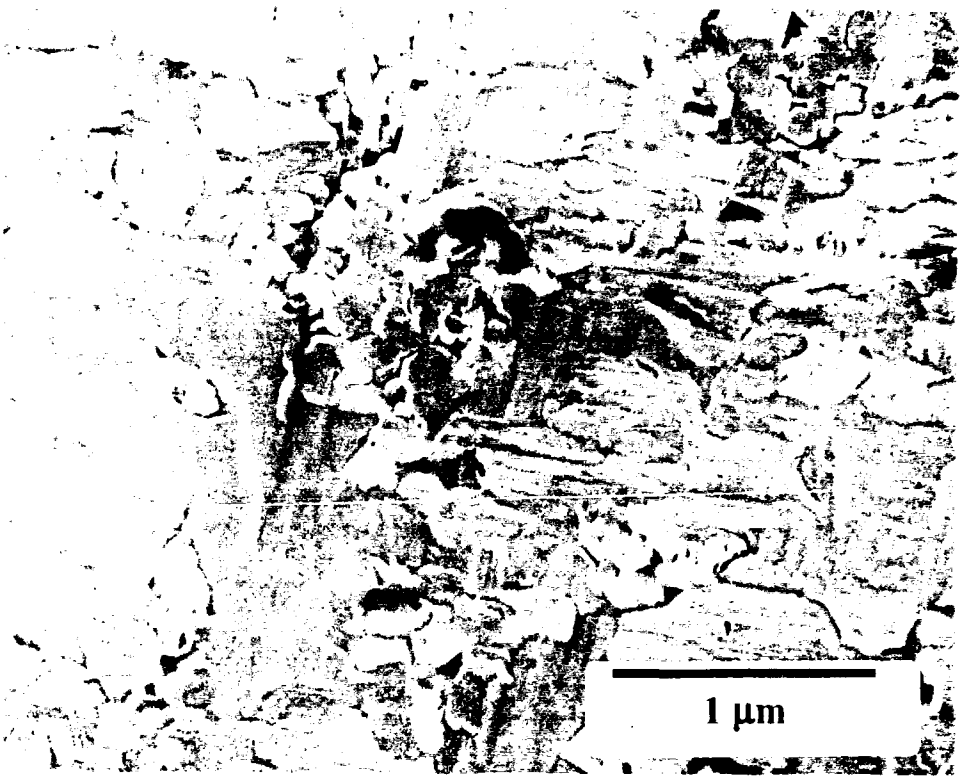

Figure 22. Secondary electron micrograph of surface of GaN film deposited on β-SiC (100) without additional illumination (Ga cell @ 975°C).

Films deposited with illumination at the lower growth rate are shown in Figures 23 and 24. The film appears much smoother in Figure 23 than in previous figures with only a few small hillock-like features spread across the surface. Figure 24 reinforces this view, but also shows the presence of a subsurface texture.

Subsequently the samples were measured for deposition thickness using backscattered electron imaging in a field emission SEM (JEOL 6400F). These results are shown in Table II along with comparison values obtained from XTEM research described later. It appears that the addition of the photon irradiation decreases the growth rate by approximately 10–15%.

Table II. Thicknesses of GaN layers deposited under listed conditions measured by backscattered electron imaging and cross-section TEM.

Conditions\Technique	BEI-SEM	XTEM	Growth rate
Ga@990°C w/o light	550 nm	550 nm	183 nm/h
Ga@990°C w/ light	500 nm*	450-500 nm*	161 nm/h
Ga@975°C w/o light	400 nm	420 nm	137 nm/h
Ga@975°C w/ light	360 nm	350 nm	118 nm/h

* Increased surface roughness made this measurement difficult.

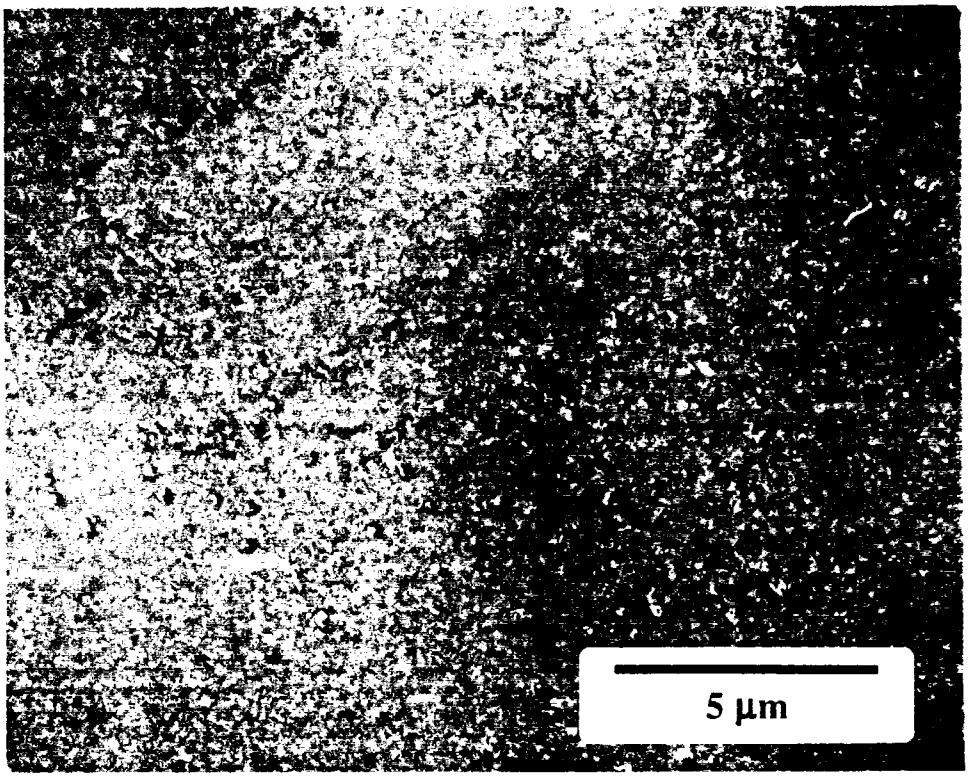

Figure 23. Secondary electron micrograph of surface of GaN film deposited on β-SiC (100) with additional illumination (Ga cell @ 975°C).

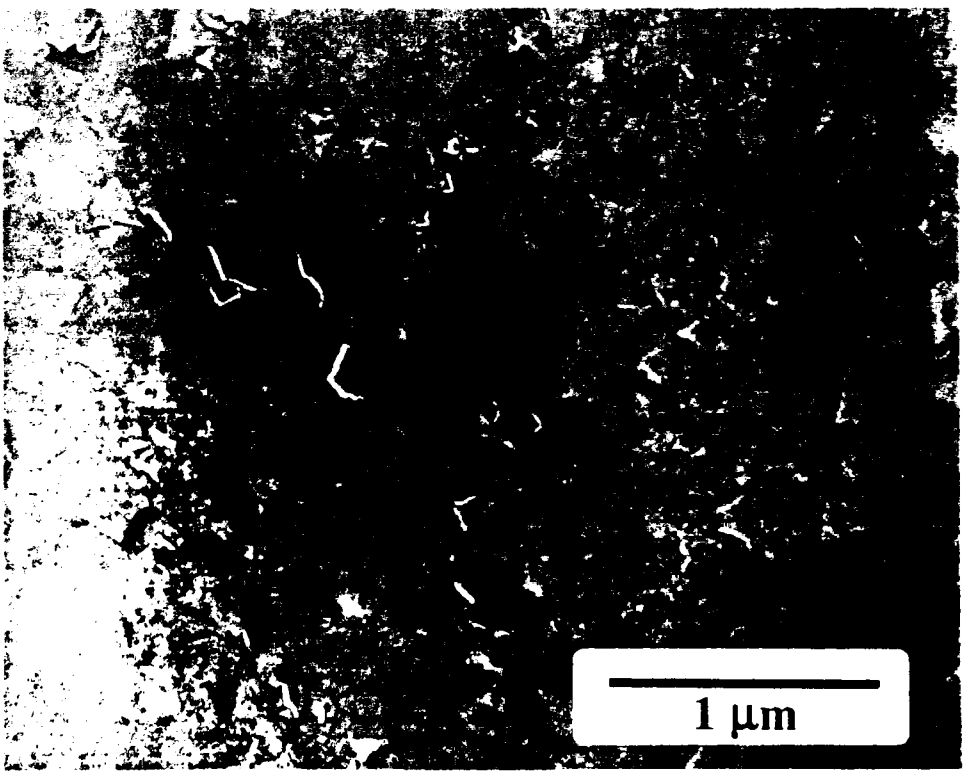

Figure 24. Secondary electron micrograph of surface of GaN film deposited on β-SiC (100) with additional illumination (Ga cell @ 975°C).

X-ray diffraction results (Rigaku Geigerflex) using $Cu_{K\alpha}$ radiation for these samples is shown in the following Figures 25 and 26. Note the dramatic change in x-ray intensities of the GaN peaks when illumination was used. These changes indicate a change in orientation of the GaN with respect to the β-SiC substrate.

Finally XTEM samples were prepared using standard techniques and observed in a STEM-style analytical TEM (Hitachi H-800). Most of these samples appeared polycrystalline in nature, with some texturing apparent. Measurement of grain size was made extremely difficult due to the small electron transparent areas of these samples, but they are estimated to be ~0.25 μm.

Figure 27(left) shows the SAD pattern from a single grain of GaN superimposed upon the β-SiC substrate pattern. This pattern shows when compared to the modeled pattern on the right that the orientation is GaN (0001)||β-SiC(100). Rather than a true wurtzite (2H) phase, a related 4H-GaN phase was formed. RHEED performed after growth and TEM observations in other areas confirm that the film is polycrystalline but maintains this basic orientation. Measurement of the diffraction spot radii would seem to indicate the formation of a hexagonal GaN polytype.

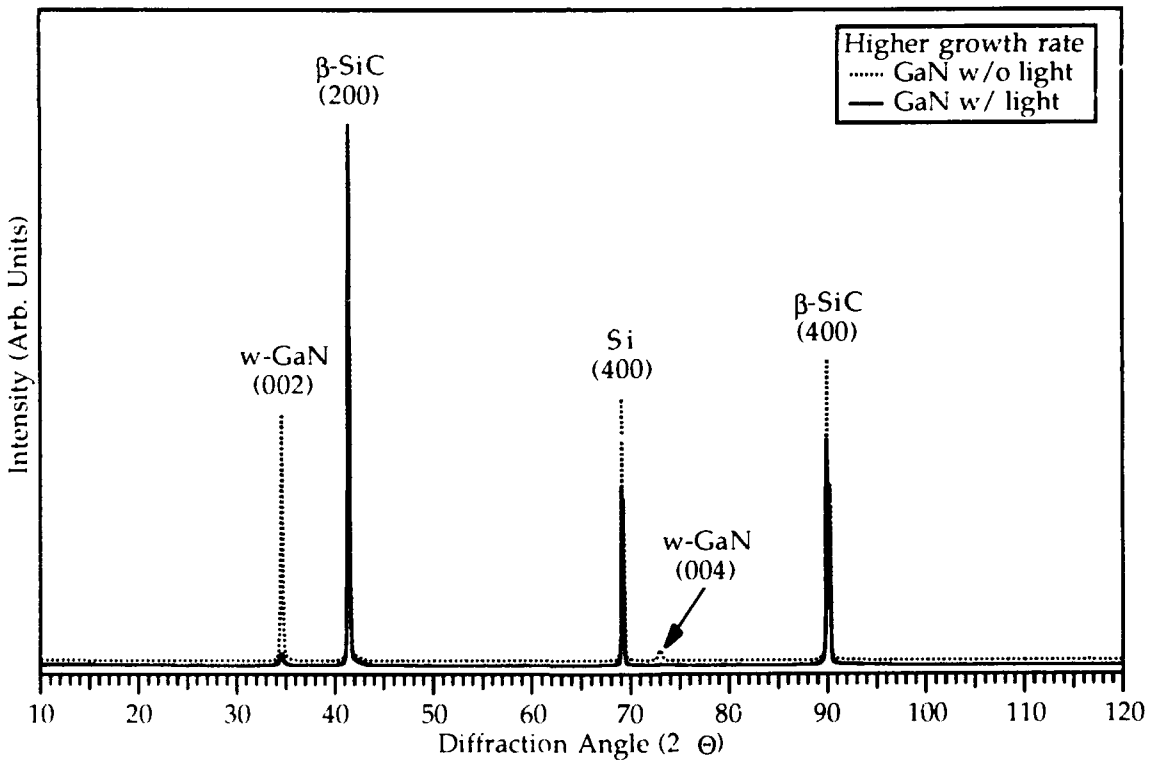

Figure 25. X-ray spectra of GaN on β-SiC(100) deposited with and without illumination from 500-W Hg-arc lamp at the higher deposition rate (Ga cell @990°C).

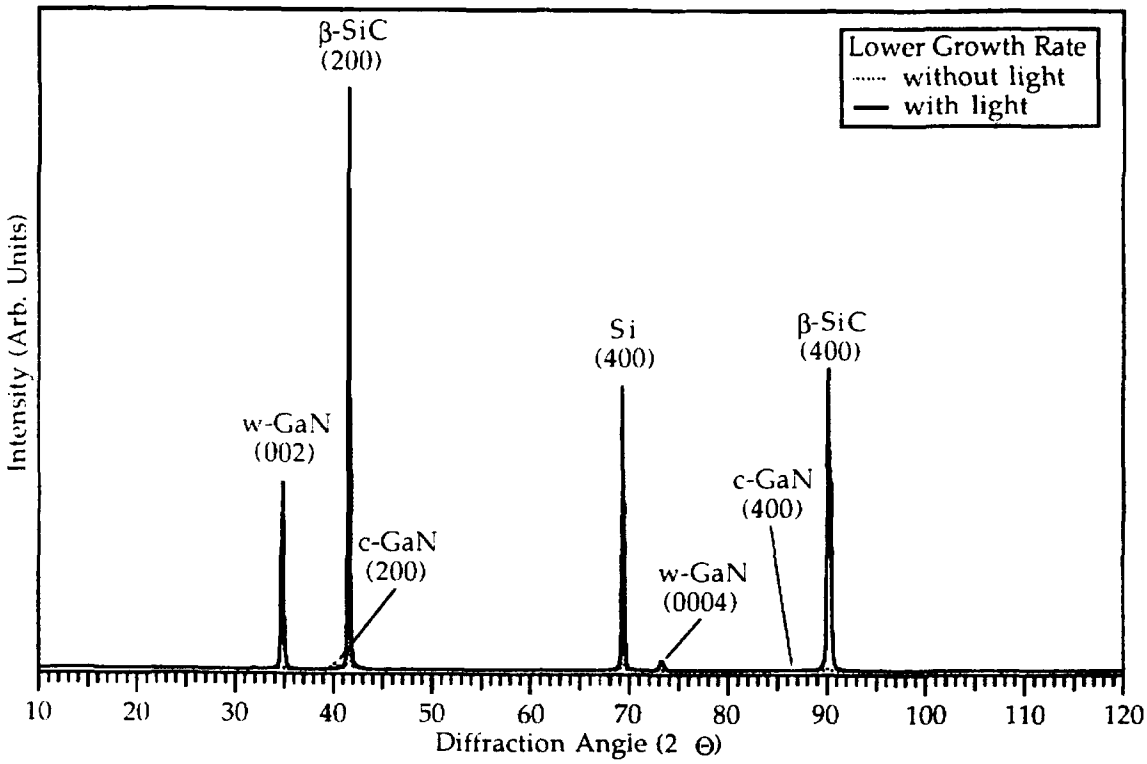

Figure 26. X-ray spectra of GaN on β-SiC(100) deposited with and without illumination from 500-W Hg-arc lamp at the lower deposition rate (Ga cell @975°C).

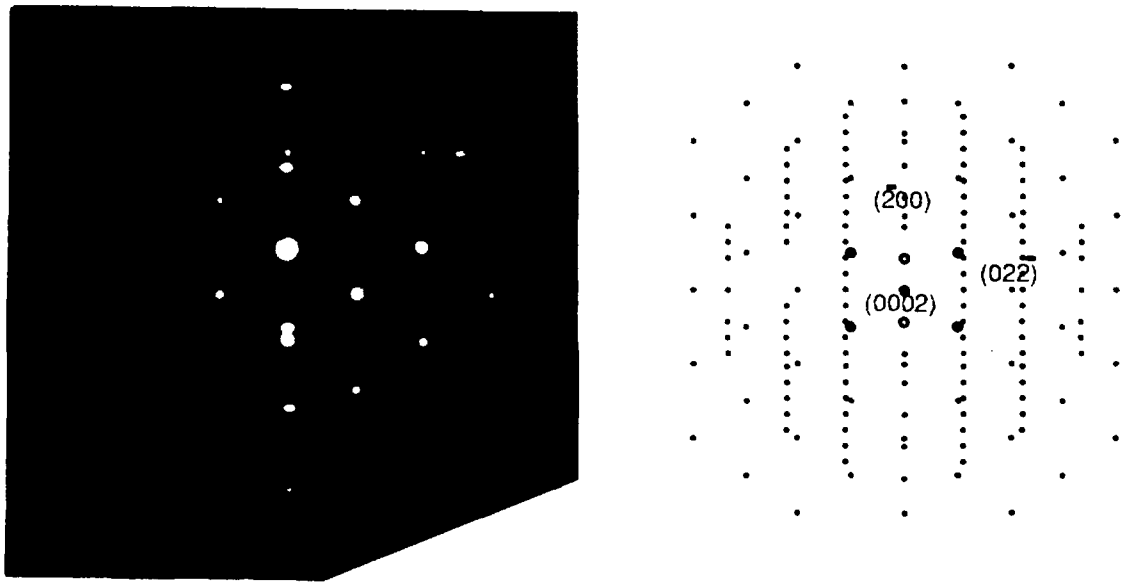

Figure 27. SAD pattern from one polycrystalline grain of GaN on β-SiC (100) at lower growth rate (Ga @975°C) without illumination during growth. Left: Real pattern. Right: Model showing orientation (z=[011]).

Figure 28(left) shows the SAD pattern from a polycrystalline region of GaN superimposed upon the β-SiC substrate pattern. Very dim spots near the center confirm the

continued presence of 4H-GaN from the (0002) reflection. The three rings correspond to the $(10\bar{1}0)$, $(10\bar{1}1)$, and $(20\bar{2}0)$ rings. This much more random pattern is reflected in the roughness of the surface observed in SEM and the much reduced diffraction intensities. RHEED performed after growth also confirmed the polycrystalline nature of the film.

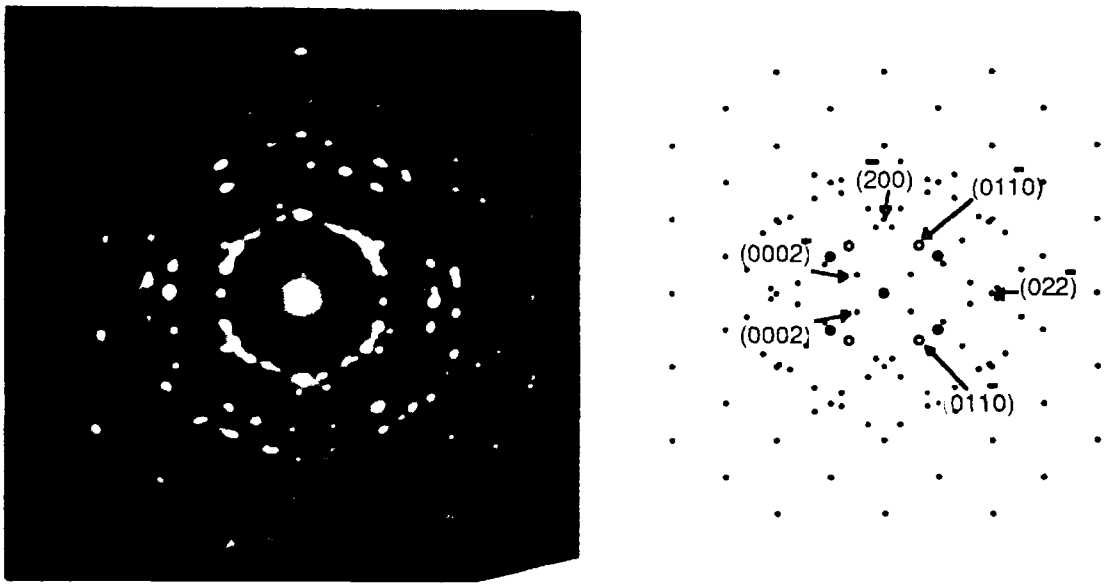

Figure 28. SAD pattern from polycrystalline patterns of c-GaN and 4H-GaN on β-SiC (100) at lower growth rate (Ga @975°C) with illumination during growth. Left: Real pattern. Right: Model showing orientation (z=[011]).

TEM confirmed the x-ray diffraction analysis as well as the SEM observations indicating that in some regions the film was 4H-GaN and in other regions the film was cubic GaN. In regions where the film was cubic GaN, the previously observed orientation was seen, namely (200)||(200) and $(02\bar{2})||(02\bar{2})$. Figure 29(left) shows the SAD pattern from a 4H-GaN region superimposed upon the β-SiC substrate pattern. This pattern, when compared to the modeled pattern on the right, shows that there are two orientations of the 4H-GaN to the β-SiC substrate. This pattern is very similar in general appearance to that for the cubic GaN case and explains why it would be difficult to differentiate the patterns using RHEED. The relationships observed are as follows: $(1\bar{1}\,1)||(0004)$ and $(600)||(03\bar{3}8)$ as well as $(11\,\bar{1})||(0004)$ and $(\bar{2}4\bar{4})||(03\bar{3}8)$. The SAD pattern also shows evidence of streaking in both of the ⟨0001⟩ directions observed.

TEM confirmed the x-ray diffraction analysis as well as the SEM observations indicating that the film was single crystal 4H-GaN. The orientation relationship observed was $(200)||(0002)$ and $(02\bar{2})||(20\bar{2}0)$. Figure 30(left) shows the SAD pattern from the 4H-GaN region superimposed upon the β-SiC substrate pattern. Again streaking in the ⟨0001⟩

direction is observed indicating defects present in the GaN film. This is confirmed in comparing the x-ray diffraction and SEM results.

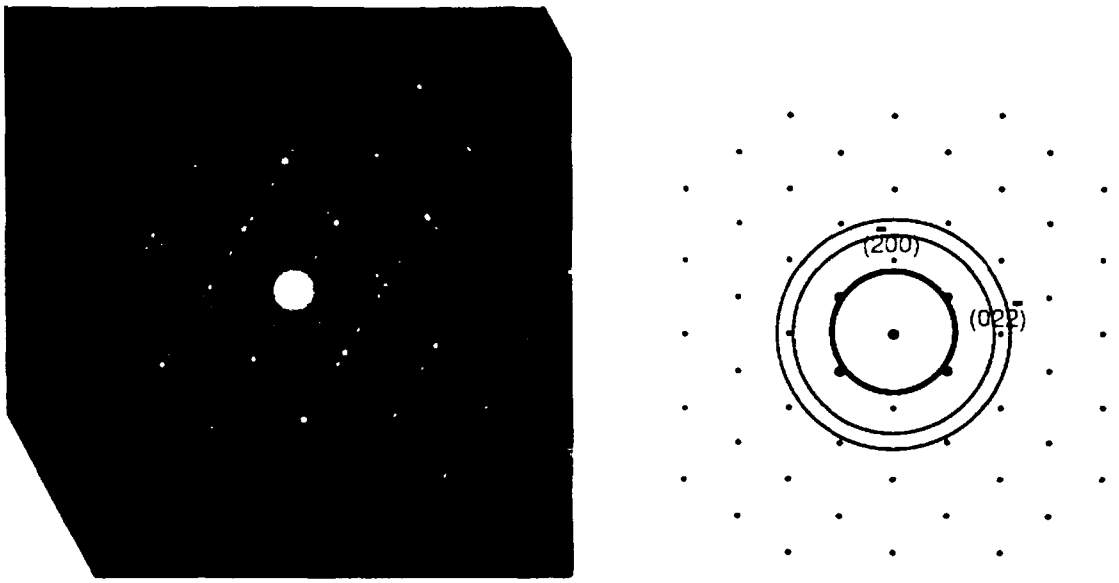

Figure 29. SAD pattern from twinned 4H-GaN on β-SiC (100) at higher growth rate (Ga @990°C) with illumination during growth. Left: Real pattern. Right: Model showing orientation (z=[011]).

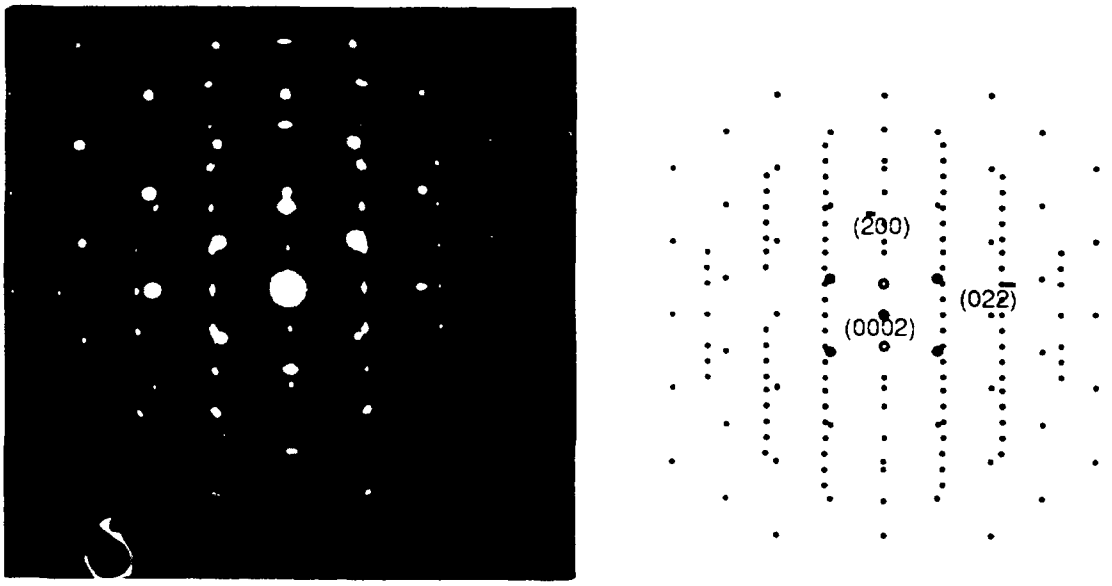

Figure 30. SAD pattern from single crystal 4H-GaN on β-SiC (100) at higher growth rate (Ga @990°C) with illumination during growth. Left: Real pattern. Right: Model showing orientation (z=[011]).

The texturing observed in the SEM is also confirmed in the bright field image shown in Figure 31. The columnar structure is evident as well as strain contrast at the GaN/β-SiC interface.

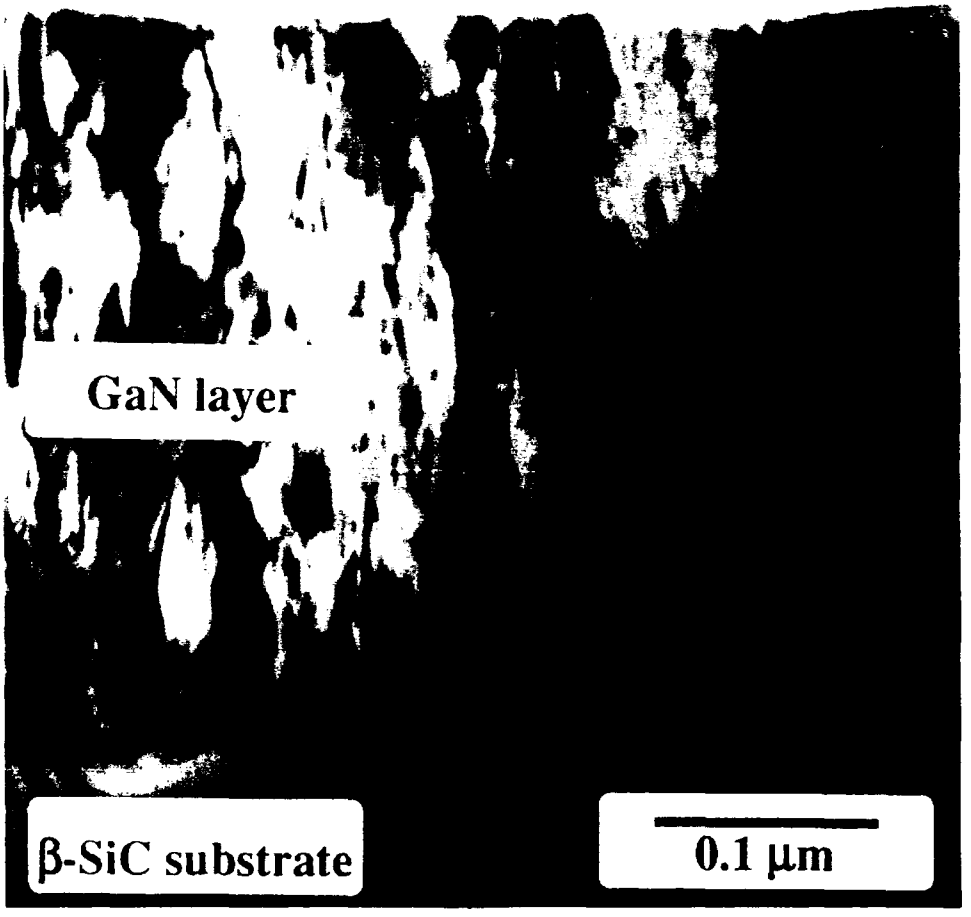

Figure 31. Bright field image of single crystal 4H-GaN on β-SiC (100) (z=[011]).

D. Discussion

1. Boron Nitride

Boron Nitride on Copper. Copper was chosen primarily because of its near perfect lattice match (Δa_0=0.022%). The thermal expansion difference is slight (≈10 ppm/°C) and actually improves the lattice match at growth temperatures. Copper does form a complex cubic nitride (Cu_3N). Its lattice parameter (3.815 Å)[60] is only ≈5% larger than c-BN. The surface energy difference is a problem, as copper has a much lower surface energy than c-BN (1430 vs. 4770 erg/cm^2).[5, 61] This problem plagues c-BN heteroepitaxial deposition on every substrate except c-BN on diamond.

An additional potential advantage in the use of copper substrates relates to the use of nitrogen as a surfactant in the growth of c-BN films. Surfactants have been used successfully in the system Si/Ge/Si to suppress island formation.[62] Dosing Cu with atomic N does form the cubic Cu_3N phase[63], noted above. It is not a strongly bonded compound and decomposes at temperatures in the range of 300–500°C.[63, 64] A cubic Cu_4N phase has also been reported. It is more difficult to form than Cu_3N. The lattice parameter of the Cu_4N phase is 3.193 Å. It decomposes above ≈550°C.[65]

X-ray diffraction indicated the presence of some phase with cubic character, perhaps a highly defective c-BN. Since the observed (110) reflection is forbidden, it would need to be a highly defective structure. There were no apparent differences in the diffraction patterns as a result of the addition of photon illumination during growth. As discussed in the Introduction, photon effects can be affected strongly by the influence of the substrate, thus this result is not necessarily surprising.

Deposition was also performed on Cu(111) to determine if the BN deposition was at all affected by interaction with the substrate. Subsequent x-ray diffraction showed the film to be strongly h-BN or t-BN.

Boron Nitride on Silicon (100). Films deposited and discussed in previous reports were analyzed via FT-IR as was shown in Figure 5. These analyses indicate some cubic-character to these predominantly amorphous films. As noted above, the peaks for amorphous BN coincide with those of h-BN and thus were not differentiated in this spectrum, but are assigned to a-BN as a result of earlier x-ray and TEM analysis.

The Introduction section showed how photon irradiation could change many kparameters in thin film growth, and so a high pressure Hg lamp was selected to illuminate samples during deposition. Figures 6-8 show the BN surfaces after deposition at 500°C coupled with illumination from the Hg lamp. The surface morphology appeared completely unchanged by the effects of the illumination. This extremely fine texture is most likely due to bombardment effects from the ECR source, as similar textures have been observed occasionally in GaN deposition.

The surface morphology of samples deposited at 400°C was changed somewhat, as documented in Figures 9–11. Small "grains" of material appeared in the surface of the otherwise identically textured surfaces. In this case, the illumination did change the morphology slightly making it more uniform. Comparison of these SEM figures with the x-ray diffraction patterns suggested that the "grains" observed in Figure 10 are h-BN, which were desorbed or prevented from forming as a consequence of the illumination (see Figure 11).

Figure 12 shows that the addition of illumination helped to initiate the formation of the c BN phase which otherwise did not occur, or did not occur in such an oriented fashion.

Details of this possible orientation effect must await TEM analysis. Figure 13 shows that the illumination dramatically decreased the h-BN (0002) peak intensity, which correlates well with the SEM observations already discussed. It was not expected that since a sharp c-BN (400) peak exists that a c-BN (200) would not exist. The scattering factors are such that the (200) peak should be as strong or stronger than the (400) peak. However, this strange outcome has been reported previously in the literature.[63–66] No reasonable explanation has been put forward to describe this unusual phenomenon.

The FT-IR analysis presented in Figure 14 shows the nature of the films deposited at 500°C. Small changes in the appearance of the peak heights occurred as a result of the UV illumination. This would seem to indicate that the presence of the c-BN peak reflects bonding of a cubic character rather than cubic structure, as is the case for the two h-BN peaks. Thus, while the crystallinity changes as indicated by x-ray diffraction, the bonding character in the larger volume of amorphous film is not dramatically affected. Deposition at 400°C involves a more dramatic change, as shown in Figure 15. The h-BN and c-BN peaks are both definitely less intense. This would indicate a dramatic reduction in the h-BN component of the film, with the peaks remaining from the amorphous component. The reduction in the c-BN peak is not understood at this time, since the x-ray diffraction peaks for the c-BN phase are virtually the same. It may be due to a reduction in the sp^3 bonding in the amorphous phase. The many peaks in the low wave number range of the unirradiated case are also not understood. Given the purity of the films, these are most likely due to defect structures which are effectively removed by the addition of the illumination. Again, much of this explanation will need to await TEM analysis.

2. Gallium Nitride

The XPS spectra in Figure 16 show no noticeable differences between films deposited with and without the lamp illumination. Higher resolution scans around the O_{1s} and C_{1s} peaks (not shown) revealed undetectable levels of contamination in both cases. Thus, further XPS analysis was not performed.

The surface morphology of the films might be expected to be quite different for films deposited with illumination from the lamp, if surface mobilities are changed as expected. Figures 17–21 clearly demonstrate this fact. The films are basically free from gross features which cannot be related to defects in the substrate surface, but the fine structure of the morphology is different in each case. Figures 17 and 18 show a film grown at a higher growth rate without illumination. This film appears to have a granular texture to it, a common feature of polycrystalline films. Figures 19 and 20 show a different granular texture, due to the effects of the photon irradiation. The features appear much rougher than the previous example, and have an, on average, different shape than before. RHEED after growth

indicated that these films were in fact polycrystalline, and had different orientations, which explains the appearance of the growth surface.

X-ray diffraction results in Figure 25 show that this change in orientation, as the unirradiated case, produced strong GaN diffraction peaks and the irradiated case did not. This would mean that the unirradiated case had a very strong (200)||(0002) texture, and the irradiated case did not, which would have strongly reduced the peak intensities. Thus the x-ray results correlate very well with the RHEED and SEM observations.

In an attempt to get single crystal material, the growth rate was lowered. This comparison is shown in Figures 21–24. Figures 21 and 22 show growth without illumination and again the surface morphology is different, with a much more uniform appearance than observed previously. However, areas are observed with varying morphology, indicating nonuniformities. RHEED after growth, was difficult to interpret due to streaking, however it appeared to be single crystal cubic GaN or something approaching single crystal in nature. Figures 22 and 23 show a dramatically flattened surface when using the photon irradiation. This surface shows a very good flatness with only a few hillock-like features. There seems to be a very fine structure that can be seen in the surface of the film. RHEED after growth would indicate a single crystal film with good flatness.

X-ray diffraction results in Figure 26 show this change in orientation, as the unirradiated case had strong cubic GaN peaks with weaker wurtzitic GaN peaks. (Note the Si (400) intensity is reduced in the unirradiated case, indicating poorer alignment of the substrate in the diffractometer, a difficult problem in a system designed for handling powders.) The irradiated case had only strong wurtzitic GaN peaks indicating a strong texture or a single crystal of GaN. Thus the x-ray results correlate very well with the RHEED and SEM observations. This is especially true for the unirradiated case where two phases appear in the x-ray diffraction data and areas of differing morphology appear in the micrographs.

XTEM analysis of these samples is shown in Figures 27–31 and indicate the observation of a new polytype of wurtzitic GaN, namely 4H-GaN. This polytype has lattice parameters of a=0.318 nm and c=1.033 nm, or the same parameters as wurtzitic (2H) GaN, but with a c-axis 2× larger than normal. This is due to a modified stacking sequence. Normal wurtzite has a stacking sequence of *abab*, while 4H material has a stacking sequence of *abcb*. Thus 4H-GaN can be interpreted as either wurtzitic GaN with regular stacking faults or atom-layer twinned cubic GaN (the ultimate micro-twin). In cases where (200)||(0002), it will be interpreted as stacking faults and where $(11\bar{1})$||(0004) it will be interpreted as perfectly regular twinning in cubic GaN.

Figure 27 shows the SAD pattern and diffraction model of the GaN deposited without illumination at the higher growth rate. Though the pattern was from a single grain, the film

was definitely polycrystalline, indicating a strong (200)||(0002) texture to the 4H-GaN deposited. Under illumination, the film developed a different texture as shown in Figure 28, showing a much reduced (200)||(0002) character. This is a rather suprising result with no clear explanation at present.

Figure 29 showed the results from the GaN deposited at a reduced growth rate without illumination, which produced cubic GaN with localized twinned regions to give the appearance of 4H-GaN. Growth with illumination produced single crystal, albeit defective, 4H-GaN, as shown in Figure 30. The orientation relationship found was (200)||(0002) and $(02\bar{2})||(20\bar{2}0)$. This relationship is somewhat unexpected as the film shown in Figure 27 had assumed a similar orientation, but with addition of the photon irradiation, it changed to a completely different one as illustrated in Figure 28. Furthermore, since the β-SiC(100) surface has four-fold symmetry and the 4H-GaN(0002) surface has six-fold symmetry the 4H-GaN must follow a two-dimensional coincidence boundary rather than a more regular alignment of lattice sites on the surface.

Finally, Figure 31 relates the structure seen in Figure 30 and the morphology observed in Figure 20. The columnar structure that is seen in Figure 31 appears similar to the surface structure observed in Figure 20, so that the observed surface morphology extends well into the GaN layer. The GaN/β-SiC interface appears sharp with strain contrast appearing due to the misfit between the materials.

E. Conclusions

1. Boron Nitride

Boron Nitride on Copper. Films of a highly defective and nanocrystalline c-BN nature were deposited on Cu (110). Films deposited on Cu (111) were clearly different and of a h-BN character, indicating that the substrate had a strong influence on the crystal structure of the BN films.

Boron Nitride on Silicon (100). Films deposited without photon irradiation and reported previously were analyzed in this reporting period. These films contained material with cubic character, as revealed by FT-IR studies. Ultra-violet irradiation was shown to have a definite effect on the deposition of the BN films. At 500°C, it enhanced the crystallization of the c-BN phase and did not encourage the formation of h-BN. At 400°C, photon irradiation clearly inhibited the formation of the h-BN phase, which had previously formed more readily at that temperature and did not inhibit the crystallization of the c-BN phase. Illumination of the growth surface also appeared to reduce certain types of cubic-like character in the film, but also removed other types of bonding defects present in the films.

2. Gallium Nitride

Films containing a new polytype of GaN, namely 4H-GaN, were grown. Photon irradiation was clearly shown to change the growth rate, morphology, and crystalline phase orientation to the β-SiC substrate. Changes in each of these properties were documented in detail using RHEED, x-ray diffraction, field emission SEM (both secondary and back-scattered), and electron diffraction.

F. Future Research Plans/Goals

1. Boron Nitride

Boron Nitride on Copper. Evaluation of these films will continue to determine if the lattice match of Cu substrates can be exploited to produce c-BN films. Thin-film reflection FT-IR will be used to determine the amount of amorphous component present. Should these films become sufficiently large in extent, they will be floated from the substrate and analyzed via TEM.

Boron has a low solubility in copper (≈0.5 at.%). If boron were diffused into copper at a high temperature and then cooled the boron would migrate to the surface. Since the boron species would migrate to sites on the copper surface, they would already possess the same symmetry as would be present in c-BN. Subsequent exposure to atomic nitrogen from the plasma source and reaction with the diffusing boron would allow the c-BN phase to form more readily and more uniformly across the surface of the copper substrate. This would not only improve the phase stability but help to resist the driving force for island formation which is quite strong for c-BN on copper. Some boron diffusion and implantation have already been conducted, the deposition of BN on these samples will be performed during the next reporting period.

Boron Nitride on Silicon (100). The first priority will be TEM analysis of the deposited films to determine (1) the extent of the c-BN deposition that has occurred, and (2) if any other photon irradiation effects can be observed. Experiments will be conducted using selective bandpass filters on the light source to determine if a strong or weak wavelength dependence is present and where in the spectrum of the light source it occurs. Finally, experiments will be initiated to determine if these photon-induced reactions can be made to occur after deposition and to see if the effects are in the bulk or strictly growth surface related.

2. Gallium Nitride

An extension of the research described above to still lower growth rates will be undertaken in an attempt to determine what phase effects will exist in a pure cubic-phase GaN. Should a transition from cubic to wurtzitic occur as a result of UV illumination as the

present evidence indicates, this would be solid, additional proof of the photophase effect in wide bandgap semiconductors. Analysis of the defects in those films will be conducted to determine if the defect density is reduced by photon irradiation. The electrical properties will also be evaluated on irradiated and unirradiated samples.

G. References

1. R. H. Wentorf Jr., J. Chem. Phys. **36**, 1990 (1962).
2. R. M. Chrenko, Solid State Commun. **14**, 511 (1974).
3. C. Deshpandey and R. F. Bunshah, Thin Solid Films **163**, 131 (1988).
4. N. Miyata, K. Moriki, and O. Mishima, Phys. Rev. B **40**(17), 12028 (1989).
5. R. C. DeVries, Cubic Boron Nitride: Handbook of Properties, Technical Information Series, General Electric Company, Corporate Research and Development, 72CRD178, 1972.
6. K. H. Seidel, K. Reichelt, W. Schaal, and H. Dimigen, Thin Solid Films **151**(2), 243 (1987).
7. M. Mieno and T. Yoshida, Jpn. J. Appl. Phys. **29**(7), 1175 (1990).
8. M. Satou and F. Fujimoto, Jpn. J. Appl. Phys. **22**(3), L171 (1983).
9. Y. Andoh, *et al.*, Nucl. Instrum. Meth. Phys. Res. **B19/20**, 787 (1987).
10. J. Kouvetakis, V. V. Patel, C. W. Miller, and D. B. Beach, J. Vac. Sci. Technol. A **8**(6), 3929 (1990).
11. H. Saitoh, T. Hirose, H. Matsui, Y. Hirotsu, and Y. Ichinose, Surf. Coat. Technol. **39–40**(1–3), 265 (1989).
12. M. Okamoto, H. Yokoyama, and Y. Osaka, Jpn. J. Appl. Phys. **29**(5), 930 (1990).
13. A. Chayahara, H. Yokoyama, T. Imura, and Y. Osaka, Appl. Surf. Sci. **33/34**, 561 (1988).
14. O. Matsumoto, M. Sasaki, H. Suzuki, H. Seshimo, and H. Uyama, in *Tenth International Conference on Chemical Vapor Deposition*. G. W. Cullen, Eds. (The Electrochemical Society, Honolulu, Hawaii, 1987), pp. 552.
15. T. Ikeda, Y. Kawate, and Y. Hirai, Kobelco Technol. Rev. **6**, 1 (1989).
16. M. Murakawa and S. Watanabe, Surf. Coatings Technol. **43/44**(1-3), 128 (1990).
17. T. Nagatomo, Y. Hatooka, and O. Omoto, Trans. IECE Jpn. E **69**(4), 482 (1986).
18. T. Ikeda, Y. Kawate, and Y. Hirai, J. Vac. Sci. Technol. A **8**(4), 3168 (1990).
19. A. R. West, *Solid State Chemistry and its Applications* (John Wiley & Sons, Chichester, 1984).
20. F. N. H. Robinson, Phys. Lett. A **26**(9), 435 (1968).
21. Z. Sitar, *et al.*, Mat. Sci. Lett. **preprint**, preprint (1991).
22. P. D. Fleischauer, in *Concepts of Inorganic Photochemistry* A. W. Adamson, and P. D. Fleischauer, Eds. (Wiley-Interscience, New York, 1975), pp. 439.
23. R. Solanki, C. A. Moore, and G. J. Collins, Sol. State Technol. **28**(6), 220 (1985).
24. B. A. Joyce, J. Phys. Chem. Solids **49**(3), 237 (1988).
25. T. Y. Sheng, Z. Q. Yu, and G. J. Collins, Appl. Phys. Lett. **52**(7), 576 (1988).
26. T. Yamazaki, S. Watanabe, and T. Ito, J. Electrochem. Soc. **137**(1), 313 (1990).
27. A. I. Kingon, O. Auciello, M. S. Ameen, S. H. Rou, and A. R. Krauss, Appl. Phys. Lett. **55**(3), 301 (1989).
28. A. Lietoila, R. B. Gold, J. F. Gibbons, and L. A. Christe, in *CW Beam Processing of Silicon and Other Semiconductors* J. F. Gibbons, Eds. (Academic Press, New York, 1984), pp. 71.
29. J. A. Van Vechten, R. Tsu, F. W. Saris, and D. Hoonhout, Phys. Lett. **74A**(6), 417 (1979).
30. J. A. Van Vechten, R. Tsu, and F. W. Saris, Phys. Lett. **74A**(6), 422 (1979).
31. Z. Yu and G. J. Collins, Phys. Scripta **41**(1), 25 (1990).

32. M. Kitagawa, Y. Tomomura, K. Nakanishi, A. Suzuki, and S. Nakajima, J. Cryst. Growth **101**, 52 (1990).
33. N. Matsumura, T. Fukada, and J. Saraie, J. Cryst. Growth **101**(1–4), 61 (1990).
34. K. L. Chopra, L. K. Malhotra, K. S. Harshavardhan, and S. Rajagopalan, Bull. Mater. Sci. **6**(6), 1013 (1984).
35. R. N. Bicknell-Tassius, A. Waag, Y. S. Wu, T. A. Kuhn, and W. Ossau, J. Cryst. Growth **101**(1–4), 33 (1990).
36. W. A. Young, M. Y. Mirza, and W. W. Duley, Opt. Commun. **34**(3), 353 (1980).
37. W. I. Milne, F. J. Clough, S. C. Deane, S. D. Baker, and P. A. Robertson, Appl. Surf. Sci. **43**, 277 (1989).
38. A. Gedanken, M. B. Robin, and N. K. Kuebler, J. Phys. Chem. **86**, 4096 (1982).
39. H. Okabe, *Photochemistry of Small Molecules* (Wiley-Interscience, New York, 1978).
40. N. C. Giles, *et al.*, J. Cryst. Growth **86**(1-4), 348 (1988).
41. N. C. Giles, K. A. Bowers, R. L. Harper Jr., S. Hwang, and J. F. Schetzina, J. Cryst. Growth **101**(1–4), 67 (1990).
42. R. L. Harper, Jr., *et al.*, J. Vac. Sci. Technol. B **7**(2), 244 (1989).
43. S. Fujita, A. Tanabe, T. Kinoshita, and S. Fujita, J. Cryst. Growth **101**(1–4), 48 (1990).
44. P. A. Kohl and F. W. Ostermayer Jr., in *Annual Review of Materials Science* R. A. Huggins, J. A. Giordmaine, and J. B. Wachtman Jr., Eds. (Annual Reviews, Inc., Palo Alto, CA, USA, 1989), pp. 379.
45. H. Kokado, I. Simizu, and E. Inoue, J. Non-Cryst. Sol. **20**(1), 131 (1976).
46. A. Das and R. A. Jishi, Phil. Mag. Lett. **62**(2), 107 (1990).
47. G. Kluge, Phys. Stat. Sol. A **101**(1), 105 (1987).
48. T. Wolkenstein, Adv. Catal. Rel. Subj. **23**, 157 (1973).
49. S. R. Morrison, J. Catal. **20**, 110 (1971).
50. W. Ho, in *Photochemistry in Thin Films*. T. F. George, Eds. (SPIE, Los Angeles, CA, 1989), pp. 157.
51. J. P. Cowin, E. P. Marsh, W. Meier, T. L. Gilton, and M. R. Schneider, in *Photochemistry in Thin Films*. T. F. George, Eds. (SPIE, Los Angeles, CA, 1989), pp. 147.
52. F. G. Celii, H. H. Nelson, and P. E. Pehrsson, J. Mater. Res. **5**(11), 2337 (1990).
53. R. M. Feenstra and T. C. McGill, Physica B **117–118**, (1983).
54. M. V. Alfimov, I. L. Aptekar', A. E. Galashin, and E. A. Galashin, Sov. Phys. Dokl. **29**(5), 404 (1984).
55. A. Matsuda and M. Kikuchi, Sol. St. Commun. **12**, 359 (1973).
56. Z. Sitar, M. J. Paisley, D. K. Smith, and R. F. Davis, Rev. Sci. Instrum. **61**(9), 2407 (1990).
57. J. R. Vig, J. Vac. Sci. Technol. A **3**(3), 1027 (1985).
58. H. Lamb, private communication, 1990.
59. I. Villegas, C. B. Ehlers, and J. L. Stickney, J. Electrochem. Soc. **137**(10), 3143 (1990).
60. V. R. Juza and H. Hahn, JCPDS Card #2-1156, Powder Diffraction File, JCPDS, 2-1156, 1938.
61. C. R. Barrett, W. D. Nix, and A. S. Tetelman, *The Principles of Engineering Materials* (Prentice-Hall, Inc., Englewood Cliffs, New Jersey, 1973).
62. M. Copel, M. C. Reuter, E. Kaxiras, and R. M. Trump, Phys. Rev. Lett. **63**(6), 632 (1989).
63. D. Heskett, A. Baddorf, and E. W. Plummer, Surf. Sci. **195**(1-2), 94 (1988).
64. M. Asano, K. Umeda, and A. Tasaki, Japanese Journal of Applied Physics **29**(10), 1985 (1990).
65. J. Blucher, K. Bang, and B. C. Giessen, Mater. Sci. Eng. A **117**, L1 (1989).
66. K. Inagawa, K Watanabe, K. Saitoh, Y. Yuchi, and A. Itoh, New Diamond , 60 (1988).
67. K. Inagawa, K. Watanabe, H. Ohsone, K. Saitoh, and A. Itoh, J. Vac. Sci. Technol. A **5**(4), 2696 (1987).
68. G. L. Doll, in *New Diamond Science and Technology*. R. Messier, J. T. Glass, J. E. Butler, and R. Roy, Eds. (Materials Research Society, Washington, DC, 1990), pp. xxi+1128.

CUBIC BORON NITRIDE THIN FILM SYNTHESIS BY MICROWAVE ECR PLASMA CHEMICAL VAPOR DEPOSITION

by

M. J. Paisley, Z. Sitar, L. P. Bourget* and R. F. Davis
Department of Materials Science and Engineering
Box 7919, North Carolina State University
Raleigh, North Carolina 27695-7907

*Applied Science and Technology (ASTeX), Incorporated
35 Cabot Road
Woburn, MA 01801

Submitted to

Kobe Engineering Reports

September 20, 1991

Abstract

Thin films of cubic boron nitride (c-BN) have many applications in areas such as diamond substrates and optoelectronic devices in the vacuum ultraviolet. The objective of this study was the deposition of c-BN on Si (100) and (111) using microwave ECR plasma chemical vapor deposition with borazine as the source material. Films were deposited and analyzed employing the techniques of ellipsometry, x-ray photoelectron spectroscopy (XPS), x-ray diffraction (XRD), transmission electron microscopy (TEM), and Fourier transform infrared spectroscopy (FT-IR). Results indicated the deposited films were comprised of microcrystals of c-BN and oriented hexagonal BN as well as amorphous BN.

I. Introduction

The cubic polymorph of BN has received much interest recently as a possible substrate for the deposition of diamond, due to the similar lattice parameters (Δa_0=1.34%) and its wider bandgap which is in the range of 5.8–6.5 eV.[1–3] The very wide bandgap of c-BN also gives c-BN potential applications in its own right, as optical devices for the vacuum UV (λ~200 nm) as well as more traditional applications such as a hard coating for machining ferrous metals. For a complete listing of materials-related properties of c-BN see *Landolt-Börnstein:Numerical Data and Functional Relationships in Science and Technology, Series III, Vols. 17 and 23*, or Ref. 4 (which also includes a side-by-side comparison of properties of c-BN with diamond).

II. Experimental Procedure

The depositions were carried out at the ASTeX, Inc. facilities in Woburn, MA a microwave electron cyclotron resonance (ECR) plasma chemical vapor deposition (CVD) systems adapted for handling BN precursor species. This involved installing a special mass flow controller calibrated for low vapor pressure gases and a bottle of borazine ($B_3N_3H_6$) liquid into the gas handling system. Borazine (analogous to the carbon compound benzene) has been used previously for deposition of BN films in CVD reactors,[5–7] but not with a microwave ECR plasma source.

The microwave ECR plasma CVD gas system consisted of a gas manifold and the associated mass flow controllers which fed gases directly into the plasma or downstream near the substrate. Depositions were performed with argon and nitrogen were injected directly into the plasma, while the borazine was injected downstream. The 35 cm diameter chamber was evacuated by an 880 l/sec turbomolecular pump (base pressure: mid 10^{-7} Torr) backed by a 50 cfm mechanical pump which was vented to an exhaust system. The substrate was rf induction heated and its temperature calibrated with a thermocouple placed on the substrate's surface. The substrate support was isolated, making it possible to add rf biasing to the substrate to independently control ion energy and ion flux to the substrate. A schematic diagram of the ASTeX system is shown in Figure 1.

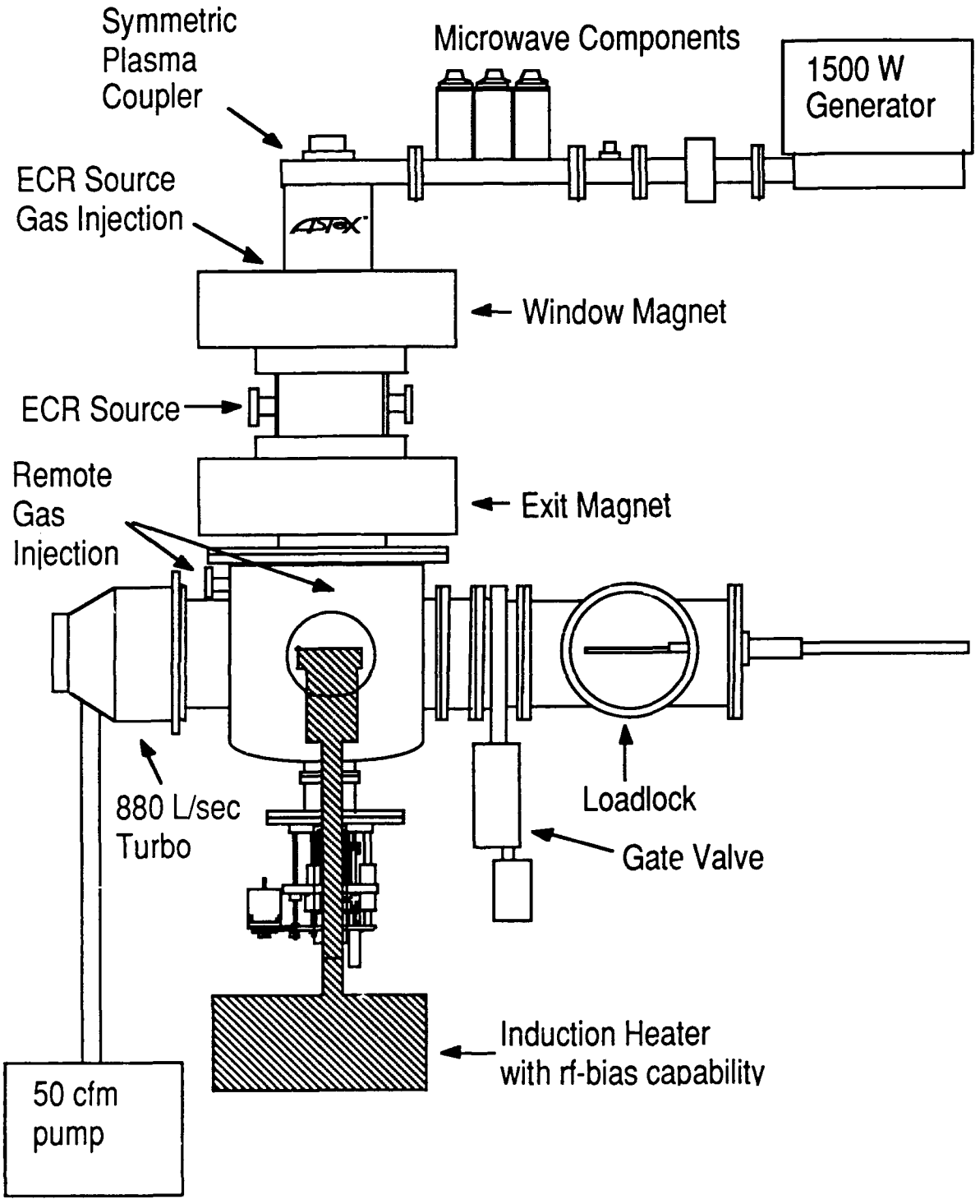

FIG. 1. Schematic diagram of microwave ECR plasma CVD system used at ASTeX, Inc. to deposit BN films.

Substrates of Si (111) or Si (100) were placed into a load lock and evacuated before loading into the main deposition chamber. The samples were subsequently heated under vacuum until the deposition temperature was reached. Finally, nitrogen and argon gas flow was begun, the plasma was ignited, and borazine flow was started which initiated deposition. In situations where substrate bias was used, the plasma was initiated and the bias conditions were established prior to deposition. The range of conditions used for deposition is shown in Table 1.

Table 1. Deposition Conditions used in ECR CVD of BN.

Borazine flow	0.6 – 4.0 sccm
Nitrogen flow	0.0 – 20.0 sccm
Argon flow	0.0 – 50.0 sccm
Chamber pressure	0.9 – 5.0 mTorr
Microwave power	500 – 1000 W
Substrate temperature	590 – 620°C
Substrate rf-induced voltage	0 to –65 VDC
Growth time (BN)	3 – 30 min.
Deposited film thickness	50 – 2000 nm

While applied rf power is often reported in the literature, this value is not nearly as descriptive as the induced voltage that is reported in Table A.1. When rf power is applied to the substrate, a DC bias is induced on the substrate surface. This bias results in ions being accelerated to the substrate surface. The rf bias was measured simply by attaching a voltmeter between ground and the substrate holder with the addition of a low-pass filter to protect the voltmeter from rf voltages.

After deposition, the samples were cooled and measured by a rotating polarizer type ellipsometer to obtain index of refraction data. Finally, the samples were sent to NCSU for further analysis.

III. Results and Discussion

The resulting refractive index varied among the films over the range of 1.65–2.28, where c-BN is n=2.12, and h-BN is n=2.02 {|| c-axis} and n=2.22 {⊥ c-axis}).[8] This would seem to indicate a mixture of phases was present, with porosity or hydrogen incorporation accounting

for the lower values measured. An x-ray spectrum of a film with n=2.01 is shown below in Figure 2.

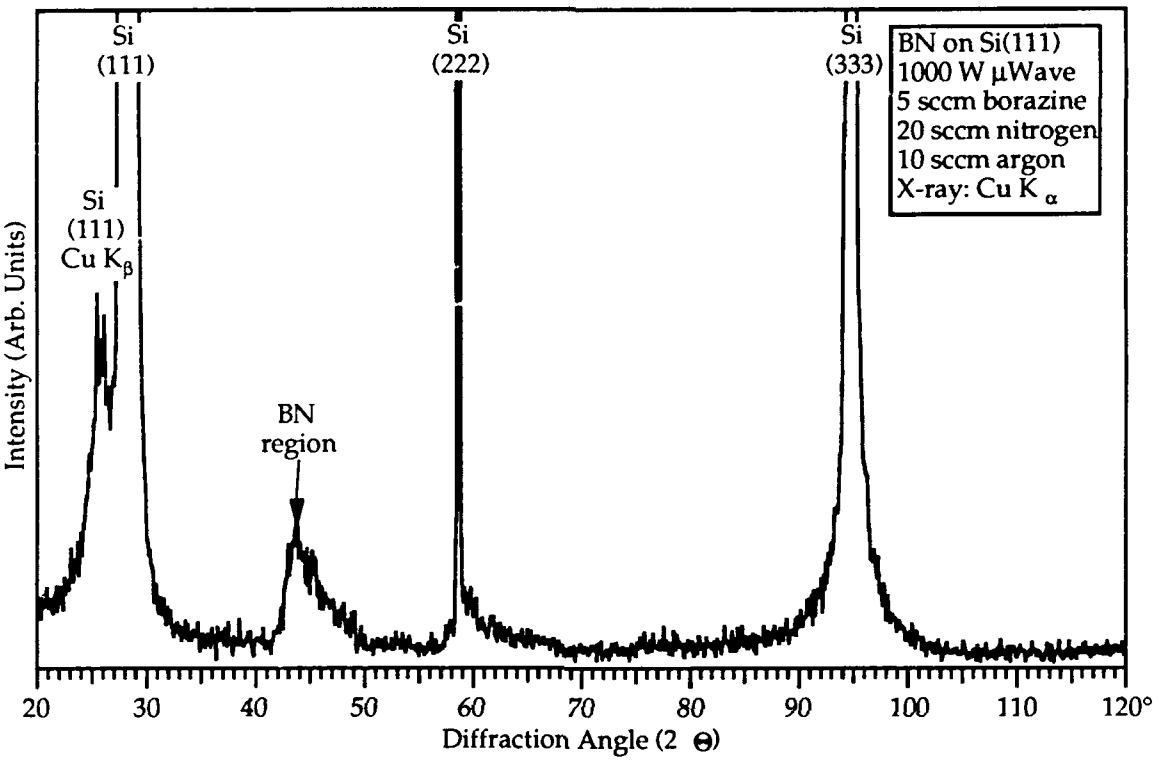

FIG. 2. Typical x-ray spectrum from BN deposited on Si (111) substrate. Note BN region which cannot be resolved into individual peaks present.

The spectrum shows only a broad band of reflections in the region of 42–50° (2θ), which covers a number of peaks from all phases of BN. The Si (111) Cu Kβ peak is exactly where predicted, but is unlikely since the detector has a graphite monochromator to greatly reduce that peak. The h-BN (002) peak is either obscured in the lower edge of Si (111) peak, or has shifted down slightly (*i.e.*, the lattice expanded) and is where the Cu Kβ peak should be. If this were the case, its relative intensity would seem to indicate a significant portion of the broad BN region is from phases other than h-BN. The fact that the region is continuous also indicates at least some amorphous component. Analysis by XPS shown in Figure 3 shows that the film is free from contamination other than carbon and oxygen. Much, if not all, of this contamination is due to atmospheric exposure.

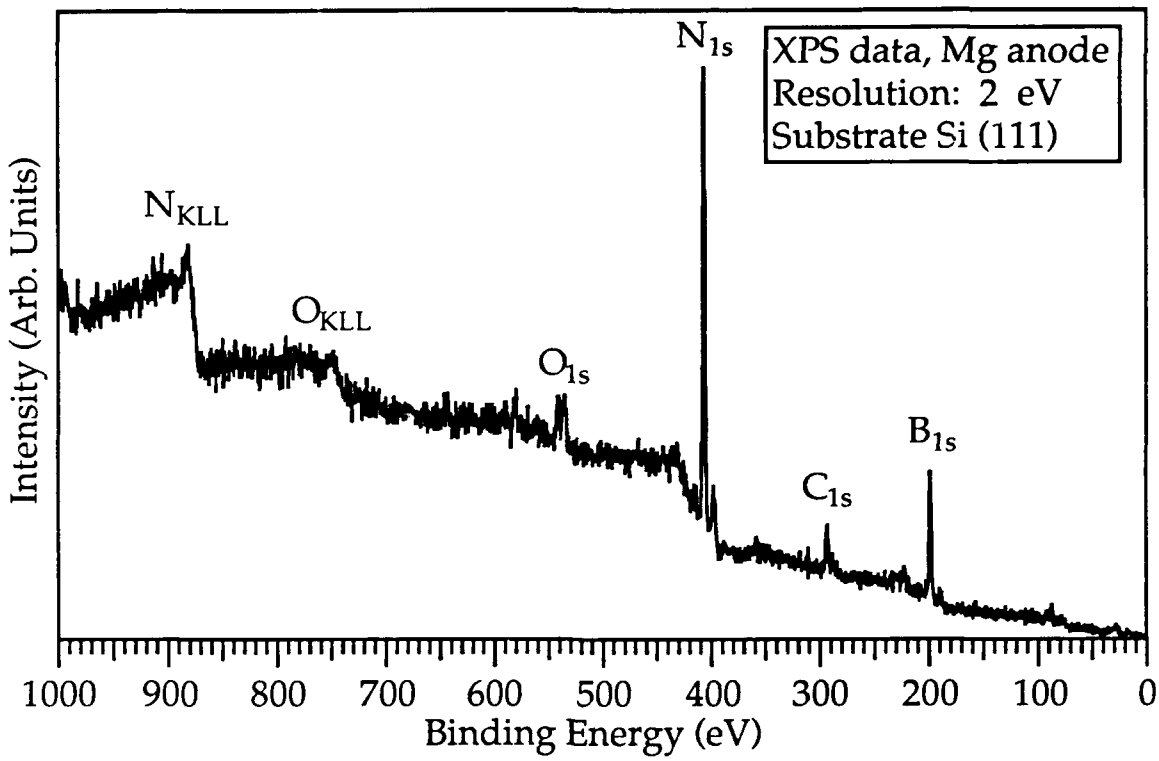

FIG. 3. XPS spectrum from BN deposited on Si (111) substrate. Note carbon and oxygen contamination peaks are most likely due to atmospheric exposure

FT-IR spectra of these films shows both hexagonal (peaks at 1370 and 870 cm^{-1}) and cubic (peak at 1100 cm^{-1}) BN phases present along with very minor amounts of hydrogen incorporation under some processing conditions, as is shown in Figures 4 and 5. The FT-IR spectrum shown in Figure 4 shows a fairly clean spectrum with only very slight hydrogen/argon incorporation, as indicated by the almost undetectable peaks in the 3200–3500 cm^{-1} range. Calculation of proportions of cubic and hexagonal/amorphous phases using reported relative absorption factors[9] yields V_h/V_c=9.8, thus the film contains ≈10% c-BN. The peak at 615 cm^{-1} has not been identified though seems at present to be substrate related while the peak at 3240 cm^{-1} is most likely a second N–H stretching mode when compared to group frequency charts.[10, 11] These peaks are apparently related to incorporation effects as will be discussed next.

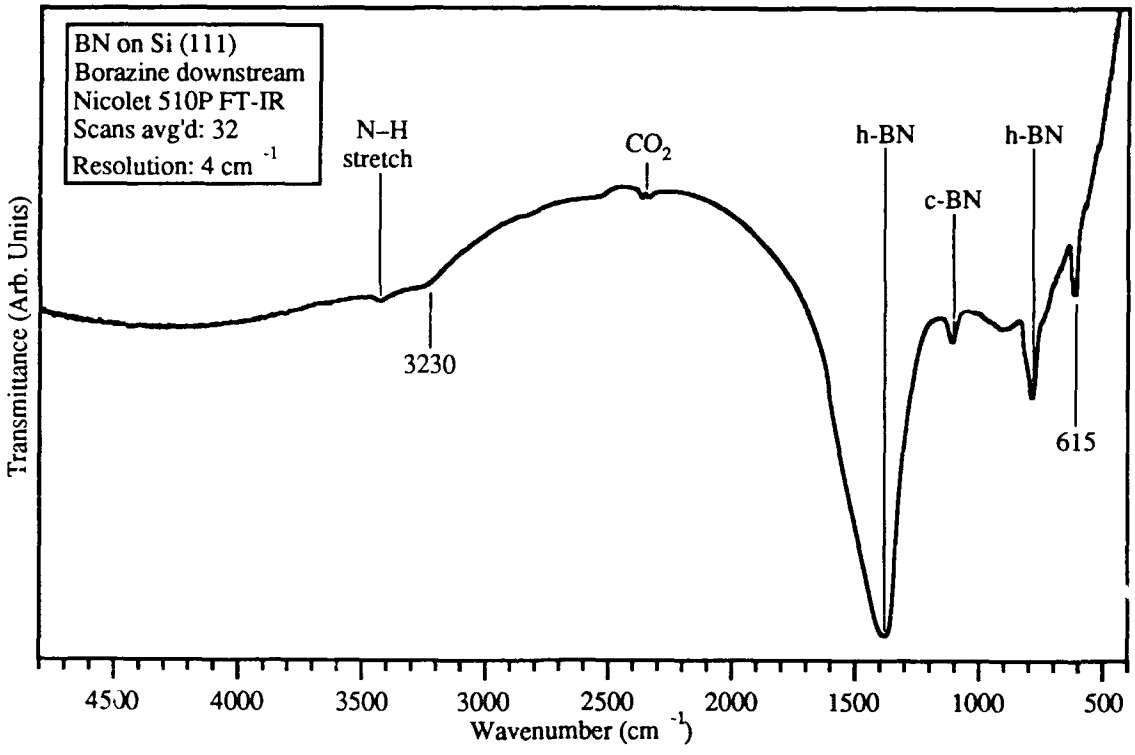

FIG. 4. FT-IR spectra of BN on Si(111) showing h-BN and c-BN peaks and very little hydrogen/argon incorporation (0 V bias, 10 sccm Ar, 1000 W).

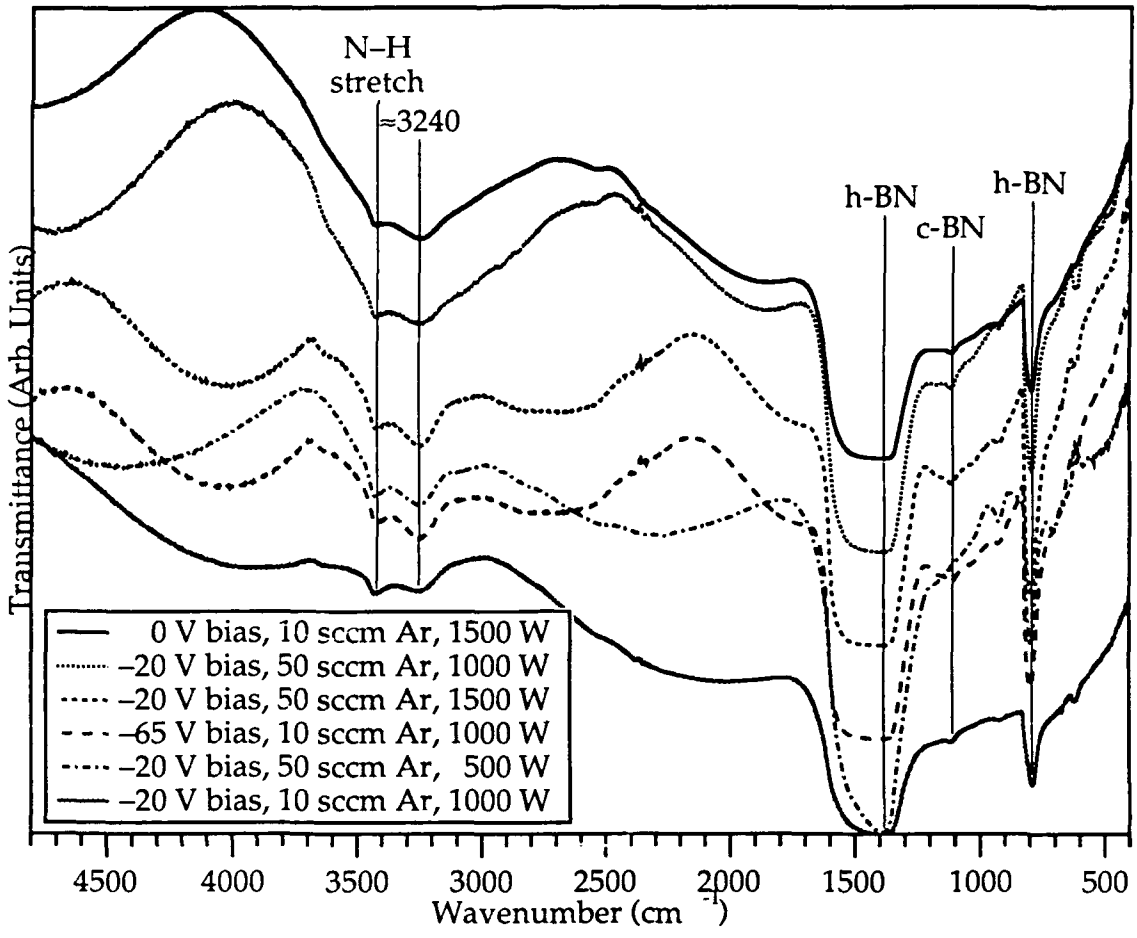

FIG. 5. FT-IR spectra of BN on Si (111) under various processing conditions showing heavily distorted h-BN and c-BN (almost invisible) peaks, as well as hydrogen/argon incorporation.

Figure 5 which shows spectra from several different deposition conditions. A comparison of the spectra of Figures 4 and 5 reveal variations in intensity of the N–H stretch and 3240 cm^{-1} peaks as well as both peaks for h-BN. The spectra in Figure 5 show strong peaks of various intensities in the 3200–3500 cm^{-1} range and an apparent broadening of the B–N stretching mode in the range from 1380–1550 cm^{-1}. The later relates either to a disordering effect from argon incorporation or perhaps the addition of a N–H bending mode which also occurs in that region.[11] It seems that for Ar flow rates ≥10 sccm, or microwave power levels

: 1000 W, or bias conditions ≤ –20 VDC, cause hydrogen and perhaps argon to begin to be incorporated into the growing film.

As a companion technique to the FT-IR analysis, samples were analyzed with Raman spectroscopy. Figure 6 shows a spectrum from the film indicating the highest fraction of c-BN from FT-IR analysis. This spectrum reveals the presence of a mix of phases. Hexagonal BN has one Raman active peak at 1368 cm^{-1} while c-BN has two peaks, namely the TO (transverse optical) at 1055 cm^{-1} and the LO (longitudinal optical) at 1308 cm^{-1}.[12] These values for BN were also confirmed by use of standards in the system used here. The h-BN phonon and the LO phonon of c-BN are clearly present, though apparently shifted slightly by stress. In addition there is another weak peak at 1244 cm^{-1} which has been described as a plasmon-phonon coupling mode by P. V. Huong.[13] More importantly, this spectrum also does not show the TO phonon mode at 1055 cm^{-1}, which may be due either to stress or other effects not yet determined.

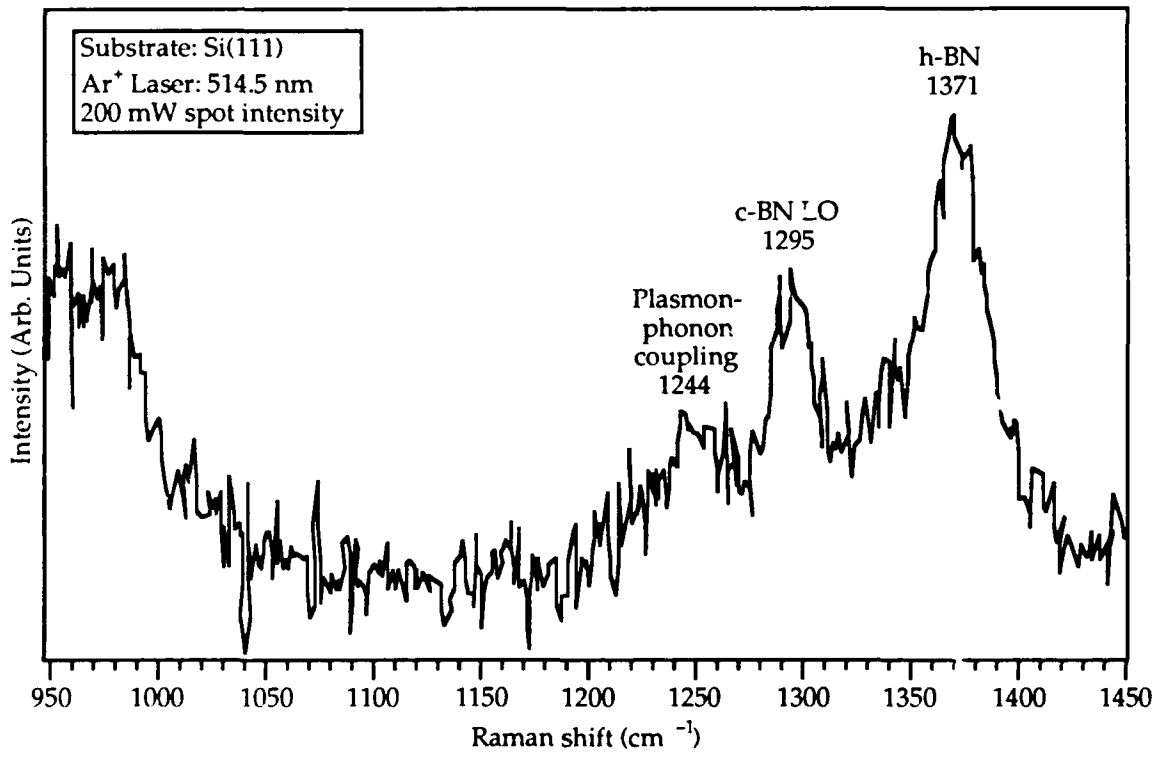

FIG. 6. Raman spectrum of BN on Si (111) for sample showing highest c-BN fraction.

Samples from the conditions yielding the most c-BN were prepared for cross-section TEM using standard techniques.[14] A bright-field micrograph of the cross-section region of the film is shown in Figure 7. The measured film thickness was 0.7 μm which corresponds to a growth rate of 1.4 μm/h. The inset photograph shows the SAD pattern observed for this film and indicates that the deposited layers are oriented h-BN with texture appearing to be h-BN (002) || Si (111). Samples grown at high substrate bias condition (≥50 VDC) delaminated from the Si substrate, presumably due to induced stress from ion bombardment. Pieces of the delaminated films were placed on nickel grids and examined in the TEM. SAD patterns from a typical region of the BN layer showed very diffuse rings from a-BN. This was especially true of the highest bias conditions (-65 VDC).

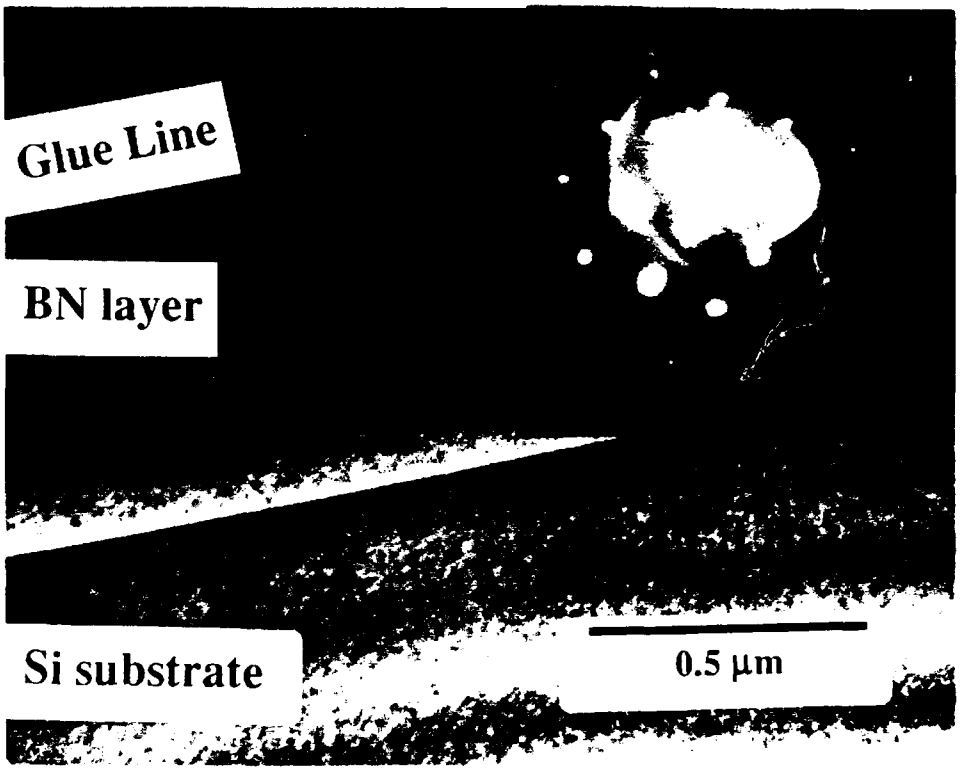

FIG. 7. XTEM photograph of BN on Si (111) with z=[110]. Inset shows SAD pattern of Si with oriented polycrystalline h-BN.

While no c-BN was observed in the SAD patterns, this is not surprising given the low concentration of c-BN and the polycrystalline/amorphous nature of much of the film. In

addition, many of the c-BN diffraction lines are very close to those of other phases of BN. This makes unambiguous phase identification virtually impossible unless the diffraction patterns are extremely sharp.

IV. Conclusions

Boron nitride thin films deposited on Si via microwave ECR CVD from borazine and nitrogen showed a mixed composition of amorphous, hexagonal and cubic phases of BN. Evidence of hydrogen/argon incorporation was observed at high deposition power and bias levels, as well as high argon flow rates. In addition, substrate biasing seemed to degrade the film quality, in contrast to the results reported by other workers. The authors think that zero or low bias ($0 \leq -20$ VDC) levels would probably result in the best films using these source gases.

V. Acknowledgements

The authors would like to acknowledge the support for this work from the Kobe Steel Research Laboratories, USA as well as Applied Science and Technology (ASTeX), Inc. Additional thanks go to L. Smith and R. C. Glass for the XPS and x-ray analyses.

VI. References

1. R. M. Chrenko, *Solid State Commun.* **14**, 511 (1974).
2. C. Deshpandey and R. F. Bunshah, *Thin Solid Films* **163**, 131 (1988).
3. N. Miyata, K. Moriki, and O. Mishima, *Phys. Rev. B* **40**(17), 12028 (1989).
4. R. C. DeVries, *Cubic Boron Nitride: Handbook of Properties*, Technical Information Series, General Electric Company, Corporate Research and Development, 72CRD178, 1972.
5. R. R. Rye, *J. Vac. Sci. Technol. A* **9**(3), 1099 (1991).
6. J. Kouvetakis, V. V. Patel, C. W. Miller, and D. B. Beach, *J. Vac. Sci. Technol. A* **8**(6), 3929 (1990).
7. S. Shanfield and R. Wolfson, *J. Vac. Sci. Technol. A* **1**(2), 323 (1983).
8. K. H. Hellwege, ed., *Landolt-Börnstein:Numerical Data and Functional Relationships in Science and Technology, Series III, Vol. 17* (Springer-Verlag, Berlin, Heidelberg, New York, Tokyo, 1987).

9. H. Yokoyama, M. Okamoto, and Y. Osaka, *Jpn. J. Appl. Phys.* **30**(2), 344 (1991).

10. K. Nakamoto, *Infrared and Raman Spectra of Inorganic and Coordination Compounds* (John Wiley and Sons, New York, 1986).

11. R. C. Weast, ed., *CRC Handbook of Physics and Chemistry* (CRC Press, Inc., Boca Raton, FL, 1988).

12. D. R. Clarke and F. Adar, in *Advances in Materials Characterization*, edited by D. R. Rossington, R. A. Condrate, and R. L. Snyder (Alfred University, 1982), 199.

13. P. V. Huong, *Diamond Relat. Mater.* **1**(1), 33 (1991).

14. J. C. Bravman and R. Sinclair, *J. Electron Microsc. Techniq.* **1**, 53 (1984).